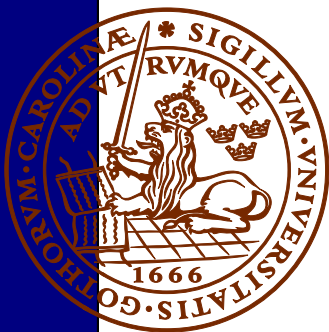
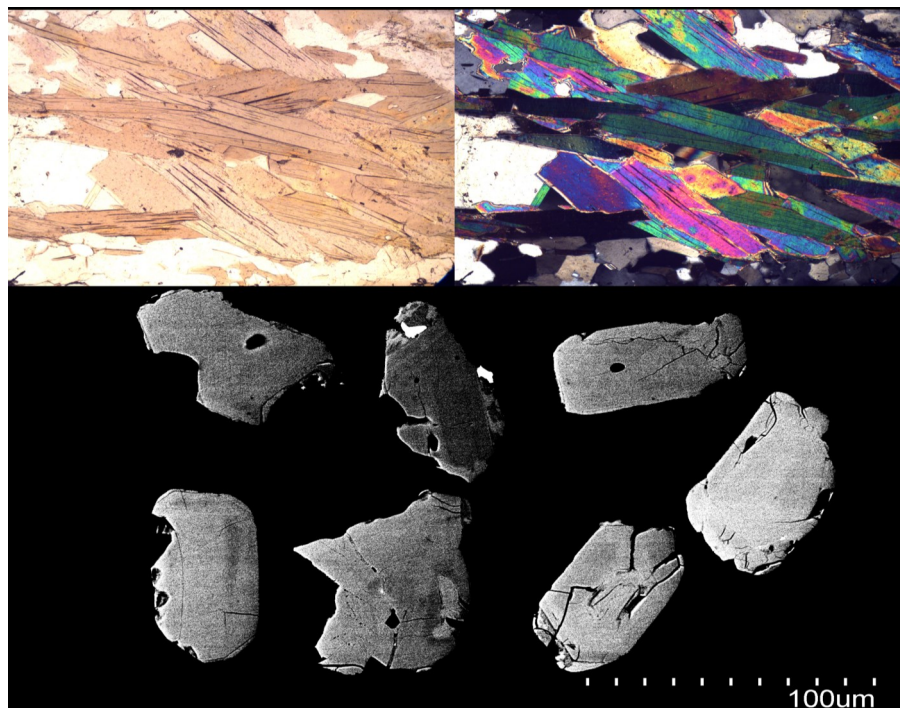


U-Pb geochronology and geochemistry of host rocks to the Bastnäs-type REE mineralization in the Riddarhyttan area, west central Bergslagen, Sweden

Wictor Linders

Dissertations in Geology at Lund University,
Master's thesis, no 466
(45 hp/ECTS credits)



Department of Geology
Lund University
2016

U-Pb geochronology and geochemistry of host rocks to the Bastnäs-type REE mineralization in the Rid-darhyttan area, west central Bergslagen, Sweden

Master's thesis
Wictor Linders

Department of Geology
Lund University
2016

Contents

1 Introduction	8
2 Background	9
2.1 Rare earth elements	9
2.2 Regional geology	10
2.2.1 The Fennoscandian shield	10
2.2.2 The Bergslagen region	11
2.2.2.1 Geology	11
2.2.2.2 Tectonic evolution models	12
2.3 Geology of the REE-line in western central Bergslagen	13
3 Principal and applied analytical methods	15
3.1 Sampling and separation of minerals for geochronology	15
3.1.1 Sample collection	15
3.1.2 Zircon and monazite separation	16
3.1.3 Scanning electron microscope (SEM) and backscattered electron (BSE) imaging	16
3.2 Overview of minerals used for geochronology	18
3.2.1 Zircon	18
3.2.2 Monazite	18
3.3 Geochronology – basics and applications	18
3.3.1 The U-Th-Pb system	18
3.3.1.1 General overview	18
3.3.1.2 Age equations	20
3.3.1.3 Visualization of U-Th-Pb data	21
3.4 Laser ablation inductively coupled plasma mass spectrometry (LA-ICP-MS)	23
3.5 Immobile element monitor for a single precursor system and isocon analysis	24
4 Samples and petrography	25
4.1 Sample collection	25
4.2 Sample descriptions	25
5 Results	31
5.1 Whole rock (WR) analysis	31
5.1.1 Major elements	31
5.1.2 Trace elements	31
5.1.3 Immobile element plots	31
5.1.4 Relative concentration change during alteration	31
5.2 Geochronology	36
6 Discussion	41
6.1 Geochemical signatures of the metavolcanic rocks	41
6.2 Isocon data	42
6.2.1 Implications of the isocon diagrams	42
6.2.2 Pitfalls with the isocon method	42
6.3 Nature of the alteration process(es)	52
6.4 Geochronology	52
6.5 Key issues for future work	56
7 Conclusions	56
8 Acknowledgements	56
9 References	56
10 Appendices	62

Cover Picture: Pictures in the upper left and right show biotite grains with radiation damage from minerals such as zircon and monazite. Lower image shows BSE-images of zircon crystals.

U-Pb geochronology and geochemistry of host rocks to the Bastnäs-type REE mineralization in the Riddarhyttan area, west central Bergslagen, Sweden

WICTOR LINDERS

Linders W., 2016: U-Pb geochronology and geochemistry of host rocks to the Bastnäs-type REE mineralization in the Riddarhyttan area, west central Bergslagen, Sweden. *Dissertations in Geology at Lund University*, No. 466, 62 pp. 45 hp (45 ECTS credits).

Abstract: The geochronology of felsic metavolcanic rocks hosting the Bastnäs-type rare earth element (REE) mineralization in the Riddarhyttan area in the Bergslagen region, Sweden, was investigated using Laser Ablation Inductively Coupled Plasma Mass Spectrometry (LA-ICP-MS) U-Th-Pb on zircon and monazite. U-Pb data from four host rock samples yield dates of 1899 ± 4 Ma (MSWD=2.2), 1910 ± 5 Ma (MSWD=3.2), 1911 ± 6 Ma (MSWD=3.2) and 1916 ± 4 Ma (MSWD=1.4). These dates are interpreted as igneous crystallization ages and indicate that several localities with felsic metavolcanic rocks hosting the REE-mineralization are 5 to 10 Myr older than previously known in this part of the Bergslagen region. These dates together with available published geochronology data for metavolcanics in Bergslagen suggest that magmatism might either have formed a continuum or that it was episodic between 1920 to 1876 Ma. A 1824 ± 7 Ma (MSWD=1.2) date for a population of monazite in one of the felsic metavolcanic rocks is temporally correlated with a nearby granite, where variably discordant zircon yield a 1822 ± 10 Ma (MSWD=1.7) date. The monazite and granite dates are overlapping, suggesting that at least part of the monazites in the felsic metavolcanic rocks might have crystallized or recrystallized due to heat and fluids from emplacement and crystallization of granite intrusions during the presumed late Svecofennian phase (c. 1.85-1.78 Ga) of regional metamorphism and ductile deformation. Further geochronological work is required to assess the temporal and geological relationship with the 1820 Ma granite magmatism and the monazite (re-)crystallization. The geochemical characteristics of the metavolcanic rocks are assessed using whole rock (WR) data in conjunction with mass-balance calculations based on the isocon method. The results imply that the felsic metavolcanic rocks hosting the REE-mineralization are mostly consisting of a variably altered rhyolite precursor. WR chemistry data show that geochemical differences among the samples are not the result of fractional crystallization processes. REE patterns are similar to those presented by numerous authors for the Svecofennian volcanic and subvolcanic suite of intrusive rocks (1.91-1.89 Ga) and as stated by earlier workers comparable with those found in a normal to mature, active continental margin. Isocon analyses, using Al_2O_3 , Zr and Hf as immobile elements, indicate that few of the geochemical signals in the felsic metavolcanic rocks are of primary, igneous, origin and instead significant mass gain ranging from +27% to 139% suggests that multiple elements have been gained (e.g. SiO_2 ; MgO , K_2O ; Co; Eu and Fe_2O_3) or lost (Pb; Ni; Zn; Na_2O ; CaO; Th and U) during chemical alteration processes.

Keywords: Riddarhyttan, REE, Metavolcanic rocks, LA-ICP-MS, Zircon, Monazite.

Supervisor(s): Anders Scherstén & Erik Jonsson

Subject: Bedrock Geology

Wictor Linders, Department of Geology, Lund University, Sölvegatan 12, SE-223 62 Lund, Sweden. E-mail: wic_linders@hotmail.com

U-Pb geokronologi och geokemi för med sällsynta jordartsmetaller av Bastnästyp, i Riddarhyttanområdet, västra centrala Bergslagen, Sverige.

WICTOR LINDERS

Linders, W., 2016: U-Pb geokronologi och geokemi för bergarter med sällsynta jordartsmetaller av Bastnästyp, i Riddarhyttanområdet, västra centrala Bergslagen, Sverige. *Examensarbeten i geologi vid Lunds universitet*, Nr. 466, 62 sid. 45 hp.

Sammanfattning: De geokronologiska relationerna för felsiska metavulkaniter med mineraliseringar av sällsynta jordartsmetaller av Bastnästyp i Bergslagen, Sverige, har undersökts med hjälp av Laser Ablation Inductively Coupled Plasma Mass Spectrometry (LA-ICP-MS) U-Th-Pb på zirkon och monazit. Fyra prover ger följande dateringar: 1899 ± 4 Ma (MSWD=2.2); 1910 ± 5 Ma (MSWD=3.2); 1911 ± 6 Ma (MSWD=3.2) och 1916 ± 4 Ma (MSWD=1.4). Dateringarna tolkas som magmatiska kristallisationsåldrar och indikerar att flera lokaler med felsiska metavulkaniter med mineraliseringar av sällsynta jordartsmetaller är 5 till 10 Myr äldre än tidigare dokumenterat i den här delen av Bergslagen. De kombinerade dateringarna från den här och tidigare studier antyder att den vulkaniska aktiviteten antingen var kontinuerlig eller episodisk mellan 1920-1876 Ma. En 1824 ± 7 Ma (MSWD=1.2) datering för en population monaziter skulle kunna korreleras med en starkt diskordant grupp zirkoner från en enskild granit som daterades till 1822 ± 10 (MSWD=1.7). Monazit- och granitdateringarna överlappar, vilket indikerar att åtminstone delar av monaziterna som finns i de felsiska metavulkaniterna kan ha (om-)kristalliserat till följd av värme och fluider från granitiska intrusioner under den förmodade sen-svekokarelska fasen (ca. 1.85-1.78 Ga) av regionalmetamorfos och duktil deformation. Ytterligare geokronologiska undersökningar av främst graniten och monaziterna behövs för att få en bättre insikt i de geokronologiska relationerna. Bergarternas geokemi utvärderades med hjälp av whole rock (WR) analys tillsammans med massbalansberäkningar baserade på isocron-metoden. Resultaten indikerar att de felsiska metavulkaniterna till störst del består av en, i varierande grad, omvandlad ryolitisk ursprungsbergart. Geokemisk data visar att geokemiska skillnader inte beror på fraktionell kristallisation. Resultaten från spårelementstudier är i konsensus med de som publicerats i tidigare studier av felsiska metavulkaniter i Bergslagen och som tidigare föreslagits jämförbara med de signaturer som normalt återfinns vid en normal till mogen, aktiv kontinental plattgräns. Isoconanalyserna, som baserades på att Al_2O_3 , Zr och Hf var immobil element, indikerar att få av de geokemiska signaturerna går att härleda till primära, magmatiska processer. De signifikanta massvinsterna, från +27% till +139% påvisar istället att bergarterna både anrikats (ex. SiO_2 ; MgO, K_2O ; Co; Eu och Fe_2O_3) eller utarmats (ex. Pb; Ni; Zn; Na_2O ; CaO; Th och U) till följd av omvandlingsprocesser.

Nyckelord: Riddarhyttan, sällsynta jordartsmetaller, metavulkaniter, LA-ICP-MS, zirkon, monazit.

Victor Linders, Geologiska institutionen, Lunds Universitet, Sölvegatan 12, 223 62 Lund, Sverige. E-post: wic_linders@hotmail.com

Abbreviations

BIF = Banded iron formation

BSE = Backscattered electron imaging

Ga = Giga annum (billion years)

HFSE = High field strength elements

HREE = heavy rare earth elements

LA-ICP-MS = Laser ablation inductively coupled mass spectrometry

LREE = light rare earth elements

Ma = Mega annum (million years)

n_d = Total number of isotopes (both radiogenic and non-radiogenic)

n_{d0} = Number of non-radiogenic isotopes

n_{d*} = Number of radiogenic daughter isotopes

n_p = Number of parent isotopes

n_{p0} = Number of parent isotopes at the time of crystallization

Nd:YAG = Neodymium-doped yttrium aluminum garnet

r = Correlation coefficient

REE = Rare earth elements

SEM = Scanning electron microscope

t = Time

TIB = Transscandinavian igneous belt

yrs = Years

WR = Whole Rock

λ_p = The decay constant for the parent isotope

1 Introduction

The importance of rare earth elements (REE) in a multitude of modern and emerging technologies has led to a significant increase in demand. As a result of China's present world dominance in REE production and their unpredictable limitations on export quotas, interest in alternative deposits – both old and new – has increased. Recycling of old electronics and industrial components will contribute to the REE supply chain (Binnemans et al. 2013), but does not prove viable and is very unlikely to meet an increase in demand (Du & Graedel 2011). It is therefore expected that mining of REE deposits will continue to be the major source of REE. However, at the time of this MSc thesis there is no on-going REE mining in Europe. Despite the fact that the Fennoscandian shield is one of the most interesting areas for REE exploration within the European Union today (e.g. Goodenough et al. 2016), the Norra Kärr project in southern Sweden is the only project that is reasonably advanced. Yet, this has not always been the case. Historically, REE mining activity in the Fennoscandian shield began already in the mid- to late 1800s in the Bastnäs mines in the western central part of the Bergslagen ore province in Sweden. This is also the location from where the element cerium was originally discovered (Hisinger & Berzelius 1804).

The genesis of the Bastnäs-type deposits is a long-standing matter of debate (e.g. Geijer 1961; Trägårdh 1988, 1991; Ripa 1994; Holtstam & Andersson 2007; Sahlström 2014). The Bergslagen ore province is in general quite well known (cf. Stephens et al. 2009), yet only limited information is available about the crystallization ages of the supracrustal host rocks that, among others, host the Bastnäs REE mineralization. Furthermore, both the exact origin and the timing of formation of the actual mineralization is still somewhat controversial, where both synvolcanic and protracted volcanic and metamorphic processes have been invoked (e.g. Holtstam et al. 2014; Sahlström 2014).

Zircon is a mineral that shows extraordinary capabilities in resisting chemical and mechanical breakdown such as those occurring during increases in temperature and pressure during metamorphism, without any large-scale diffusion of isotopes or elements (Faure & Mensing 2005). Monazite, a relatively common REE-phosphate mineral is contrary to zircon more sensitive to mechanical weathering but in part shares the same ability to withstand large-scale isotope diffusion (Williams et al. 2007). This leads to the fact that both zircon and monazite may preserve their isotopic composition when most other minerals do not and thus makes them suitable for bedrock age dating. The U-Pb system within both zircon and monazite has high closure temperatures, making them useful tools in dating of igneous and metamorphic crystallization ages. Both minerals may contain compositional domains, representing different stages of mineral growth but monazite is, unlike zircon, easily affected by fluid

induced reactions. This gives the two minerals slightly different properties and could enable for a better understanding of the geologic evolution (Faure & Mensing 2005; Williams et al. 2007).

By utilizing micro-imaging techniques such as back-scattered electron (BSE) imaging it is possible to achieve a high degree of textural control during analysis and in the case of complex zoning or the presence of inclusions, the most suitable location of the analytical spot can be selected prior to the analysis. This, in combination with modern high-sensitive analytical techniques, allows control of the geochronological analysis, ensuring both good accuracy and precision.

In this study I combine field observations, petrography, whole rock geochemistry, electron imaging and zircon U-Pb dating of samples from various locations in the Riddarhyttan area in order to constrain the geochemical and geochronological relationships in a suite of felsic metavolcanic rocks that host the REE-mineralizations. In addition to this, a population of monazite was also dated, using U-Pb dating. U-Pb dating was done using a LA-ICP-MS (Laser Ablation Inductively Coupled Plasma Mass Spectrometer). LA-ICP-MS has a number of advantages over other techniques. It is rapid with short analysis time, which makes it cost-effective, yet, the precision loss is less than one order of magnitude compared to that of mineral dissolution analytical techniques (Schoene 2014; Košler & Sylvester 2003). However, no matter how good the method is, if one does not fully understand the mechanisms behind it, the geology of the area studied, the details of the samples as well as the analyzed phases, the end-result may suffer. This work therefore includes descriptions of the geology of the study area, the U-Th-Pb isotope system and of the different analytical techniques used.

nada, Australia and Russia have considerable deposits as well (Humphries 2013).

In recent times REE have risen to the top of EU's list of critical raw materials and the EURARE project, with 23 partners from Europe, has been launched with the goals of characterizing Europe's potential REE resources and to research, develop and improve technologies for extraction of existing resources with minimum environmental impact (www.eurare.eu, 2015). Sweden, Greenland (Denmark), Norway, Finland, Turkey and Greece are countries that have promising potential for REE mining and extraction (Goodenough et al. 2016). In the Fennoscandian Shield, several

occurrences are known; further detailed in table 1 (Goodenough et al. 2016). When occurrences have been listed in table 1, no consideration has been taken to whether or not an actual resource estimation or any previous exploration has been carried out.

2.2 Regional geology

2.2.1 The Fennoscandian shield

The East European craton comprises the Fennoscandian, Sarmatian and Volgo-Uralian crustal segments (Gorbatshev & Bogdanova 1993). The Fennoscandian shield consists of an Archaean core, located in the

Table 1. Known deposit types, their main REE-bearing minerals and locations in Scandinavia (based on Goodenough et al. 2016).

Location	Main REE-bearing mineral(s)/ mineral group(s)	Genetic type
Norway		
Fen	Bastnäsite	Carbonatite
Høgtuva	Zircon, allanite	Hydrothermal
Misværdal	Allanite	Alkaline igneous rock
Seiland Igneous Province	Apatite	Alkaline and carbonatitic rock
Søftestad	Apatite	Pegmatite
Sweden		
Alnö	Apatite, monazite, titanite	Carbonatite
Bastnäs-type	Bastnäsite, cerite, allanite s.l.	Hydrothermal
Grängesberg-Blötberget	Fluorapatite, monazite, allanite, xenotime	Apatite-iron-oxide-
Kiirunavaara (Kiruna-Malmberget)	Fluorapatite, monazite, allanite, xenotime	Apatite-iron-oxide-
Norra Kärr	Eudialyte s.l., catapleiite	Alkaline igneous rock
Olserum	Fluorapatite, monazite, xenotime, allanite s.l.	Hydrothermal
Ytterby group	Gadolinite, yttrantalite, ishikawaite, monazite, xenotime	Pegmatite
Finland		
Halpanen	Apatite, monazite, allanite, ancylite	Carbonatite
Juuka	Apatite, monazite, allanite, ancylite	Carbonatite
Katajakangas	Zircon	Miaskitic igneous rock
Korsnäs	Britholite	Carbonatite
Lamujärvi	Allanite, monazite	Alkaline igneous rock
Iivaara	Apatite, monazite	Alkaline igneous rock
Naantali	Apatite, monazite, allanite, ancylite	Carbonatite
Siilinjärvi	Apatite, REE-fluorocarbonates	Carbonatite
Sokli	Ancylite, apatite, bastnäsite	Carbonatite

north-east, to which a collage of Palaeoproterozoic terranes have been accreted from different plate tectonic settings; volcanic arcs, active continental margins, rifted microcontinents and intervening sedimentary basins (e.g. Gaál & Gorbatshev 1987 and Korja & Heikkinen 2008).

Major rock forming events with igneous activity between 1.95-1.75 Ga has the overall character of an accretionary orogen with crustal growth directed to the south or southwest from the Archaean nucleus (e.g. Gaál & Gorbatshev 1987; Lundqvist et al. 1998; Andersson et al. 2006). The key Palaeoproterozoic orogens of the Fennoscandian Shield are divided into the Lapland-Kola and the Svecofennian/Svecokarelian orogens, where the latter potentially can be further divided into the Lapland-Savo, Svecobaltic, Nordic and Fennian orogens (Lahtinen et al. 2005, 2008).

Rocks in the central part of the Fennoscandian Shield, traditionally called the Svecofennian Domain (e.g. Gaál & Gorbatshev 1987), were variably affected by Svecokarelian/Svecofennian deformation and metamorphism between c. 1.9-1.8 Ga. The southwesternmost parts were to various extent overprinted by Sveconorwegian deformation and metamorphism between 1.0-0.9 Ga, while the western-most parts went through deformation and metamorphism related to the Caledonian Orogeny between 425-395 Ma (e.g. Stephens et al. 2009).

The accumulation of components in the southern and western parts of the Svecofennian Domain was followed by the development of an Andino-type continental margin, creating the voluminous 1.85-1.65 Ga Transscandinavian Igneous Belt (TIB) as well as most-

ly granitoid magmatism (e.g. Andersson et al. 2006 and references therein; Andersson et al. 2004; Högdahl et al. 2004).

The western parts of the Svecokarelian orogen consists of five distinct components: (1) the active continental margin volcano-sedimentary Skellefte district, (2) the tectonically stacked marine basin (Bothnian Basin), (3) granitoids from the continental margin (Ljusdal batholith of the Ljusdal Domain), (4) a possible island-arc fragment (Hamrånge formation) and (5) the continental back-arc volcano-sedimentary Bergslagen Region. These components have been tectonically characterized using several different criteria (e.g. Högdahl et al. 2009; Högdahl et al. 2012). Gaál & Gorbatshev (1987) used lithology; Romer & Wright (1993) used lead isotope compositions; Sjöström & Bergman (1998) used lithology in combination with structural form lines; Hermansson et al. (2007) used geochronology (“tectonic” domains) while Lahtinen et al. (2005) used all these criteria together with crustal geophysics. The boundaries between the different terranes typically coincide, regardless of criteria used, and ductile shear zones usually define them (Högdahl 2009).

2.2.2 The Bergslagen region

2.2.2.1 Geology

The Bergslagen ore province (Fig. 2) is a major volcano-metallogenetic province with abundant mineralizations of several types, primarily containing base metals (Cu, Pb, Zn) and iron oxides (e.g. Tegengren 1924; Geijer & Magnusson 1944; Magnusson 1970; Stephens et al. 2009). The main ore-bearing units in

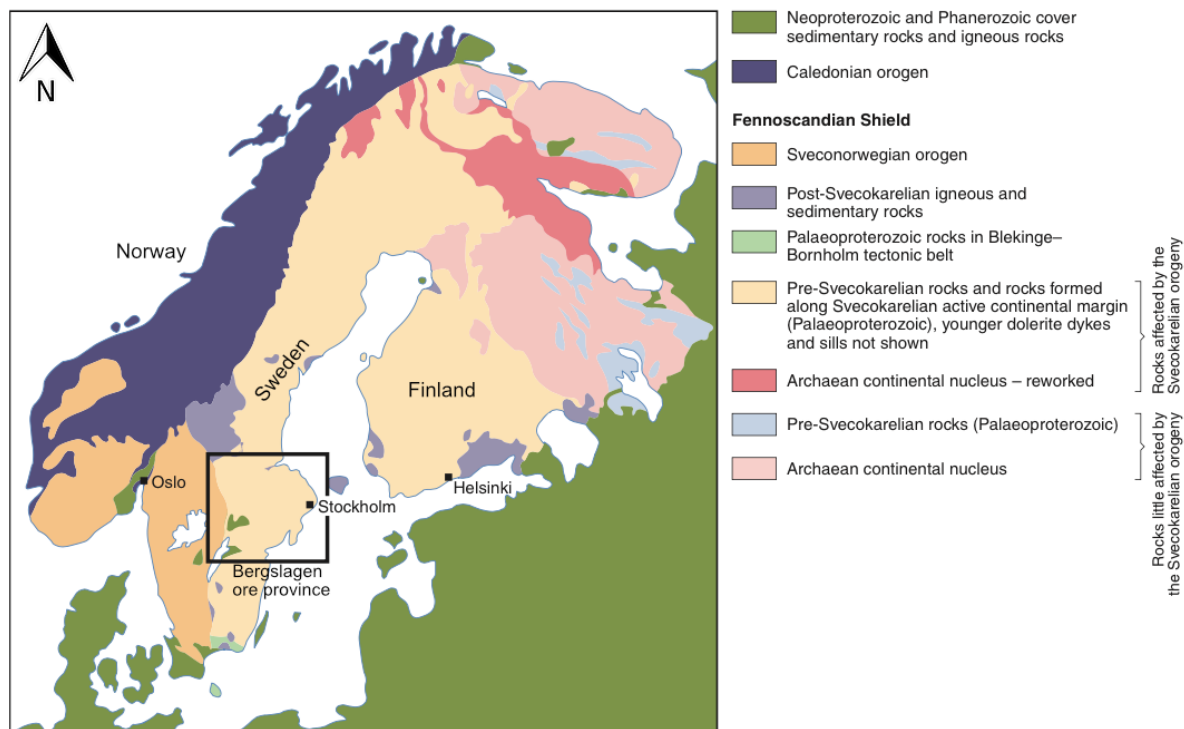


Fig 2. Map showing the general geological units of the Fennoscandian Shield. Dark frame outlines the Bergslagen ore province. Modified from Stephens et al. 2009.

the Bergslagen ore province are dominantly rhyolitic to rhyodacitic, alkali-rich metavolcanic rocks, occurring together with intercalated minor volumes of metabasic rocks, clastic metasedimentary rocks and marbles (e.g. Stephens et al. 2009). The metavolcanic rocks are of a predominantly felsic pyroclastic nature and were to various degrees hydrothermally altered during the synvolcanic stage (e.g. Allen et al. 1996; Lundström, 2004). This alteration resulted in widespread metasomatic redistribution of several elements, particularly K, Na and Mg and ultimately formation of rocks enriched in one of the three elements and depleted in others (e.g. Frietsch 1982; Lagerblad 1988, Trägårdh 1988; Hallberg 2003). The clastic metasedimentary rocks that occur associated with the metavolcanic units are mostly metapsammites and metapelites (e.g. Stephens et al. 2009).

The supracrustal rocks underwent polyphase deformation and LP-HT greenschist to amphibolite facies metamorphism during the Svecokarelian orogeny (e.g. Ripa, 1994; Stephens et al. 2009). These rocks were also intruded by several generations of plutonic rocks. Of these, the older, early Svecokarelian (c. 1.90-1.85 Ga) suite is commonly foliated and have tonalitic to granodioritic to granitic compositions (e.g. Hermansson et al. 2008; Stephens et al. 2009). The younger, (c. 1.81-1.75 Ga; e.g. Öhlander & Romer 1996) suite is late- to post-tectonic and consists of basically undeformed or homogenous granites sensu stricto (e.g. Zuber & Öhlander 1991; Andersson & Öhlander 2004). The region probably underwent metamorphism and ductile deformation during two main phases; (1) an early Svecokarelian phase (>1.85 Ga; Andersson et al. 2006, Hermansson et al. 2008) and (2) a late Svecokarelian phase (c. 1.85-1.78 Ga; Andersson 1997; Stephens et al. 2009). However, in many areas, only a general age of metamorphism, around c. 1.85-1.80 Ga can be observed. Minor mafic rocks (gabbro, etc.) with similar ages as phase (1) are typically related to the early granitoids. Granites and pegmatites post-dating the (c. 1.85-1.80 Ga) regional metamorphism are abundant. Younger, post-Svecofennian tectonic stress caused brittle deformation and formation of faults and fractures (e.g. Allen et al. 1996 and references therein).

Most of the base metal and iron oxide mineralizations in the region are found in the felsic metavolcanic rocks and in particular within the interlayered carbonate/skarn rocks. The skarn rocks are compositionally variable Fe,Mg- and/or Mn-bearing calc-silicate assemblages, which formed either as the result of regional metamorphism of impure carbonate rocks or during metasomatism of carbonate rocks involving granite-derived fluids rich in silica and various other constituents (e.g. Jansson 2011 and references therein).

Based on the geochemistry of the Svecofennian 1.91-1.89 Ga metavolcanic rocks, Löfgren (1979) and Loberg (1980) suggested that the Bergslagen region formed as a volcanic arc situated above a subduction zone. This was disputed by e.g. Oen et al. (1982), van

der Velden et al. (1982) and Oen (1987), who instead argued that the western part of the region was created in a continental rift setting. Allen et al. (1996) proposed that the 1.91-1.89 Ga volcanism and deposition of iron oxide and Zn-Pb-Ag sulfide deposits were related to an extensional back-arc setting next to an active continental margin. Allen et al. (1996) visualized a tectonic evolution of cyclic nature, through “stages of intense magmatism, thermal doming, and crustal extension, followed by waning extension, waning volcanism, thermal subsidence, reversal from extension to compressional deformation, regional metamorphism, and structural inversion.”

2.2.2.2 Tectonic evolution models

According to Stephens et al. (2009), the 1.9-1.8 Ga tectonic evolution is best explained by a model featuring a convergent plate setting, because of both the geochemical character of the igneous rocks and due to the interaction between volcanic activity, metamorphism and deformation. In addition to this, they suggest that Sm-Nd data and U-Pb (zircon) geochronology are indicative of the existence of a juvenile, pre-1.91 Ga crust in the Bergslagen region. There is also abundant evidence for the presence of mature, older continental material (Jonsson & Billström 2009 and references therein).

Hermansson et al. (2008) applied a “migratory tectonic switching” model that could account for the cyclic nature of the tectonic evolution (Fig. 3) and which is consistent with the continental back-arc setting proposed by Allen et al. (1996). A description of the tentative older cycle between 1.91-1.86 Ga, which involved an extended period of transtensional tectonics, replaced by a short period of transpression, followed by renewed transtension is given below.

This particular model, like several earlier ones, is based on a north-east dipping subduction zone, located to the south-west of a continent, with a subduction zone hinge-line that retreated during 1.91-1.89 Ga, causing back-arc extension and bimodal volcanism (in agreement with Allen et al. 1996), subsequently followed by sedimentation and calc-alkaline igneous activity. Between 1.89-1.87 Ga, the subduction zone hinge-line retreatment ceased and changed direction with decreasing extension as a result. Meanwhile, major igneous activity changed from being calc-alkaline (1.89-1.88 Ga) to more alkali-calcic character (1.88-1.87 Ga). The now advancing subduction zone hinge-line led to compression in the back-arc region. A renewed reversal in the direction of the subduction zone hinge-line occurred at approximately 1.86 Ga that once again led to back-arc extension and magmatism.

The model of Hermansson et al. (2008), supported by e.g. Stephens et al. (2009) and Bogdanova et al. (2015), accounts for the occurrence of older crust, probably created during a similar but earlier cycle and also for the accretionary character of the Svecokarelian orogen, but it is in strong contrast with the concept for

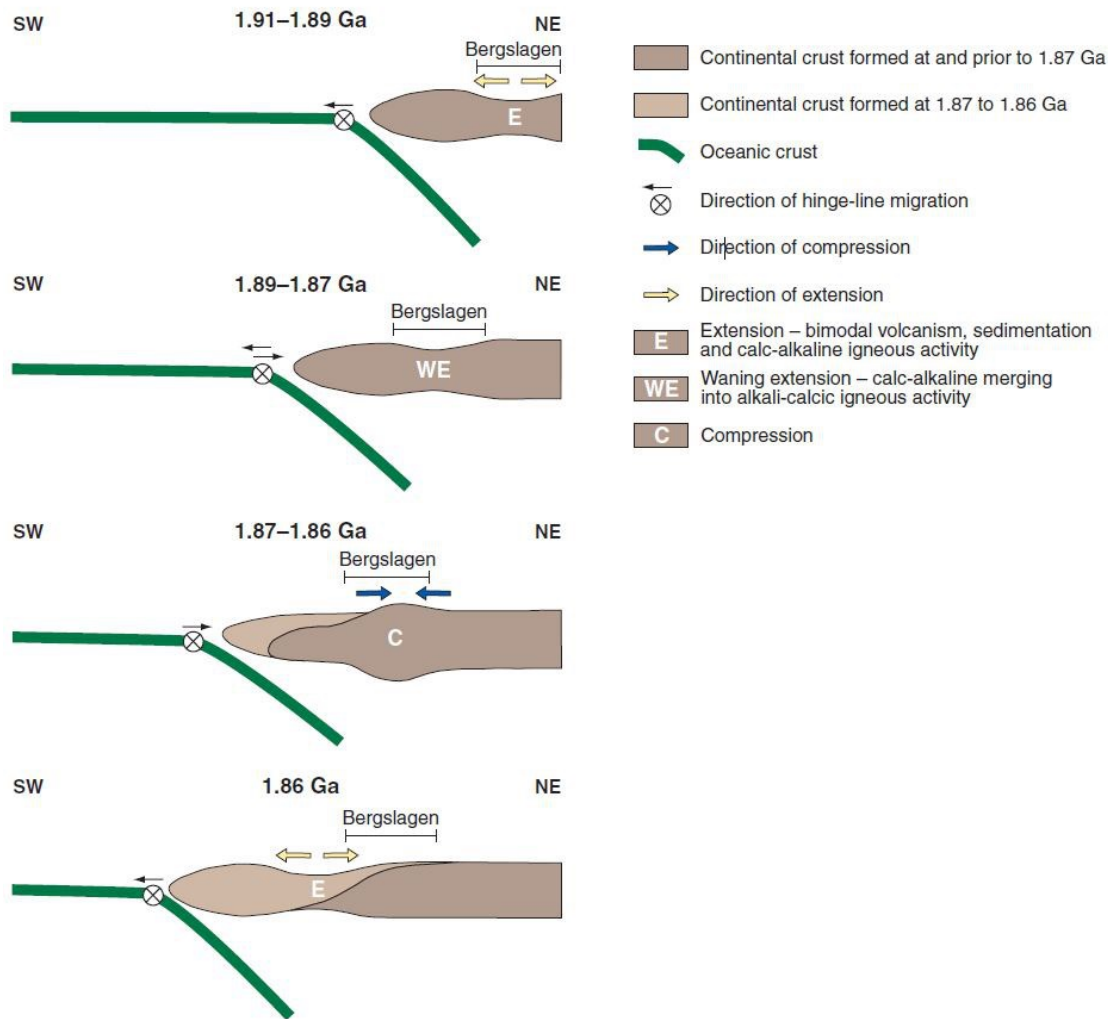


Fig 3. Conceptual tectonic switching model showing the tectonic evolution of the Bergslagen region between 1.91-1.86 Ga. Retreat or advance of the subduction zone hinge-line causes extensional or compressional regimes. From Stephens et al. 2009.

the tectonic evolution of the Fennoscandian Shield put forward by e.g. Nironen 1997; Lahtinen et al. 2005, 2008, 2014 and Beunk & Kuipers 2012; whose models are instead based on microplate tectonics and fast arc-accretion associated with subduction of oceanic crust in alternating directions.

2.3 Geology of the REE-line in western central Bergslagen

Mining activity in the Fennoscandian Shield with focus on REE first occurred in the mid- to late 1800s in the Bastnäs mines, outside Riddarhyttan, in the central part of the Bergslagen region (Jonsson et al. 2014 and references therein), notably the locality where the element cerium was first discovered (e.g. Hisinger & Berzelius, 1804). The Bastnäs-type deposits (Fe-REE-(Cu-Mo-Bi-Au)) (Geijer 1961) are located along a more than 100 km long, narrow zone, the REE-line (Jonsson & Högdahl 2013; Fig. 4). The host rocks have a foliation that is mainly dipping moderately to steeply eastwards and are suggested to represent the core of an antiform (Strömberg 1980). The zone is

regarded as a geological “anomaly” because of its substantial enrichment in mostly LREE but to some extent also in yttrium and HREE. The metavolcanic host rocks and their interlayered carbonate units host numerous iron oxide skarn deposits as well as banded iron formations (BIF). Some of the skarn deposits are rich in REE whereas others are not. These mineralizations are mainly found within horizons of marble within the metavolcanic rocks. The metavolcanic rocks were hydrothermally altered close to the iron oxide skarn deposits during regional metamorphism and are now andalusite and/or cordierite-bearing mica schists or quartzites (Geijer & Carlborg 1923; Ihre & Sädbom, 1986). Smaller, ductile folds have been observed in some parts of the REE-line. This together with the observation that REE mineral assemblages in the deposits are folded and recrystallized suggests that the mineralizations formed during an early stage of the orogenic evolution (Jonsson & Högdahl 2013).

The deposits in the southern and central parts of the REE line are concentrated around Nora and Riddarhyttan while the deposits in the northern parts are

mainly found close to Norberg (Jonsson & Högdahl 2013). Holtstam & Andersson (2007) subdivided the Bastnäs-type deposits into two subtypes, based on REE geochemistry and paragenesis (table 2).

In subtype 1, represented by the Rödbergsgruvan and Bastnäs deposits, dominant REE minerals are cerite-(Ce), bastnäsite-(Ce) and ferriallanite-(Ce). Prevailing REE minerals in subtype 2 are dollaseite-(Ce), dissakisite-(Ce), fluorbritholite-(Ce) and Y-dominant species, found in deposits in the Norberg area. There is thus an enrichment of LREE in subtype 1 and enrichment in both LREE and Y+HREE in the subtype 2. Gangue mineral in subtype 1 is dominantly tremolite-actinolite, compared to norbergite, chondrodite, fluorite and fluorophlogopite in subtype 2. In addition to this, associated sulfide mineralizations are more abundant in subtype 1 (Holtstam & Andersson

2007; cf. also Jonsson et al. 2014).

How the Bastnäs-type deposits have formed has together with the chronological relations between REE mineralizations and host rocks been a question of debate. The deposits, together with associated skarn iron ores, were originally interpreted to have formed due to large-scale Mg-metasomatic processes that formed during granitoid intrusions synchronous with fading regional metamorphism (Geijer & Magnusson 1944; Geijer 1961; Magnusson 1970). Several later authors refuted this and presently, a scenario with synvolcanic interaction between essentially magmatic-derived hydrothermal fluids and pre-existing limestone is suggested to be most likely (e.g. Sahlström et al. 2014; Holtstam & Andersson 2014; Jonsson et al. 2014; Jonsson & Högdahl 2013; Holtstam & Andersson 2007).

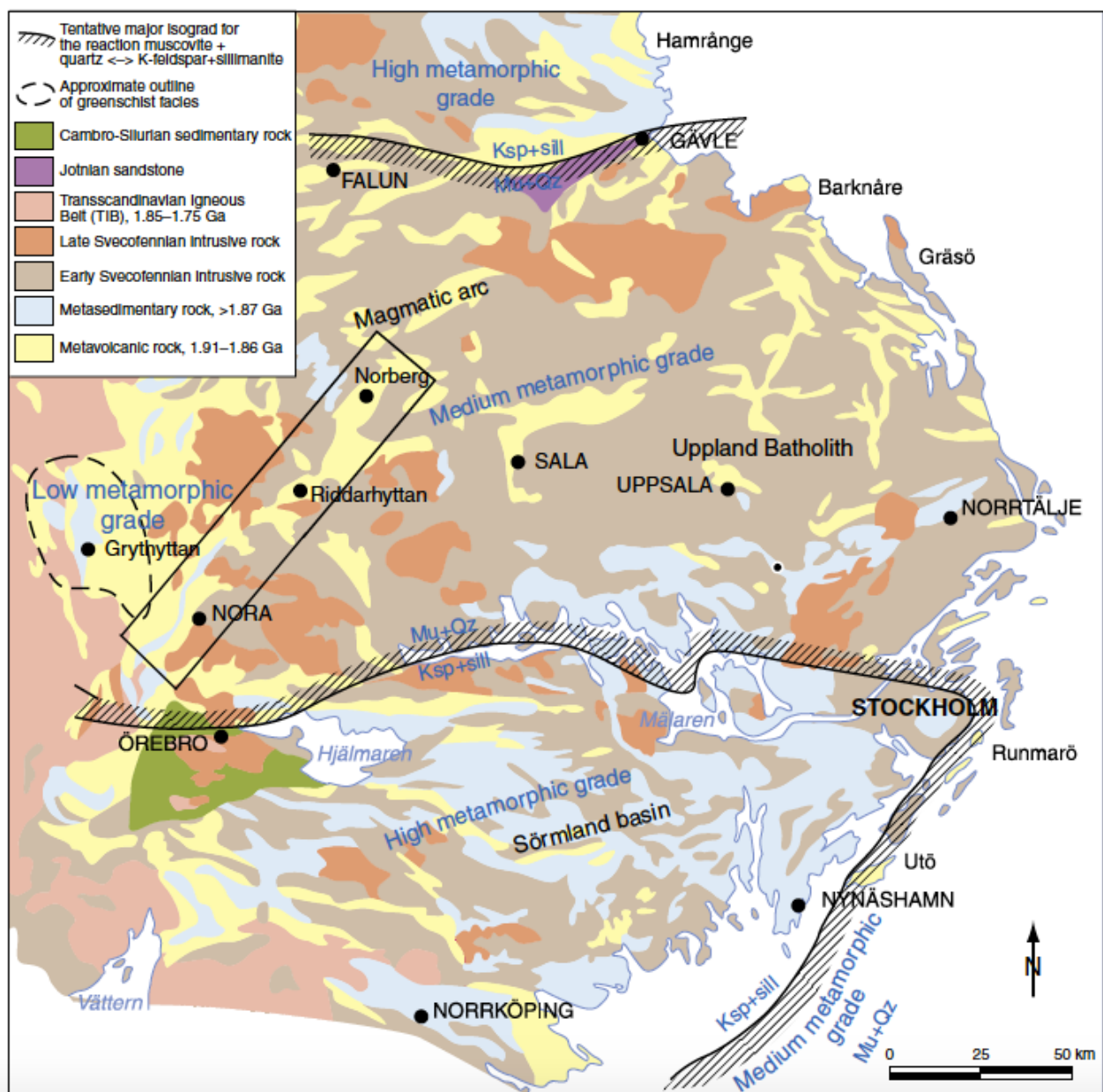


Fig. 4. Geological overview of the Bergslagen region. The rectangular frame essentially outlines the REE-line of Jonsson & Högdahl 2013. From Andersson (2004).

Table 2. Presently known REE minerals in the Bastnäs-type deposits together with their chemical formulae and occurrence. From Holtstam et al. 2014 and Jonsson et al. 2014.

Name	Chemical Formula	Subtype 1	Subtype 2
Allanite-(Ce)	(Ce,La)CaFe ²⁺ Al ₂ [Si ₂ O ₇][SiO ₄]O(OH)	X	X
Bastnäsite-(Ce)	(Ce,La)CO ₃ F	X	X
Bastnäsite-(La)	(La,Ca)CO ₃ F	X	
Cerianite-(Ce)	CeO ₂	X	
Cerite-(Ce)	(Ce,La,Nd) ₉ (Mg,Fe)Si ₇ O ₂₄ (O,OH,F) ₇	X	X
Dissakisite-(Ce)	Ca(Ce,La)MgAl ₂ [Si ₂ O ₇][SiO ₄]O(OH)	X	X
Dollaseite-(Ce)	Ca(Ce,La)Mg ₂ Al[Si ₂ O ₇][SiO ₄]F(OH)		X
Ferriallanite-(Ce)	(Ce,La)CaFe ²⁺ AlFe ³⁺ [Si ₂ O ₇][SiO ₄]O(OH)	X	
Fluocerite-(Ce)	(Ce,La)F ₃	X	
Fluocerite-(La)	(La,Ce)F ₃	X	
Fluorbritholite-(Ce)	(Ce,La) ₅ [SiO ₄] ₃ F		X
Fluorbritholite-(Y)	(Y,REE) ₅ [SiO ₄] ₃ F		X
Gadolinite-(Ce)	(Ce,La) ₂ Fe ²⁺ Be ₂ Si ₂ O ₁₀	X	X
Gadolinite-(Y)	(Y,REE) ₂ Fe ²⁺ Be ₂ Si ₂ O ₁₀		X
Håleniusite-(La)	(La,Ce)OF		
Magnesorowlandite-(Y)	(Y,REE) ₄ MgSi ₄ O ₁₄ F ₂		X
Monazite-(Ce)	(Ce,LREE)PO ₄		
Parisite-(Ce)	Ca(La,Ca) ₂ ((CO ₃) ₃)F ₂		X
Percleveite-(Ce)	(Ce,La) ₂ Si ₂ O ₇	X	
Törnebohmitte-(Ce)	(Ce,La) ₂ Al[SiO ₄] ₂ (OH)	X	
Västmanlandite-(Ce)	Ca(Ce,La) ₃ Al ₂ Mg ₂ [Si ₂ O ₇][SiO ₄] ₃ F(OH) ₂		X

Holtstam et al. (2014) suggests that there is still some agreement with the old hypothesis: "...The age span and rock association argues for protracted mineralization from mainly magmatic fluids circulating through an extensive volcano-plutonic complex in several pulses, initially in a dominantly volcanic environment and later by convection driven by plutonic activity somewhat deeper in the juvenile crust."

Holtstam et al. (2014) also suggested that the REE mineralization in the Bastnäs-type deposits formed, beginning at 1.9 Ga, from predominantly Svecofennian, juvenile igneous (>400°C) fluids transporting Si, F, Cl, S, CO₂, REE and various other metals. This is in line with Sahlström (2014) and Sahlström et al. (2015) who, using stable isotope systematics, concluded that REE-associated magnetite mineralizations in the REE-line formed from essentially magmatic, 400-650°C fluids.

2.4 Geochronology in Bergslagen and the REE-line

Stephens et al. (2009) compiled geochronological data

for the Bergslagen area (Fig. 5). A summary of the ages for the suite of "Svecofennian volcanic and sub-volcanic intrusive rocks" of Stephens et al. (2009) is shown in table 3. Only limited age dating has been done within the rock units of the REE line. A few attempts using different methods yielded varied results. Welin (1963) dated uraninite using U-Pb; Holtstam et al. (2014) dated molybdenite with Re-Os and REM with Sm-Nd, and Sahlström (2014) did chemical U-Pb dating of uraninites, where the results range from c. 1.6-1.9 Ga (table 4).

3 Principal and applied analytical methods

3.1 Sampling and separation of minerals for geochronology

3.1.1 Sample collection

Eleven rock samples were collected during three

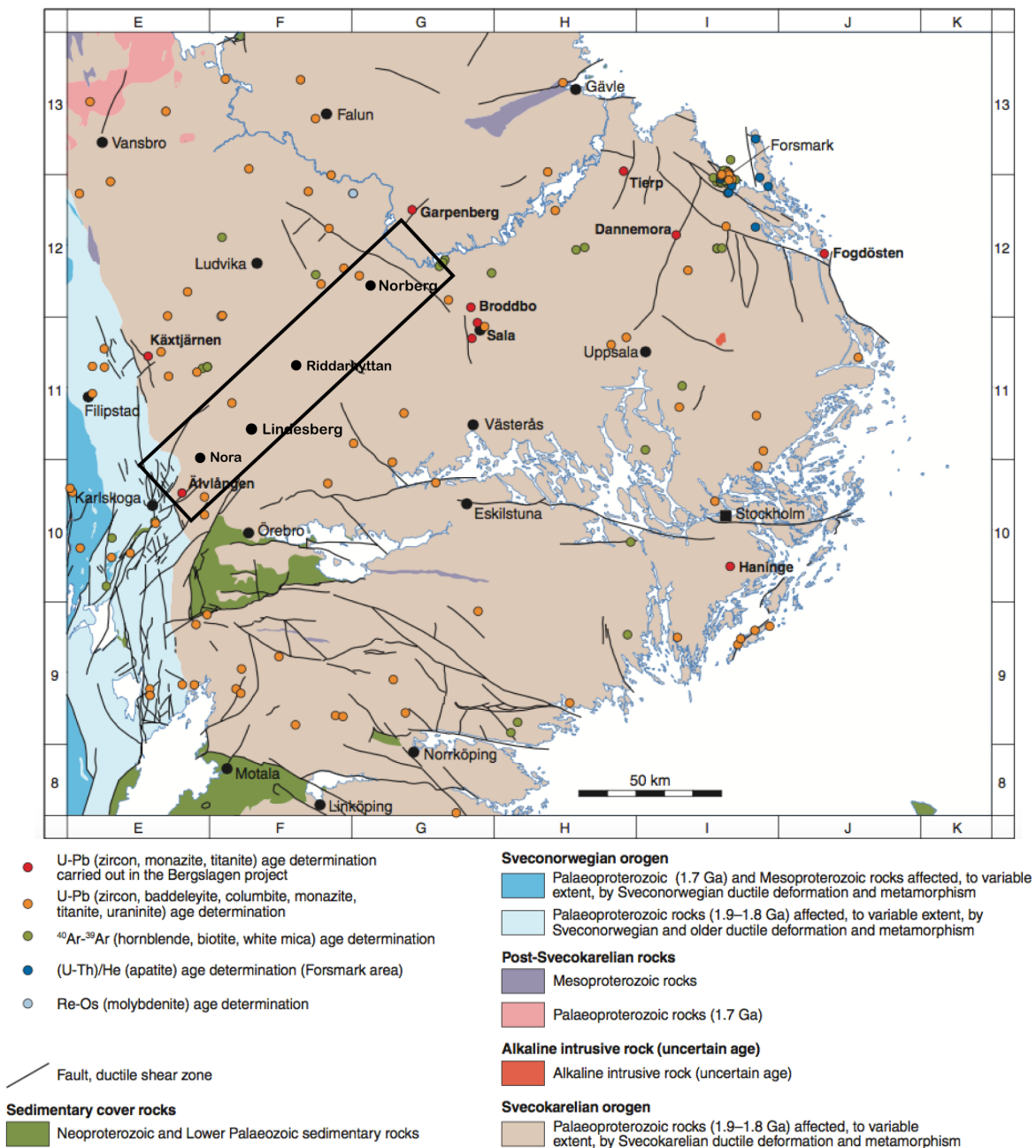


Fig. 5. Geochronology of the Bergslagen province. Colored points represent locations where radiometric age dating has been conducted. Note that only published ages or ages acquired in the “Bergslagen project” are shown. Ages with uncertainties larger than ± 20 Ma are omitted. Results from age dating conducted after 2009 are not shown. Black frame outlines the REE line of Jonsson & Högdahl (2013). Modified from Stephens et al. 2009.

sampling rounds in 2015, eight during the first, two during the second and one during the third (Fig. 6). Eight of these (KES150001-0008) were sent to Bureau Veritas (former Acme Labs) in Vancouver, BC, Canada, for whole rock (WR) major- and trace element analyses. Results from the WR-analyses are shown in Appendix I. Zircon and monazite for geochronology were separated out of these samples. Rock chips were sawed and sent to Geological Institute, Slovak Academy of Sciences (SAS) for manufacture of thin sections. For further information about the different samples see section 4 *Samples and petrography*.

3.1.2 Zircon and monazite separation

Separation of zircon and monazite for U-Pb dating was done by first crushing and then grinding the samples in a steel mill into smaller fractions. This was followed by heavy minerals separation on a Wilfley shaking table following Söderlund and Johansson (2002). Magnetic fractions were removed with a handheld magnet before zircon and monazite were hand-picked from the remaining heavy minerals under a binocular microscope. Between 50-100 grains were picked from each sample and placed on double-sided tape before cast into standard 1 inch cylindrical epoxy mounts. The epoxy mounts were polished to expose cross sect-

Table 3. Selected U-Pb zircon ages (SIMS or TIMS) for the Svecofennian volcanic and subvolcanic intrusive rocks found in the Bergslagen region (Stephens et al. 2009 and references therein). Ages with uncertainties larger than ± 20 Ma are omitted. Coordinates are given in WGS-84 dec.

Lithology	Method	Age (Ma)	N	S	Reference
Metarhyolite (mass flow)	U-Pb zircon (TIMS)	1906 \pm 3	59,997506°	16,561444°	Stephens et al. 2009
Metarhyolite (mass flow)	U-Pb zircon (TIMS)	1904 \pm 4	58,969000°	18,364351°	Lundström et al. 1998
Metarhyolite	U-Pb zircon (TIMS)	1901 \pm 18	58,898364°	15,365406°	Kumpulainen et al. 1996
Metarhyolite (mass flow)	U-Pb zircon (TIMS)	1897 \pm 6	59,839002°	14,534202°	Stephens et al. 2009
Metarhyolite (mass flow)	U-Pb zircon (TIMS)	1896 \pm 2	59,410145°	14,759969°	Stephens et al. 2009
Amphibolite	U-Pb zircon (SIMS)	1895 \pm 5	60,248165°	15,666089°	Andersson et al. 2006
Metarhyolite (ash-fall, tuff)	U-Pb zircon (TIMS)	1894 \pm 2	59,899604°	16,564491°	Stephens et al. 2009
Metarhyolite (mass flow)	U-Pb zircon (TIMS)	1894 \pm 4	60,211772°	17,866915°	Stephens et al. 2009
Metarhyolite	U-Pb zircon (TIMS)	1892 \pm 6	59,801608°	14,261243°	Welin 1987
Metaporphyry (subvolcanic intrusion)	U-Pb zircon (TIMS)	1892 ⁺⁵ ₋₄	59,948217°	16,601389°	Stephens et al. 2009
Volcanic supra-crustal rock	U-Pb zircon (SIMS)	1892 \pm 7	60,233187°	18,186029°	Andersson et al. 2006
Metarhyolite (mass flow)	U-Pb zircon (TIMS)	1891 \pm 4	59,776996°	14,664034°	Lundström et al. 1998
Metarhyolite	U-Pb zircon (TIMS)	1891 \pm 10	59,893148°	17,534450°	Welin 1987
Metarhyolite (mass flow)	U-Pb zircon (TIMS)	1891 \pm 2 (UI, 4 fractions); 1823 \pm 7 (²⁰⁷ Pb/ ²⁰⁶ Pb age, 1 fraction)	60,306013°	16,194022°	Stephens et al. 2009
Felsic metavolcanic rock	U-Pb zircon (SIMS)	1888 \pm 12	60,098728°	17,935368°	Andersson et al. 2006

Table 4. Geochronology previously conducted in the REE-line.

Locality	Method	Age (Ma)	Uncertainty $\pm 2\sigma$ (Ma)	# of datings	Reference
Rödbergsgruvan, Bastnäs, S. Hackspiksgruvan	Re-Os on Mlb	1,837-1,910	6-9	3 samples, each run in duplicate	Holtstam et al. 2014
Bastnäs	Sm-Nd on REE-minerals.	1875	110	6	Holtstam et al. 2014
Östra Gyttorpsgruvan	Chemical dating of uraninites.	1623-1898	3	24	Sahlström, 2014
Bastnäs	U-Pb mass spectrometry on uraninites	1760	-	1	Welin, 1963; 1980.

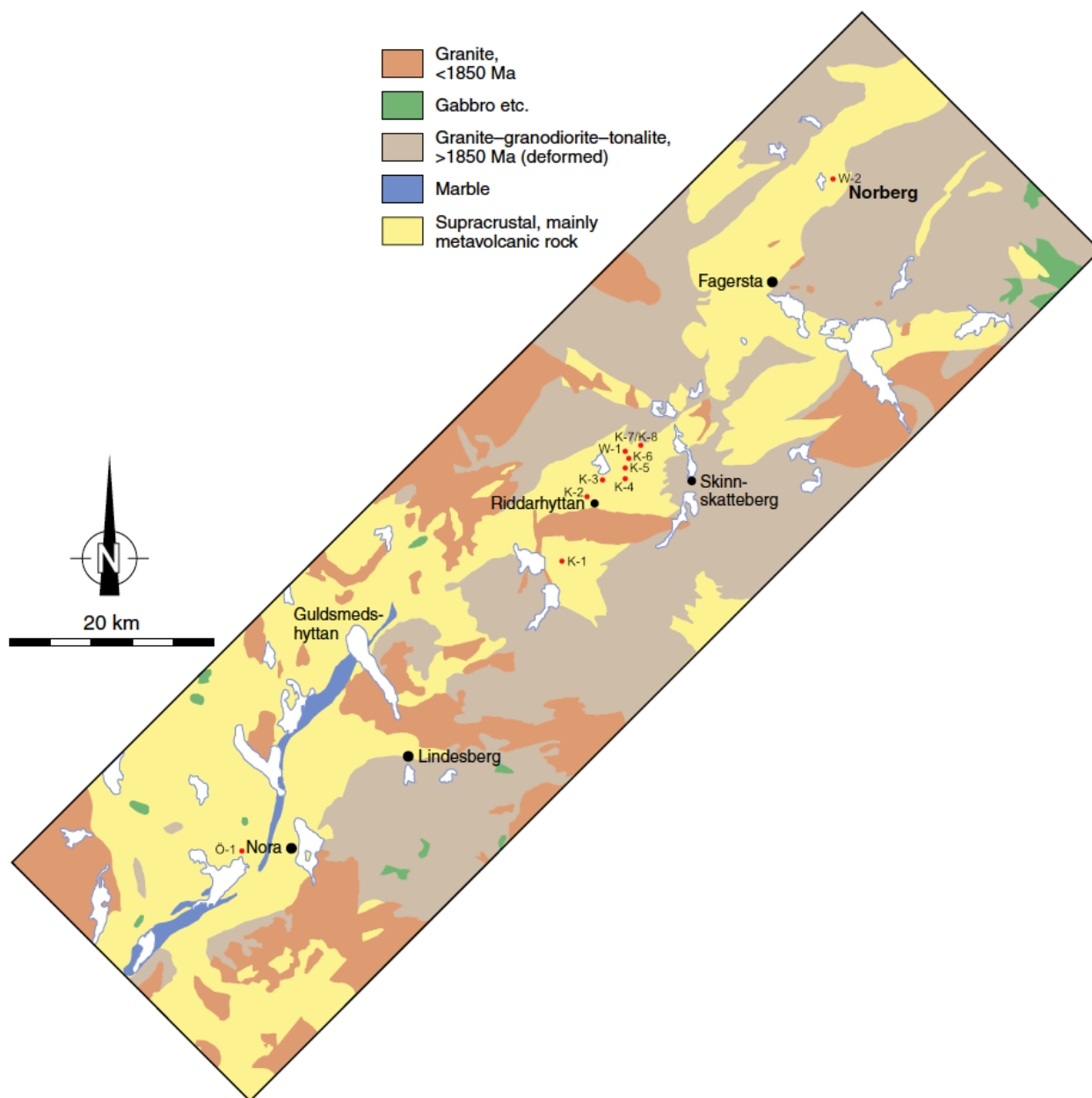


Fig. 6. Geologic bedrock map showing the area with Bastnäs-type deposits. Samples Ö-1 = Ö. Gytt-1; K-1 to K-8 = KES150001 to KES150008; W-1 to W-2 = WL15001 to WL15002. Modified from Andersson (2004).

ions of the crystals.

3.1.3 Scanning electron microscope (SEM) and backscattered electron (BSE) imaging

The epoxy mounts were coated with carbon and placed in a scanning electron microscope (SEM) at the Department of Geology, Lund University for high magnification imaging of the zircons and monazites. A SEM fires a high-energy electron beam on the sample, producing a wide range of secondary features, e.g. backscattered electrons (BSE) that were used in this study (Egerton 2005). In BSE mode, heavy elements appear brighter than light ones, a feature which is especially useful when trying to find inclusions or uranium (or other heavy elements) rich/poor domains in zircons and monazites. The images produced were

used for determination of where to place analytical LA-ICP-MS (laser ablation inductively coupled plasma mass spectrometer) spots. The aim of this work is, in essence, to find areas free from inclusions, fractures and zonation.

3.2 Overview of minerals used for geochronology

3.2.1 Zircon

Zircon ($ZrSiO_4$) is highly used in geochronology as it is a common accessory mineral in many different sedimentary, igneous and metamorphic rocks, it incorporates significant amounts of U and Th, it has a high closing-temperature $>900^\circ C$, and it is physio-chemically very resistant (e.g. Finch & Hanchar 2003; Faure &

Mensing 2005; Lee et al. 1997).

3.2.2 Monazite

Monazite ((Ce,LREE)PO₄) is a LREE-bearing phosphate that occurs in a wide range of rocks, incorporates among many other elements U and Th in its crystal structure and has very slow diffusion rates. Monazite is increasingly being used as a mineral for geochronology (Williams et al 2007).

3.3 Geochronology – basics and applications

3.3.1 The U-Th-Pb system

3.3.1.1 General overview

The method of using U-Pb for age dating of geological materials dates back more than a century. Arthur Holmes pioneered radiometric dating with his paper "The association of lead with uranium in rock-minerals and its application to the measurement of geological time" (Holmes 1911). This and subsequent work carried out by numerous authors (e.g. Barrel 1917; Bateman 1910; Soddy 1913) focusing on examining the

nature of isotopes and U decay helped to establish one of the most important geological dating systems in use today.

Pb has four naturally occurring stable isotopes: ²⁰⁴Pb, ²⁰⁶Pb, ²⁰⁷Pb and ²⁰⁸Pb, where the last three are produced from the radioactive decay of: ²³⁸U, ²³⁵U and ²³²Th, each with an independent decay chain. Minerals rich in U are fairly common in many rock types. This may together with the fact that these minerals can withstand physical and chemical weathering contribute to the popularity of the U-Pb system (Schoene 2014). Zircon is the most commonly used mineral in U-Pb dating but monazite, apatite, xenotime, titanite, rutile, baddeleyite, perovskite and allanite are also used and can provide thermochronological information about igneous, metamorphic and hydrothermal processes (Schoene 2014 and references therein). The half-lives of the three parent isotopes are long enough for establishing time constraints for various important geological processes such as the formation of the solar system, rates of crustal formation, paleogeographic reconstructions and so on (table 5; Schoene 2014).

None of the three parent isotopes decays directly to the stable lead isotope, but follow three different

Table 5. Daughter isotopes, half-lives and decay constants for ²³²Th, ²³⁵U and ²³⁸U.

Parent isotope	Daughter isotope	Half-life (yr)	Decay constant (λ)	Reference
²³² Th	²⁰⁸ Pb	14.010x10 ⁹	4.9475x10 ⁻¹¹	LeRoux et al. (1963)
²³⁵ U	²⁰⁷ Pb	0.7038x10 ⁹	9.8485x10 ⁻¹⁰	Jaffey et al. (1971)
²³⁸ U	²⁰⁶ Pb	4.468x10 ⁹	1.5513x10 ⁻¹⁰	Jaffey et al. (1971)

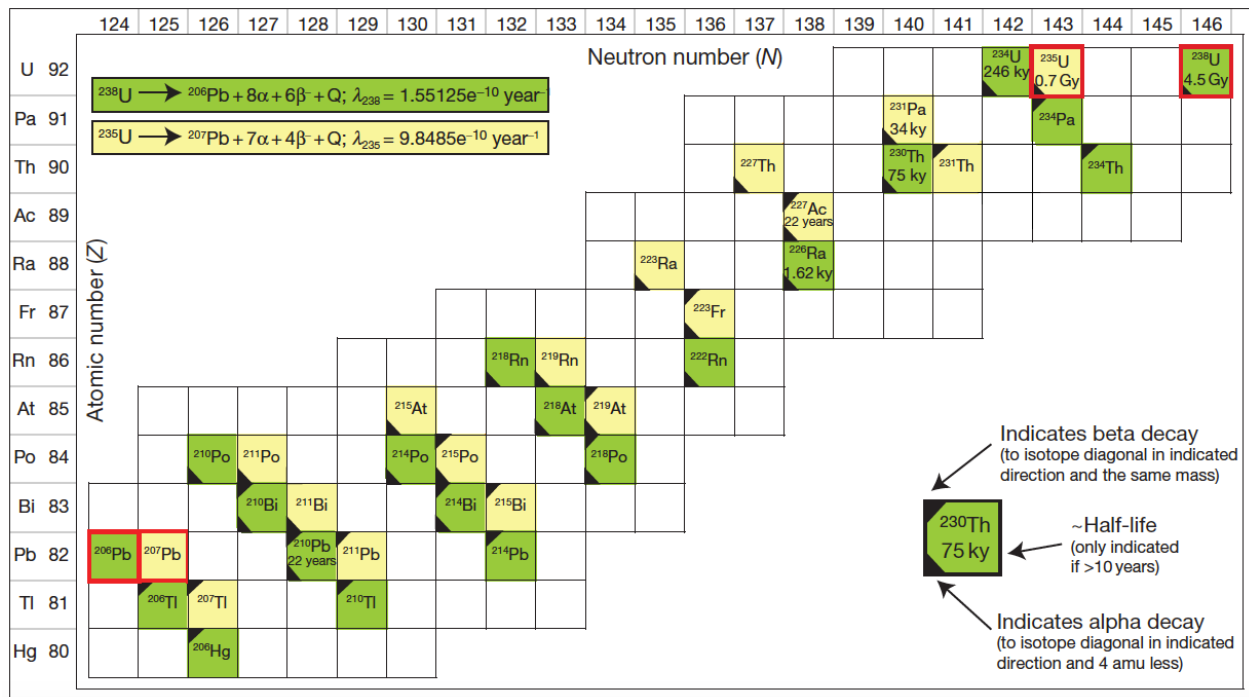


Fig. 7. Illustration of the three different decay chains for ²³⁸U, ²³⁵U in the U-Pb system. Parent and stable daughter isotopes are outlined in red. The isotopes are color-coded following the parent isotope where yellow = ²³⁵U and green = ²³⁸U. α indicates alpha decay, β is beta decay and Q is energy released during decay. See inset for further information concerning symbols in each box. Modified from Schoene (2013).

decay series, passing through intermediate radioactive daughter isotopes during alpha or beta decay (Fig. 7 outlines the decay chains for ^{238}U and ^{235}U). Note that the half-life of each intermediate daughter isotope is much shorter than that of the parent isotope.

In order to fully comprehend the decay chains a concept called secular equilibrium is used. The decay chain is in secular equilibrium when the abundance (in mole) of an isotope multiplied with its decay constant equals to that of the parent isotope and all the daughter isotopes, see equation 1.

$$N_1\lambda_1 = N_2\lambda_2 = N_3\lambda_3 = \dots \quad (1)$$

This can be rewritten using the common nomenclature for isotope activity, which describes the decay rate of the isotope:

$$[N_1] = [N_2] = [N_3] \quad (2)$$

As soon as the system is in secular equilibrium it will remain that way until one or several of the isotopes in the decay chain is fractionated away from the rest. Causes for secular disequilibrium can be igneous fractionation or chemical weathering. If a system is in secular disequilibrium then the simplified equations are no longer valid and the calculated age will be incorrect which is shown in Fig. 8. However, secular equilibrium is generally assumed for e.g. zircon geochronology (Schoene 2014).

3.3.1.2 Age equations

Hodges (2003) describes radioactive decay as the spontaneous process when one parent isotope is transformed into a daughter isotope (in the equations below

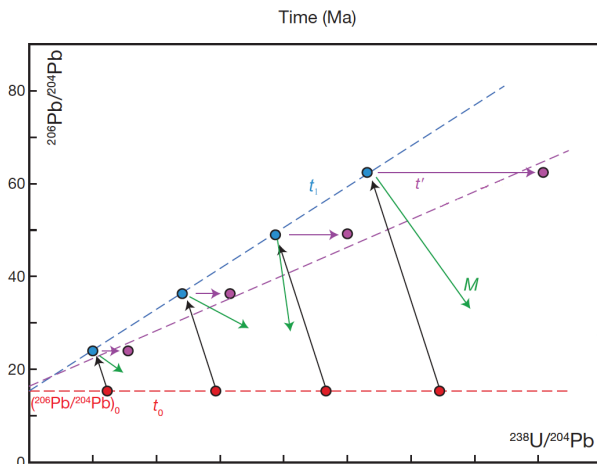


Fig 8. Example of an isochron diagram for the U-Pb system. At t_0 a suite of minerals crystallize with identical $^{206}\text{Pb}/^{204}\text{Pb}$ but different $^{238}\text{U}/^{204}\text{Pb}$ ratios. At t_1 , radioactive decay increased the $^{206}\text{Pb}/^{204}\text{Pb}$ ratio but since the starting points were different the end point are different as well. Purple lines symbolize Pb loss whereas green represent mixing with younger and/or less radiogenic material. Modified from Schoene, (2014).

secular equilibrium is assumed). The rate at which this occurs is proportional to the number of parent isotopes in the rock/mineral at a given time:

$$\frac{-dn_p}{dt} = \lambda_p n_p \quad (3)$$

where: n_p = number of parent isotopes, t = time and λ_p = the decay constant for the parent.

After integration, this new equation will tell the number of the parent isotopes at a given time as a function of the number of parent isotopes existing at the time of the rock/mineral crystallization:

$$n_p = n_{p0} e^{-\lambda_p t} \quad (4)$$

where n_{p0} = number of parent isotopes at the time of crystallization. After a time period t the number of radiogenic daughter isotopes is given by:

$$n_{d*} = n_p (e^{\lambda_p t} - 1) \quad (5)$$

where: n_{d*} = number of radiogenic daughter isotopes. Since most rocks/minerals also contain non-radiogenic isotopes that were trapped in the crystal structure during crystallization or added during later alteration, and hence not created during the radioactive decay, the equation becomes:

$$n_d = n_{d0} + n_p (e^{\lambda_p t} - 1) \quad (6)$$

where: n_d = total number of isotopes (both radiogenic and non-radiogenic) and n_{d0} = number of non-radiogenic isotopes. The three decay chains for ^{238}U , ^{235}U and ^{232}Th can now be treated as simple equations in the same fashion as the equation above:

$$^{206}\text{Pb} = ^{206}\text{Pb}_0 + ^{238}\text{U} (e^{\lambda_{238} t} - 1) \quad (7)$$

$$^{207}\text{Pb} = ^{207}\text{Pb}_0 + ^{235}\text{U} (e^{\lambda_{235} t} - 1) \quad (8)$$

$$^{208}\text{Pb} = ^{208}\text{Pb}_0 + ^{232}\text{U} (e^{\lambda_{232} t} - 1) \quad (9)$$

Since it is much easier to measure isotopic ratios instead of absolute abundances in mass spectrometers, it is common practice to rearrange the equations above by dividing with a stable, non-radiogenic isotope of the daughter element:

$$\frac{^{206}\text{Pb}}{^{204}\text{Pb}} = \frac{^{206}\text{Pb}_0}{^{204}\text{Pb}} + \frac{^{238}\text{U}}{^{204}\text{Pb}} (e^{\lambda_{238} t} - 1) \quad (10)$$

$$\frac{{}^{207}\text{Pb}}{{}^{204}\text{Pb}} = \frac{{}^{207}\text{Pb}_0}{{}^{204}\text{Pb}_0} + \frac{{}^{235}\text{U}}{{}^{204}\text{Pb}} (e^{\lambda_{235}t} - 1) \quad (11)$$

$$\frac{{}^{208}\text{Pb}}{{}^{204}\text{Pb}} = \frac{{}^{208}\text{Pb}_0}{{}^{204}\text{Pb}_0} + \frac{{}^{232}\text{Th}}{{}^{204}\text{Pb}} (e^{\lambda_{232}t} - 1) \quad (12)$$

Pb_0 is also normally referred to as *common lead*. If the contribution of common lead is very low or even negligible compared to radiogenic lead, the three equations above can be simplified to:

$$\frac{{}^{206}\text{Pb}^*}{{}^{238}\text{U}} = (e^{\lambda_{238}t} - 1) \quad (13)$$

$$\frac{{}^{207}\text{Pb}^*}{{}^{235}\text{U}} = (e^{\lambda_{235}t} - 1) \quad (14)$$

$$\frac{{}^{208}\text{Pb}^*}{{}^{232}\text{U}} = (e^{\lambda_{232}t} - 1) \quad (15)$$

where * is *radiogenic*. A benefit with the two decay chains in the U-Pb system is the possibility to create a fourth isochron equation by dividing equation 11 and 10:

$$\frac{\left(\frac{{}^{207}\text{Pb}}{{}^{204}\text{Pb}}\right) - \left(\frac{{}^{207}\text{Pb}_0}{{}^{204}\text{Pb}_0}\right)}{\left(\frac{{}^{206}\text{Pb}}{{}^{204}\text{Pb}}\right) - \left(\frac{{}^{206}\text{Pb}_0}{{}^{204}\text{Pb}_0}\right)} = \left(\frac{{}^{235}\text{U}}{{}^{238}\text{U}}\right) \frac{(e^{\lambda_{235}t} - 1)}{(e^{\lambda_{238}t} - 1)} = \left(\frac{{}^{207}\text{Pb}^*}{{}^{206}\text{Pb}^*}\right)^* \quad (16)$$

where * in this case is the ratio of radiogenic ${}^{207}\text{Pb}/{}^{206}\text{Pb}$. In most cases, the system has not been closed and secular equilibrium has not been achieved. This leads to the problem that the equations above are not valid. In order to overcome this problem, numerous numerical and graphical methods have been developed, which in turn has led to a great variety of visualization techniques, see section *Visualization of U-Th-Pb Data* below for further details.

3.3.1.3 Visualization of U-Th-Pb data

Equations (10, 11 and 12) are used to generate traditional isochron plots (Fig. 8). Isochrons were first used by Holmes (1946) and Houtermans (1946). Early on it was evident that the dual decay chains created when the two different uranium isotopes (${}^{238}\text{U}$ and ${}^{235}\text{U}$) decay could be of great use in geochronology, and Wetherill (1956) introduced the concordia diagram. In this diagram, Wetherill plotted ${}^{206}\text{Pb}^*/{}^{238}\text{U}$ against ${}^{207}\text{Pb}^*/{}^{235}\text{U}$ for the same analyses. The concordia plot is created by using the set of solutions to the equations 13 and 14 for the same values for t . This plot is non-linear since ${}^{238}\text{U}$ and ${}^{235}\text{U}$ have different half-lives, and therefore points on the concordia curve are where ${}^{206}\text{Pb}^*/{}^{238}\text{U}$ and ${}^{207}\text{Pb}^*/{}^{235}\text{U}$ have the same age. Every sample where the system has remained closed will plot

on the concordia curve (being concordant). Samples that have gone through disturbances in the system will plot outside the concordia curve (being discordant), unless they are completely reset and back on the concordia (Schoene 2014).

In the following section it is (for simplicity) assumed that all analyzes are corrected for common lead. However, this is not often the real case. Discordant data can be due to: loss or gain of lead and/or uranium or because of mixing of material with different ages. It is thought that lead loss and/or mixing with younger or less radiogenic material are the most important processes that cause discordant data (Schoene 2014).

Initially, a mineral crystallizes and Pb^* is incorporated into the crystal structure of the mineral. Subsequently, the ${}^{207}\text{Pb}^*/{}^{235}\text{U}$ and ${}^{206}\text{Pb}^*/{}^{238}\text{U}$ ratios evolve, following the concordia curve (Fig. 9). If the system undergoes a lead-loss event, the lead that leaves the mineral would be of a ${}^{207}\text{Pb}/{}^{206}\text{Pb}$ composition that matches its Pb-Pb date (Eq. 16). If instead several minerals went through the same process, but with different degrees of lead loss, they would plot on a straight discordia line that passes through the origin and intersects the concordia curve at a point that is equal to the real age (Fig. 10). In this case the Pb-Pb date also equals the age of the upper intercept of the discordia line (if the lead loss is recent, i.e. $t=0$). If the minerals once again would act as closed systems, they would continue to accumulate radiogenic lead (Pb^*) through radioactive decay and progress along a track in such a way that the discordia array still is a straight line. If the minerals were to be dated 100 My later, the upper intercept of the concordia curve would equal the initial

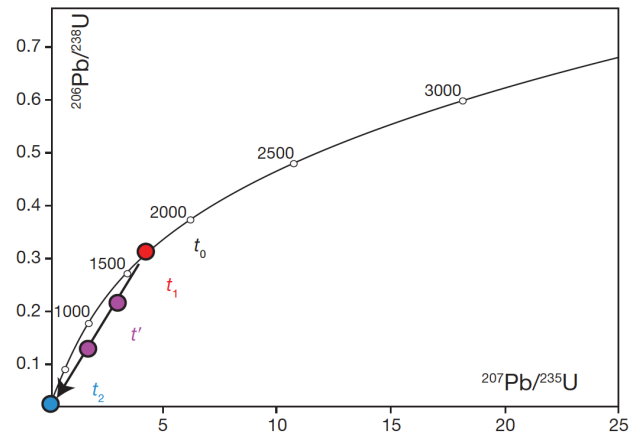


Fig. 9. Example of a concordia curve where a 1.7 Ga zircon either goes through lead-loss or analysis is a mixture of an igneous core and a metamorphic overgrowth. t_0 is the crystallization age = 1.7 Ga. After 1.7 Gy of radioactive decay during closed system behavior the zircon plots at t_1 on the concordia curve (red circle). At t_2 the zircon undergoes open system behavior through either lead-loss or growth of a metamorphic rim around the old core (blue circle). t' symbolizes zircons that plot discordant due to partial lead-loss of mineral overgrowth at t_2 (purple circles). Modified from Schoene (2014).

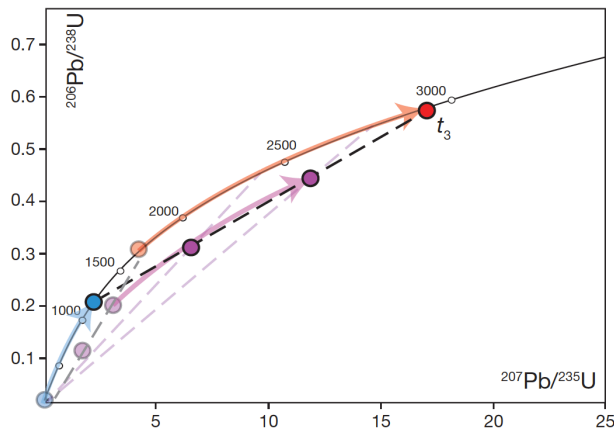


Fig. 10. Continuation of the example in Fig. 8. The mineral once again behaves as a closed system and progresses along the concordia curve for 1.2 Gy until it reaches t_3 . The purple circles are analyses of discordant data that define a discordia line where the upper intercept with the concordia symbolizes age of original crystallization (t_0 in Fig. 8) and the lower intercept represents the age of the lead-loss or overgrowth event (t_2 in Fig. 8). Modified from Schoene (2014).

crystallization age of the mineral whereas the lower intercept equals to the time when the lead-loss event occurred. In a situation like this, neither the U-Pb nor the Pb-Pb dates of single minerals would give a correct age. However, since the upper intercept of the discordia line represents initial crystallization and the lower intercept the Pb-loss event, a graphical solution (Fig. 10) yields some information about the geological history of the minerals (Schoene 2014).

The exact same effect as in the example above would be noted if the mineral, say a zircon, was zoned with an older igneous core and a younger metamorphic overgrowth and the analysis was a mixture of the two (Fig. 10). This scenario is quite simple, with only one event of lead-loss or overgrowth; in reality this is rarely the case, which may make the interpretation of geochronological data somewhat difficult.

Other varieties of concordia diagrams exist, using different ratios on the x- or y-axis. One example is the Th/Pb vs. U/Pb, sometimes utilized for monazite whose $^{206}\text{Pb}/^{238}\text{U}$ system is affected by ^{230}Th disequilibrium coming from high Th/U ratios (Searle et al. 2007; Villeneuve et al. 2000). Even though many alternatives exist, the most commonly used alternative for the Wetherill concordia diagram is the Tera-Wasserburg (T-W) concordia diagram where $^{238}\text{U}/^{206}\text{Pb}$ is plotted on the x-axis and $^{207}\text{Pb}/^{206}\text{Pb}$ is plotted on the y-axis (Tera & Wasserburg, 1972a,b). If corrected for common lead (as in the Wetherill diagram) the ratios become $^{238}\text{U}/^{206}\text{Pb}^*$ and $^{207}\text{Pb}^*/^{206}\text{Pb}^*$. When data is plotted using these isotope ratios, concordant and discordant data can be visualized and interpreted in the same fashion as in the Wetherill diagram. In addition to this, the T-W diagram also tests for open system behavior and thus combines the powers of the concordia diagram with those of the isochron

diagram. If, for an example, a cogenetic series of samples, that has not been corrected for common Pb, plot off the concordia only because of variable contamination from a single initial lead composition, then a straight line drawn through the series or samples will intercept the concordia at the true age and the y-axis ($^{207}\text{Pb}/^{206}\text{Pb}$) where it equals Pb_0 (Fig. 10; Schoene 2014).

However, if a sample is affected by lead-loss, or not only one single but also mixing of several age domains, the power of the linear regression (straight line) technique fails. This would be the case if the discordant samples are not falling onto a straight line, or if multiple age domains can be recognized within the mineral. Another, more statistical way of testing if this is the case is by utilizing a 3D isochron (Ludwig, 1998; Wendt, 1984). In a 3D isochron it is possible to simultaneously plot the initial $^{206}\text{Pb}/^{204}\text{Pb}$ and $^{207}\text{Pb}/^{204}\text{Pb}$ ratios together with age, for samples that are cogenetic (Fig. 11). In this method, $^{238}\text{U}/^{206}\text{Pb}$ is plotted on the x-axis, $^{207}\text{Pb}/^{206}\text{Pb}$ on the y-axis and $^{204}\text{Pb}/^{206}\text{Pb}$ on the z-axis; together the three different ratios make up a 3D coordinate system. A series of cogenetic samples should fall on a straight line in this coordinate system if the only difference between them is different amounts of Pb_c . The 3D isochron method is thus suitable for not only applications in high-precision dating but also in giving information about whether lead loss or inheritance is of importance in a dataset with high Pb_c (Ludwig, 1998).

Discordant samples will plot slightly different in

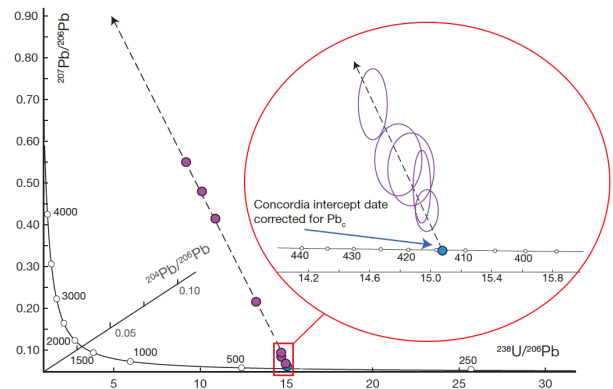


Fig. 11. Tera-Wasserburg (T-W) concordia diagram for both 2D and 3D visualization. The red frame outlines the magnified inset in the central-right part of the figure. Concordant and discordant data can be visualized and interpreted in the same fashion as in a Wetherill concordia diagram but the T-W plot also tests for open system behavior. A linear regression through the samples will intersect the concordia at a point equal to the real age. If samples plot discordant only because of mixing with initial common-lead then the linear regression will intersect the y-axis ($^{207}\text{Pb}/^{206}\text{Pb}$) higher up than if mixed with radiogenic lead (which could come from an older age domain of the mineral). By introducing a z-axis ($^{204}\text{Pb}/^{206}\text{Pb}$), it is possible to deduce if the samples have gone through lead-loss or some kind of inheritance. Modified from Schoene (2014).

the T-W diagram compared to the Wetherill concordia diagram. This is simply due to the different isotopic ratios utilized in the two types of diagrams. Fig. 12 shows some of the most common causes to discordant data. Recent Pb-loss (Fig. 12a) is commonly explained by Pb-loss occurring in metamict (radiation damaged) zircons, which is seen as horizontal displacement to the right of the concordia in a T-W diagram. Horizontal displacement may also be caused by incorrect U/Pb calibration but in such a case, the horizontal displacement may be either to the left or right of the concordia. Note that the $^{207}\text{Pb}/^{206}\text{Pb}$ age is unaffected by recent Pb-loss, or is representative of a minimum age (Faure & Mensing 2005).

Episodic Pb-loss (Fig. 12b) is normally caused by a metamorphic event or similar process in the past that triggered partial Pb-loss. In the case of an incomplete process, the partial Pb-loss will be displayed as a point in between the “real” age and the Pb-loss event. The two situations above (recent Pb-loss and episodic Pb-loss) stress the importance of having large enough datasets since it is impossible to distinguish between the two if only having one data point (Faure & Mensing, 2005).

Common Pb interference has already been dis-

cussed in the section above (Fig. 11) and is showed here only to put it in a graphical context among the other plots (Fig. 12c). The data point will have high $^{207}\text{Pb}/^{206}\text{Pb}$ values, usually around 1. In a T-W diagram, this displaces the point along a steep trajectory up to high $^{207}\text{Pb}/^{206}\text{Pb}$ ages. The zircons in a population will plot along a discordia line (Fig. 12d) if they lose lead to various degree during one episodic Pb-loss event (Faure & Mensing, 2005).

3.4 Laser ablation inductively coupled plasma mass spectrometry (LA-ICP-MS)

The epoxy mounts were placed in an ANU HelEx II sample cell in a Teledyne Photon Machines Analyte G2 laser ablation system. The laser system is connected to a quadrupole Bruker Aurora M90 ICP-MS (Appendix II and III for further methodology descriptions). In laser ablation inductively coupled plasma mass spectrometry (LA-ICP-MS), the mineral is ablated with a laser beam and the ablated particles are transported with a carrier gas into a mass spectrometer for further analysis. The technique started to be applied for U-Pb geochronology in the early 1990s (e.g. Feng et al. 1993; Fryer et al. 1993; Hirata & Nesbitt 1995). It has since become one of the most used meth-

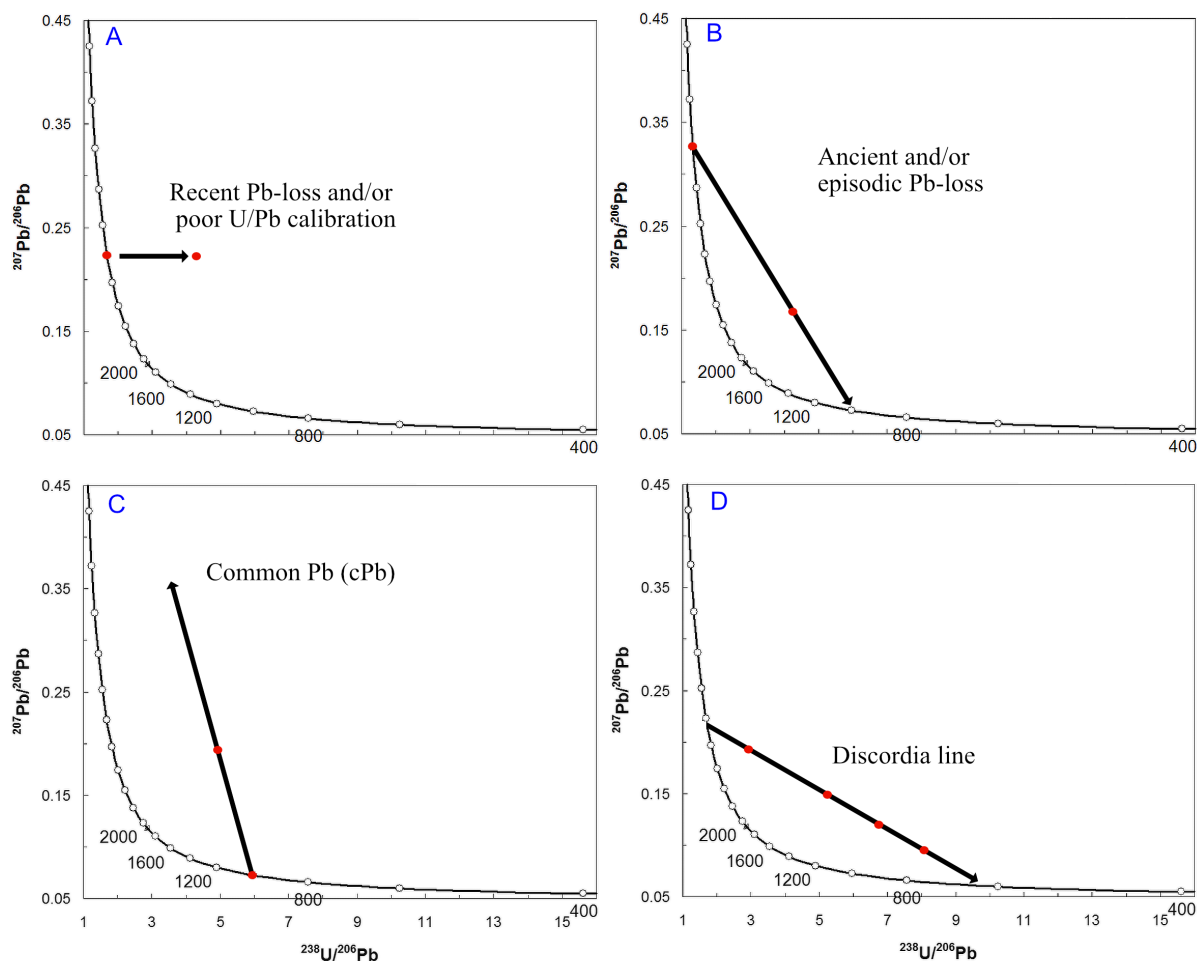


Fig. 12. Four common reasons to why data plot discordant. A) Recent Pb-loss and/or a poor U/Pb calibration. B) Ancient and/or episodic Pb-loss. C) Common Pb (Pbc). D) Discordant data falling on a single discordia line.

ods for U-Pb measurements, largely because of the reasonably high spatial resolution, fast analysis time and its comparatively low operation costs.

A LA-ICP-MS system is divided into two parts: (1) the actual laser ablation unit and its sample holder and (2) the mass spectrometer with its plasma. The lasers in laser ablation systems are usually of either solid-state type (e.g. Nd-YAG) or gas-source type (e.g. Ar-F excimer) and the wavelengths tend to be short (266 nm or less). Several authors, such as Guillong et al. (2003) have showed that lasers with short wavelength together with precisely controlled energy densities and pulse rates (normally on the nanosecond scale) are most efficient when it comes to ablation. Other benefits of this type of lasers are minimization of heat and reduced elemental and isotope fractionation.

The sample is placed in a sample holder with a window that is laser transparent and particles that are ablated by the laser are transported with a carrier gas into the plasma torch. A wide range of gases has been tested, with variable instrument sensitivity (e.g. Guillong et al. 2003) and today most research facilities use He gas, sometimes with N₂, Ar or H blended into the gas mixture (Schoene 2014). Cottle et al (2009a) and Frei & Gerdes (2009) showed that the speed and stability with which the ablated particles were transported to the plasma is dependent not only on the carrier gas but also on the size and shape of the sample cell. This affects not only the measurement itself but also sample throughput and affordability.

Inside the plasma, argon gas flows in circular channels. Once a spark ignites the argon gas, electrons are stripped off from the argon atoms, creating argon ions. Wound around the torch is a radio frequency load coil and when a power is applied to this, oscillating magnetic and electric fields are created that catch the argon ions. Ions caught in the oscillating fields will start to collide with new argon atoms, establishing an argon discharge, also known as an argon plasma. The particles from the sample are upon arrival into the plasma first converted into gaseous atoms and then ionized, all of this due to the high temperature (c. 6000-10000°C), depending on ICP-MS system. When it comes to the ICP-MS, many different types are utilized in laser ablation U-Th-Pb geochronology: single-/multicollector or quadrupole magnetic sector instruments (USGS, 2015).

3.5 Immobile element monitor for a single precursor system and isocon analysis

The idea of using immobile elements as chemical alteration pattern monitors was first described by Gresens (1967) and it has since been examined and refined by numerous workers (e.g. Babcock 1973; Finlow-Bates & Stumpfl 1981; MacLean & Kranidiotis 1987; MacLean 1988, 1990; MacLean & Barrett 1993). Overall, these authors have examined and later outlined how elements that have remained immobile during hydrothermal alteration and metamorphism can

be used when assessing gain and/or loss of chemical components during alteration. Previous studies and especially those of MacLean & Kranidiotis (1987) and MacLean & Barret (1993) are now widely used when defining alteration trends from single precursor systems in e.g. volcanic massive sulfide deposits in greenstone belts.

MacLean & Kranidiotis (1987) & MacLean & Barret (1993) argued that alteration of one originally chemically homogenous rock into a secondary, altered rock, produces a “single precursor system”. If immobile elements are plotted in binary (X-Y) plots, the samples will regress linearly through or very close to the origin. Depending on whether alteration led to a mass gain or a mass loss, the samples will plot correspondingly either closer or further away from the origin (Finlow-Bates & Stumpfl 1981). The immobile incompatible elements will thus preserve a constant inter-element ratio. Immobile incompatible element pairs used in these binary plots will define highly correlated linear regressions with correlation coefficients (r) values of $r = 0.90-0.99$.

Isocon analysis (Grant 1986, 2005) is a commonly used method for quantitatively estimating concentrations in mass transfer or changes in mass or volume during chemical alteration. The method is based on the assumption that there is a common unaltered original (precursor) rock composition, which has been subject to mass gain or mass loss of mobile elements during alteration. By comparing the unaltered part of the rock with the altered parts, the chemical changes can be assessed. The method requires limited data manipulation and is performed by plotting the altered composition (or an average of several altered compositions) against the unaltered/least-altered composition. However, it should be noted that great care has to be taken when choosing the unaltered/least-altered composition. This is not always straightforward and a number of influencing parameters, such as: field relations, geochemistry, textural and structural properties have to be considered.

When creating isocon diagrams, immobile elements are used to define an isocon line. For this study, elements with most immobile behavior were found in two ways: (1) by plotting traditionally viewed immobile elements (such as Al, Ti, Zr, Hf, Nb, and Lu) against each other in binary element plots and then calculating linear regressions or (2) by dividing the component of the average altered composition (CiA) with the component of the least altered composition (CiO), e.g. SiO₂ average/SiO₂ unaltered and so on. When examining slope to data point (CiA/ CiO) values, those equal to or close to 1 indicate immobility. In this study the slope of the isocon line was determined by a linear regression through the origin and the most immobile elements, all yielding CiA/ CiO values close to 1 and thus indicating element immobility. There are however, not only one but five different ways in which the slope of the isocon can be determined. The advantage of using CiA/ CiO values is that it allows for

arbitrarily scaling when creating the actual diagram since the scaling factors are mathematically cancelled (Grant 2005). If employing one of the other methods, great care has to be taken when scaling. Grant (1986) developed an equation for the relationship between the isocon slope and the overall relative mass gain or mass loss. The equation can be expressed by:

$$\Delta M = \left(\frac{1}{m} - 1 \right) * 100 \quad (17)$$

where ΔM is the mass change and m is the slope of the isocon.

4 Samples and petrography

4.1 Sample collection

Sample localities are shown in table 6. Stephens et al. (2009) classifies the felsic metavolcanic rock as belonging to a suite of rocks called “Svecofennian volcanic and subvolcanic intrusive rocks with assumed ages of c. 1.91-1.89 Ga”, that are widespread within the Bergslagen region. The granite is classified as belonging to the “late Svecokarelian granite-pegmatite

(GP) intrusive rock suite (1.85-1.75 Ga) (Stephens et al. 2009).

4.2 Sample descriptions

Samples that are considered as felsic metavolcanic rocks are most likely metamorphic equivalents of originally hydrothermally altered volcanic rocks. Origin is sometimes hard to deduce.

KES150001

Medium- to coarse-grained, rich in quartz and mica (Fig. 13). Chemically altered beyond recognition but may originally have been a felsic metavolcanic rock; this sample will from now on be denoted as such. The rock consists largely of quartz, biotite and muscovite together with sericite, alkali feldspar and accessory zircon and apatite. Quartz grains are anhedral to subhedral in shape of variable size and with a few, randomly oriented fractures. Some quartz grains show inclusions of fine-grained quartz and biotite. In general, biotite grains are subhedral to euhedral and slightly platy. Muscovite grains are subhedral to euhedral and platy, some show twinning and crystals close to extinction are mottled in a characteristic mica fashion.

Table 6. Sample locations. Coordinates are given in WGS-84 dec.

Sample-ID	North	East	Locality	Rock type	Field assessments
KES150001	59.765770°	15.490143°	Roadcut S of Forshammar	Possible metavolcanic ¹	High degree of alteration
KES150002	59.815899°	15.529216°	Small outcrop, N of Riddarhyttan, towards Källfallet	Metavolcanic	Intermediate degree of alteration
KES150003	59.832509°	15.549156°	Old Cu process plant, W of Bäckegruvan	Metavolcanic	Intermediate-high degree of alteration
KES150004	59.835605°	15.588524°	Roadcut W of Bjursjön	Metavolcanic	Low degree of alteration
KES150005	59.846062°	15.588492°	Nya Bastnäs, close to the mines	Metavolcanic	Intermediate-high degree of alteration
KES150006	59.852334°	15.592519°	Bastnäs Storgruvefält, NW part	Metavolcanic	High degree of alteration
KES150007	59.865135°	15.611249°	Högfors Storgruva	BIF	-
KES150008	59.865135°	15.611249°	Högfors Storgruva	Granite	Cuts the iron oxide mineralization
WL150001	59.858883	15.590674	Roadcut between Riddarhyttan and Fagersta	Metavolcanic	
WL150002	60.078996	15.929440	Mine dump close to the old Östanmossa open pit mine	Metavolcanic	
EJ.ÖGytt-1	59.515300°	14.958545°	Mine dump close to the old Östra Gyt-torpsgruvan	Metavolcanic	

¹Altered beyond recognition.

KES150002

Fine-grained, weakly quartz-porphyritic, felsic metavolcanic rock with dispersed, very fine-grained biotite crystals (Fig. 13). Quartz is the main mineral together with minor plagioclase, biotite, muscovite, presumed alkali feldspar and accessory zircon and apatite. Quartz is generally anhedral to subhedral and fine-grained but larger crystals occur. Plagioclase grains are anhedral to subhedral and commonly show albite twinning. Biotite likely occurs in two generations; one as anhedral to subhedral, interconnected grains with altered edges that define a weak foliation in thin section and a second with more euhedral and platy grains.

KES150003

Fine-grained, quartz-porphyritic, felsic metavolcanic rock with biotite defining a foliation that gradually changes from spaced to continuous (Fig. 14). Quartz and biotite are the major phases together with minor muscovite, possibly chlorite, plagioclase, presumed alkali feldspar with microperthite as well as accessory zircon and apatite. Quartz occurs as anhedral to subhedral, both fine-grained and more coarse-grained bands. Biotite grains are ranging from anhedral to euhedral in shape and are generally platy, defining a foliation. Some biotite grains have altered edges. Muscovite is spatially associated with biotite and occurs as subhedral to euhedral, platy grains. Plagioclase crystals are fine-grained, anhedral to subhedral with albite twinning. Alkali feldspar grains are anhedral to subhedral with most likely strain-induced microperthite.

KES150004

Very fine-grained, felsic metavolcanic rock with isolated mica crystals (Fig. 14). The rock consists largely of quartz with minor phases of biotite, plagioclase, alkali feldspar with microperthite and siderite and/or limonite and hematite. Quartz grains are anhedral to subhedral and very fine grained. Biotite occurs as an- to euhedral, elongated grains with slightly altered edges that define a weak foliation that is only discernible in thin section. Plagioclase grains are anhedral to subhedral, some with either albite twinning while others are more similar to quartz in appearance with low interference colors but with inclined extinction. Siderite and/or limonite are found in fine-grained earth-like aggregates with very high interference colors spatially associated around or close to hematite. Hematite occurs as anhedral to subhedral disseminated crystals.

KES150005

This rock is a fine-grained, foliated felsic metavolcanic rock (Fig. 15). Quartz, muscovite and biotite are the major phases together with minor siderite and/or limonite and an unknown phase that consists of heavily altered porphyroclasts, possibly andalusite or cordierite. Alkali feldspar with microperthite as well as chlorite are found as accessory grains. Hematite occurs as bands. Quartz is generally an- to subhedral and occurs

in two types of bands, one with larger grain size with little or no micas and one with smaller grain size and an abundance of micas. Grains in both types are platy. Biotite and muscovite are subhedral to euhedral and spatially associated with each other. Some muscovites show twinning and crystals close to extinction are mottled in a characteristic mica fashion. In places the micas define a weak crenulation cleavage. Siderite and/or limonite are found in fine-grained earthy aggregates with very high interference colors spatially associated around or close to hematite. Alkali feldspar with microperthite are anhedral to subhedral, few and small.

KES150006

Aphanitic, foliated felsic metavolcanic rock with numerous, heavily altered porphyroclasts of possibly andalusite or cordierite (Fig. 15). The rock consists largely of quartz with minor biotite and muscovite and the altered porphyroclasts. Quartz is an- to subhedral, inequigranular and interlobate. Biotite and muscovite are spatially associated and occur as sub- to euhedral, elongated grains. Some muscovite crystals are twinned. The altered porphyroclasts consist of small, anhedral and interconnected grains with moderate relief and a dusty appearance in plane polarized light together with high interference colors.

KES150007

A somewhat skarn-banded iron formation (BIF; Fig. 16). The rock consists of quartz, amphibole (possibly tremolite) biotite and hematite. Quartz is anhedral to subhedral and generally fine-grained but a few larger porphyroblasts can be found grouped together. Amphibole (possibly tremolite) occurs as larger, anhedral to subhedral crystals that are nonpleochroic, colorless to faintly green in plane polarized light and have second order interference colors. Hematite is found in massive bands, usually with a bluish tint added to its medium grey-white reflected-light color. Some silicate minerals occur dispersed within the massive hematite bands. The rock is slightly magnetic in hand sample but no magnetite was found in thin section.

KES150008

Medium- to coarse-grained, mostly isotropic red granite (Fig. 16). Quartz, plagioclase, amphibole (possibly actinolite), muscovite and alkali feldspar with microperthite are the major phases together with minor biotite and fracture fillings of chlorite and accessory rutile and hematite. Overall, the minerals have a "dusty" appearance as if affected by alteration. Quartz is an- to subhedral. Alkali feldspars are inequigranular with cross-hatched twinning. Amphibole (possibly actinolite) is sub- to euhedral and occurs spatially associated with platy muscovite and chlorite in fractures. Rutile is fine-grained and anhedral with extremely high birefringence. Hematite is disseminated with an- to subhedral crystals.

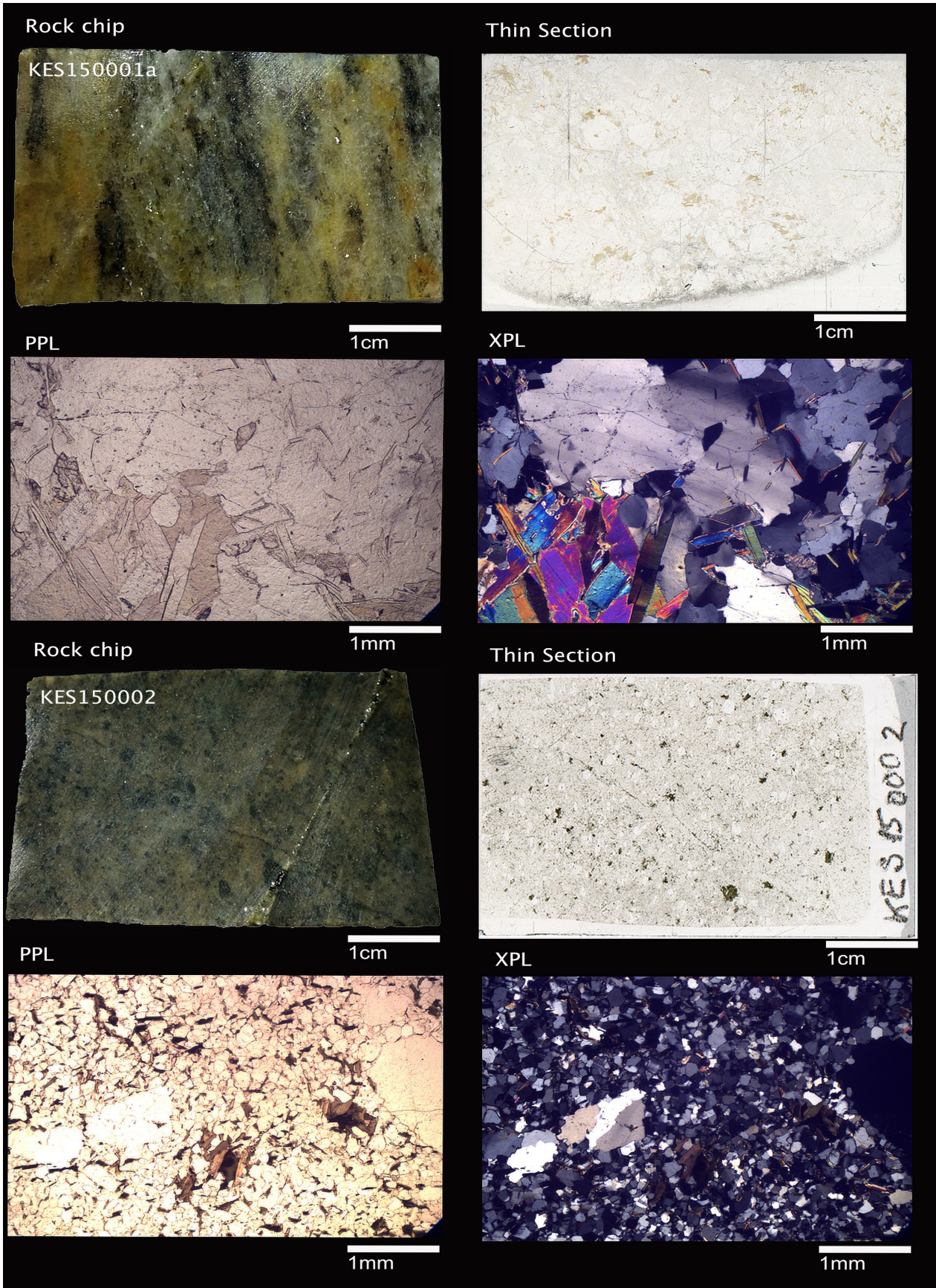


Fig. 13. Representative photomicrographs of samples KES150001 and KES150002. KES150001: coarse- and fine-grained quartz together with muscovite and biotite. KES150002: fine-grained quartz and biotite matrix together with larger quartz crystals. Thin sections are standard-sized. Pictures taken with plane polarized and cross polarized light uses x5 magnification.

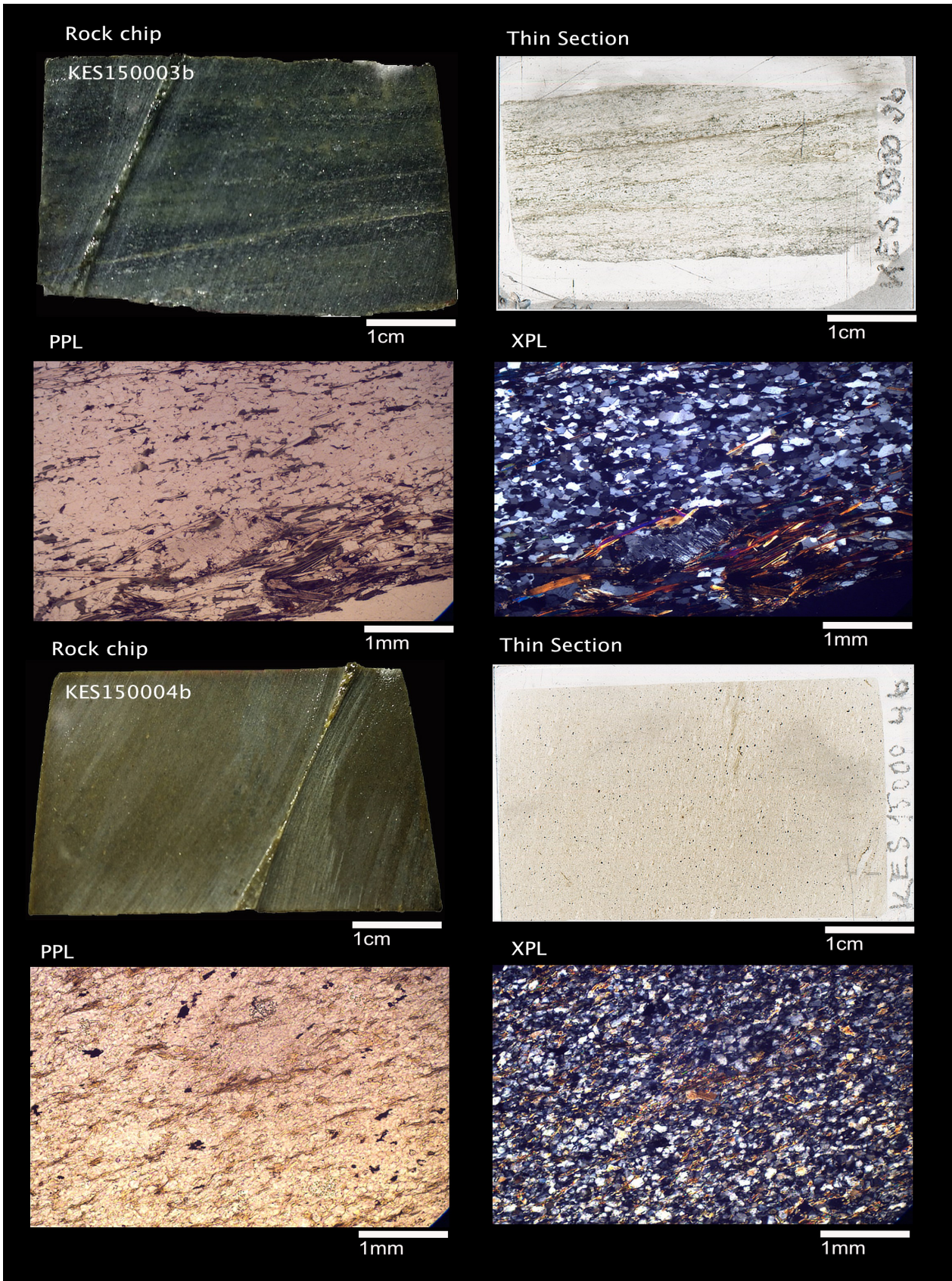


Fig. 14. Representative photomicrographs of samples KES150003 and KES150004. KES150003: fine-grained matrix of quartz, biotite and muscovite with larger crystals of quartz and feldspars with micropertthite. Micas define the foliation. KES150004: very fine-grained matrix of quartz, biotite, muscovite and plagioclase together with opaque crystals of hematite, siderite and/or limonite. Thin sections are standard-sized. Pictures taken with plane polarized and cross polarized light uses x5 magnification.

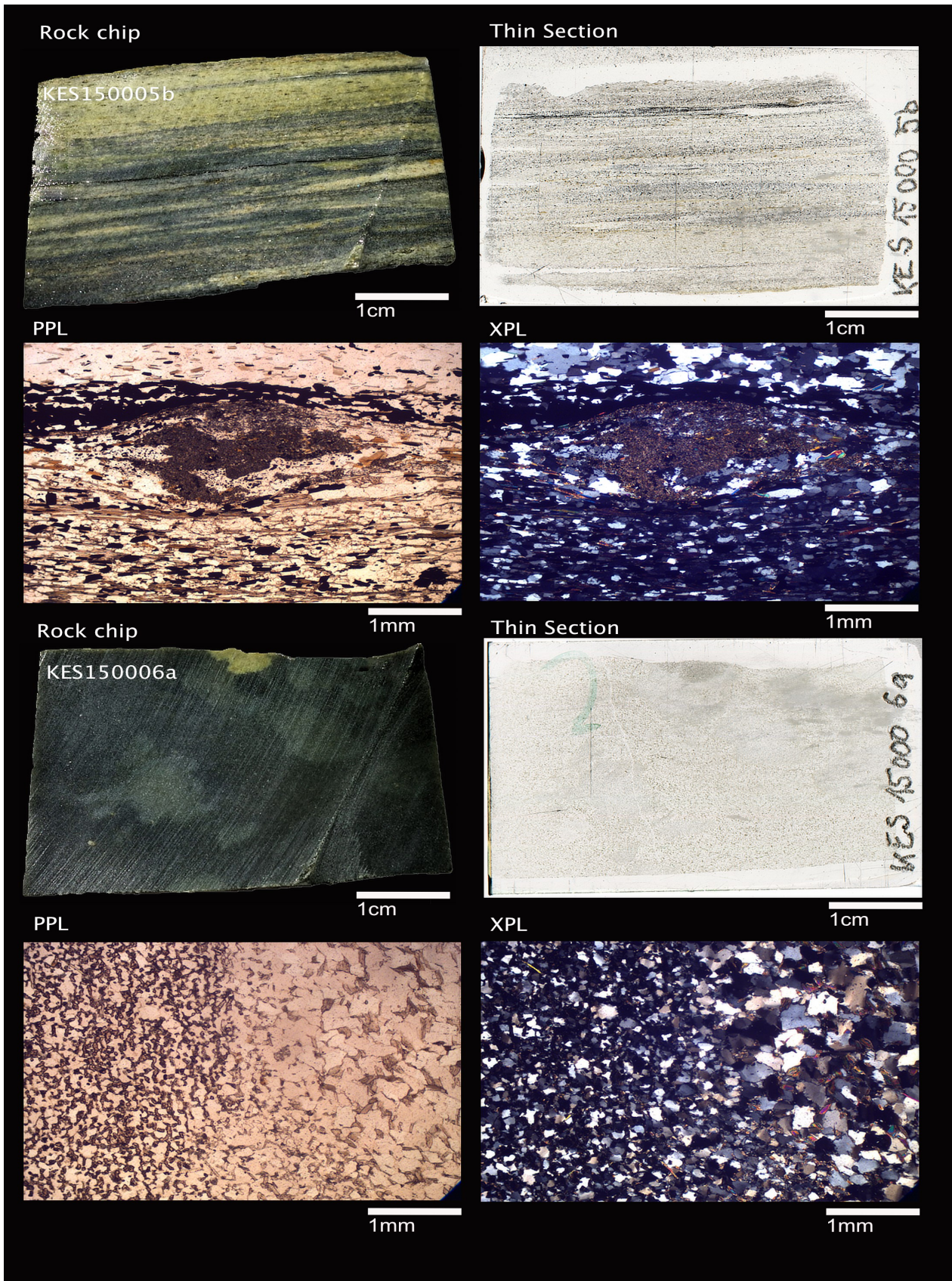


Fig. 15. Representative photomicrographs of samples KES150005 and KES150006. KES150005: fine-grained matrix of quartz, biotite and muscovite together with larger, heavily altered, crystals of possibly andalusite or cordierite and opaque crystals of hematite, siderite and/or limonite. Micas define the foliation. KES150006: aphanitic matrix of quartz, biotite and muscovite together with larger, heavily altered, crystals of possibly andalusite or cordierite. Thin sections are standard-sized. Pictures taken with plane polarized and cross polarized light uses x5 magnification.

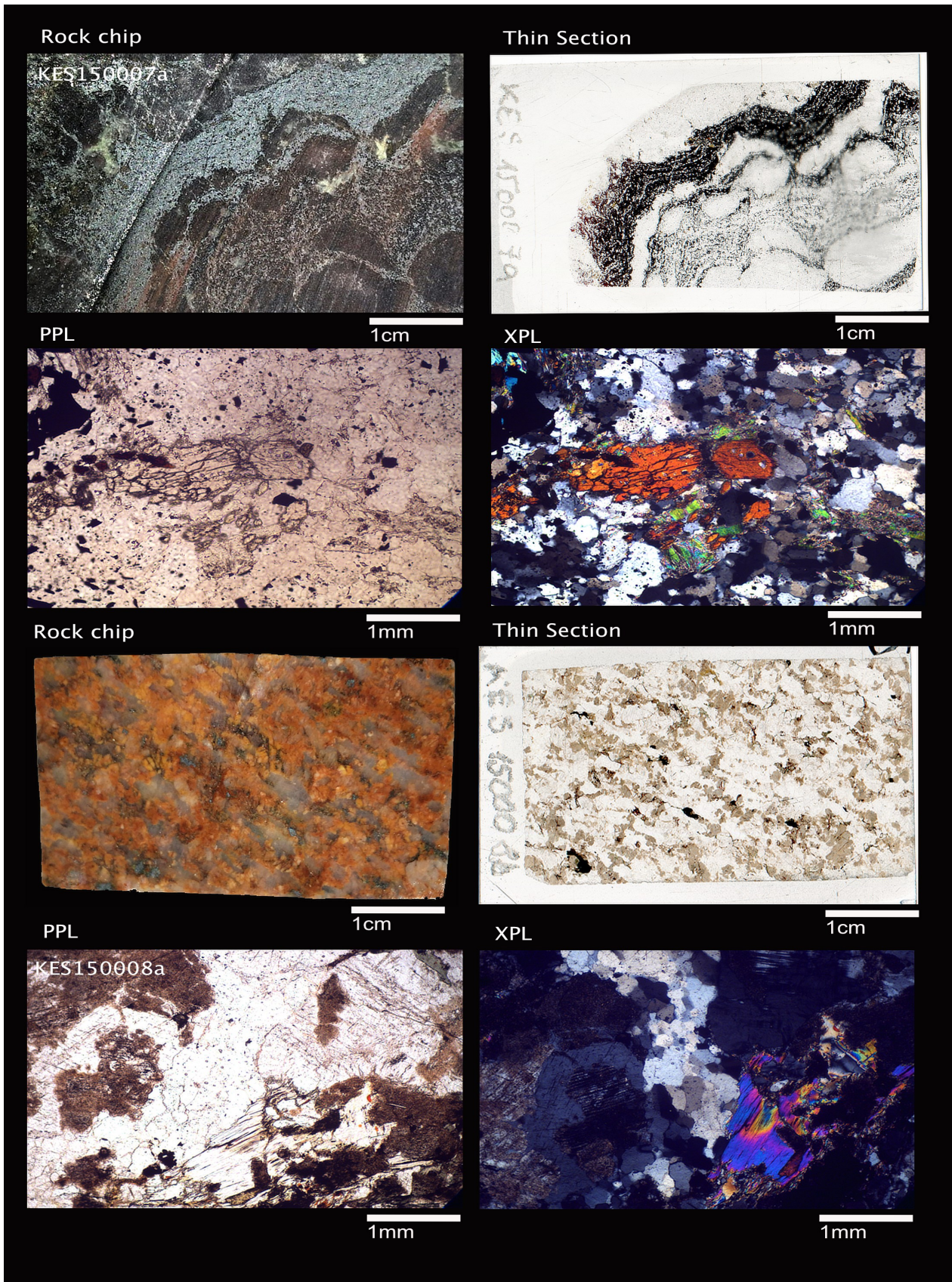


Fig. 16. Representative photomicrographs of samples KES150007 and KES150008. KES150007: quartz, amphibole (possibly tremolite), biotite and opaque crystals of hematite. A large amphibole crystal is seen in the center of the PPL/XPL pictures. KES150008: “dusty” crystals of quartz, amphibole (possibly actinolite), muscovite, chlorite and opaque crystals of hematite. Pictures taken with plane polarized and cross polarized light uses x10 magnification for KES150007 and x5 for KES150008.

WL15001

Time constraints prevented further examination of this sample. Studies of separated crystals in SEM indicated the presence of titanite and rutile.

WL15002

Time constraints prevented further examination of this sample.

EJ.ÖGytt-1

Time constraints prevented further examination of this sample. Studies of separated crystals in SEM indicated the presence of titanite and rutile.

5 Results

5.1 Whole rock (WR) analysis

5.1.1 Major elements

Three rock types were sampled on the basis of their field classification: (1) felsic metavolcanic rocks (KES150001-0006), (2) Banded Iron Formation (BIF) (KES150007) and (3) granite (KES150008). Their major, minor and trace element analyses are, as mentioned earlier, listed in Appendix I. Whole-rock analytical data are calculated and normalized on a volatile-free basis and plotted using the IgPet software (www.rockware.com, 2016). CIPW normative mineralogy was calculated using IgPet and where $\text{Fe}_2\text{O}_3/\text{FeO}$ was adjusted according to Irvine & Baragar (1971) such that $\% \text{Fe}_2\text{O}_3 = \% \text{TiO}_2 + 1.5$. If the measured $\% \text{Fe}_2\text{O}_3 > \% \text{TiO}_2 + 1.5$, the excess Fe_2O_3 is converted to FeO. Due to the extreme chemical composition of the BIF, it has been omitted in many of the chemical discrimination diagrams.

Major elements are plotted against SiO_2 and Al_2O_3 , TiO_2 and K_2O are inversely correlated with SiO_2 (Fig. 17). Al_2O_3 ranges from 7.39 to 16.87, which is generally more than the alkali elements and CaO. CaO ranges from <0.01 to 0.33, which is rather low. MgO ranges from 0.71 to 4.40 and FeO ranges from 0.86 to 12.67. FeO is almost constant for any given MgO. TiO_2 ranges from 0.05 to 0.14. P_2O_5 is either 0.01 or less, which is below detection limit.

The majority of the felsic metavolcanic rocks plot within the rhyolite field, except for KES150004 that plots as a trachyte and KES150005 that plots within the dacite field (Fig. 18). This can be compared with a Zr/TiO₂ vs. Nb/Y diagram (Winchester & Floyd 1977) where all samples plot within the rhyolite field except KES150004 that plots within the rhyodacite/dacite field and KES150001 that is within the comendite/pantellerite field (due to its higher Nb/Y; Fig. 19). However, it should be noted that classification diagrams like those in Fig. 18 and 19, are primarily aimed at discriminating unaltered rocks. Since many of the felsic metavolcanic rocks are heavily altered, the diagrams should be used with a degree of caution.

Relative variations in Na_2O , K_2O and MgO can be highlighted in a triangular diagram (c.f. Hallberg 2003; Holtstam et al. 2014). Three samples have very low Na_2O contents and plot essentially along a MgO-K₂O join (Fig. 20). Two of the samples, KES150001 and KES150006 show high relative concentration of MgO and to a lesser extent K_2O , while KES150002 is strongly enriched in K_2O . Sample KES150004 plots close to the area belonging to “least altered volcanics” and the granitic sample plots close to “least altered granitoids”. KES150002 plots as “weakly altered rock” and KES150005 in between “weakly altered rocks” and “strong K-(Mg) alteration”.

In the igneous spectrum of Hughes (1972), KES150004 plots within the field of “unaltered volcanic rock” while all other samples plot as K-metasomatically altered (Fig. 21).

In the weathering index diagram of Ohta & Arai (2007), the felsic metavolcanic samples plot along the bottom axis with KES150004 closest to the unweathered, felsic corner (F) and KES150006 nearby the weathering corner (W) and the rest of the samples in between (Fig. 22). Some of the components included in the calculations for the weathering index diagram were below detection limit. In order for the calculations to work out, components below detection limit were set equal to the detection limit. These corrections affected one or several samples for the following components: TiO_2 , MnO, CaO, Na_2O , K_2O .

5.1.2 Trace elements

The BIF has been excluded from the trace element plots due to its extreme chemical nature. Rare Earth Elements (REE) concentrations for the six metavolcanic rocks (KES150001-0006) have (La/Yb)_{chond} values between 3.54- 14.09, the BIF (KES150007) has 250.26 (not shown) and the granite (KES150008) has 4.03. All samples have distinct negative Eu-anomalies with Eu/Eu* values between 0.20-0.45 for KES150001-0006, 0.33 for KES150007 and 0.21 for KES150008 (Fig. 23).

Trace element concentrations vary considerably, and in a primitive mantle-normalised plot several elements show pronounced negative anomalies: Ba, Nb, Ta, Sr, P and Ti, while Pb scatter with both positive and negative anomalies (Fig. 24).

5.1.3 Immobile element plots

Al, Ti, Nb, Zr, Hf and Lu are elements that are commonly immobile during alteration processes, and they were plotted against each other in binary element plots for all the felsic metavolcanic rocks. Plots with the best linear regression values (r values close to 1) were chosen (Fig. 25). The linear regression values (r) for these plots are shown in a matrix in table 6.

5.1.4 Relative concentration change during alteration

Calculations for isocon plots for the felsic metavolcanic rocks were done following Grant (1986, 2005) and

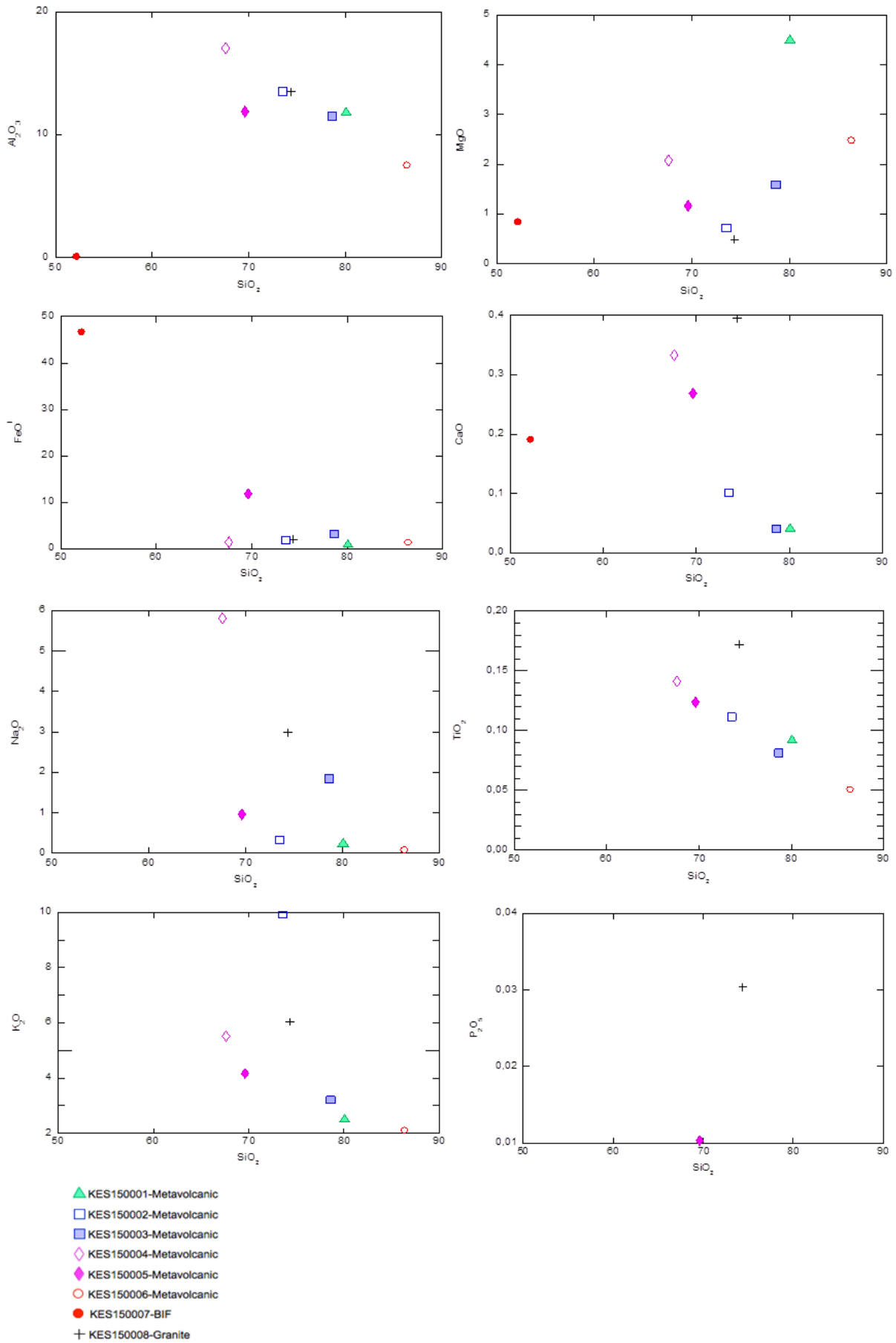


Fig. 17. Harker variation diagrams for the eight analyzed rocks KES150001-KES150008.

are presented in Appendix IV. KES150004 was assumed to best represent the unaltered/least altered volcanic precursor rock. This assumption is based on several factors: how KES150004 plots in Fig. 20, 21 and 22 and its apparent low degree of alteration as seen in outcrop, hand sample and thin section. The element pairs from section 5.1.3 with r-values closest to one (Al_2O_3 , Zr and Hf) were used as immobile reference elements in all the isocon plots and calculations. All samples have had mass gain.

KES150001 – (assumed) metavolcanic rock (roadcut south of Forshammar)
MgO and SiO₂ and Eu are the most strongly enriched compounds at (>+200%) and (>+60%) respectively

(Fig. 26). Cs and Sr are moderately enriched at c. (+40%), while Mo and Nd are weakly enriched at (<+20%). Ce and Pr plot on the isocon. Fe₂O₃, TiO₂, Ga, Nb, La and Sm are weakly depleted with (<-10%). Pb, K₂O, Ta, Gd, Tb are depleted with (-20%) to (-40%); Sn, U, Th, Y, Dy, Ho, Er, Tm, Yb, Lu, Ba and Rb are depleted (-40%) to (-60%), and Ni, Be, Na₂O, CaO and Zn are the most depleted at (>-60%). Overall, the slope of the isocon (0.67x) indicates a significant mass gain of c. 49% in the rock.

KES150002 – metavolcanic rock (outcrop north of Riddarhyttan, close to Källfallet)
Eu is most strongly enriched with (>+200%) (Fig. 27). Other enriched components are: K₂O and Co at

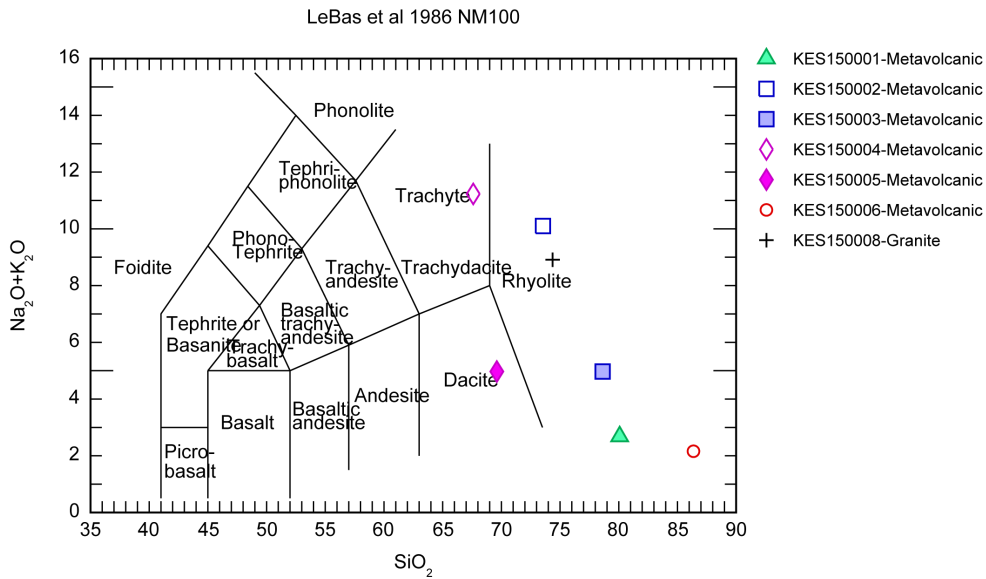


Fig. 18. TAS-diagram after LeBas et al (1986). The majority of the rocks plot as rhyolites together with one trachyte and one dacite sample. KES150007 is below detection limit for one or several of the components and hence omitted.

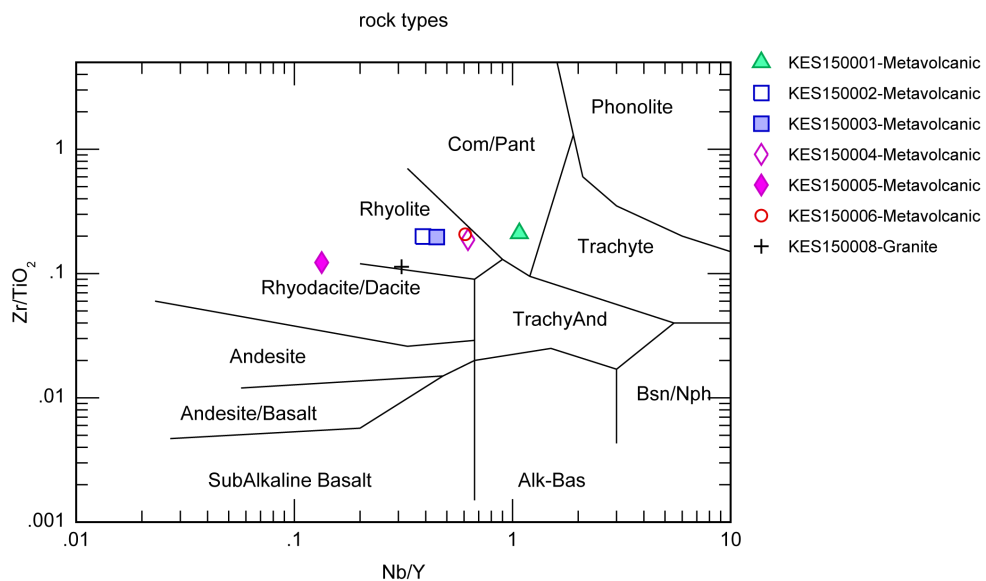


Fig. 19. Geochemical rock classification diagram after Winchester & Floyd (1977). KES150007 is below detection limit for one or several of the components and hence omitted.

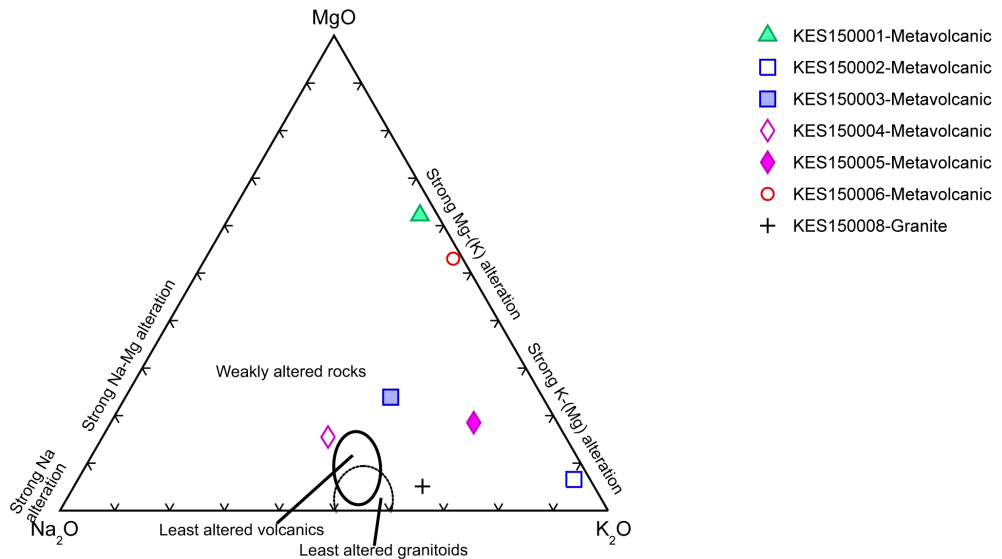


Fig. 20. Whole-rock Na₂O-K₂O-MgO triangular diagram. KES150007 is below detection limit for the alkalis and has hence been omitted. The figure suggests that KES150001 and KES150006 have undergone strong Mg-(K) alteration, whereas KES150003 underwent strong K-(Mg) alteration. KES150003, KES150004, KES150005 are weakly altered. Least altered rocks plot in the middle of the bottom axis. Modified after Hallberg (2003) and Holtstam et al. (2014).

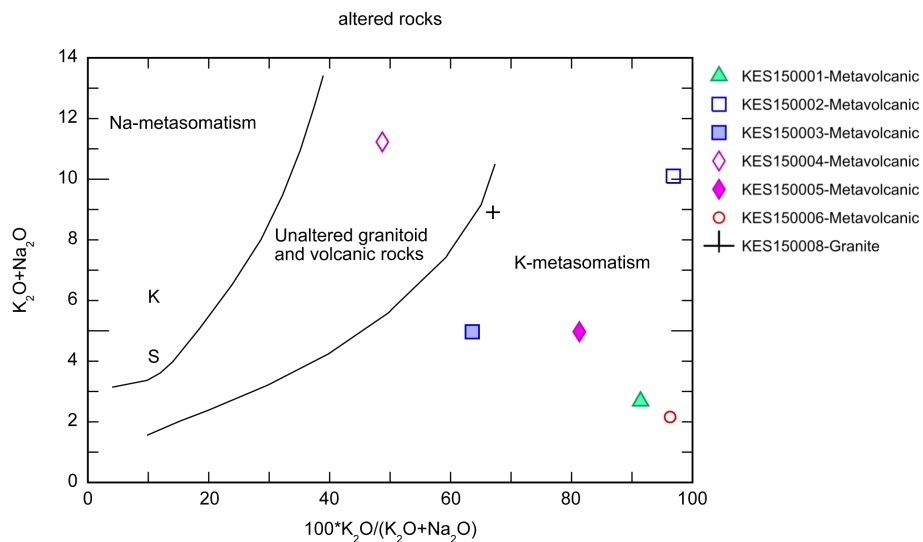


Fig. 21. Variation in alkali for the rocks shown in the igneous spectrum of Hughes (1972), modified after Holtstam et al. (2014).

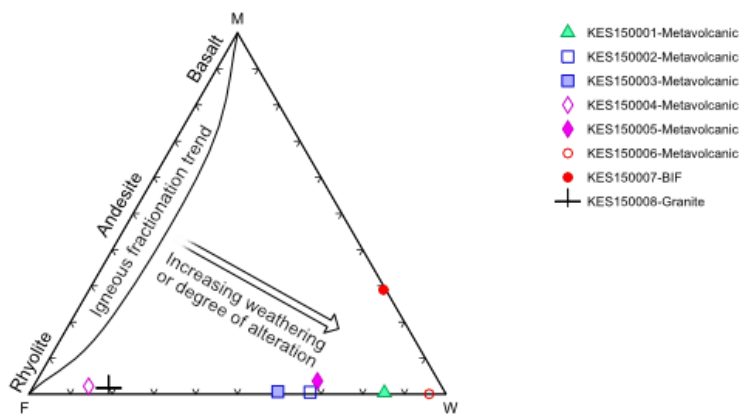


Fig. 22. Weathering index diagram that shows how the samples differs from the igneous fractionation trend. The felsic index (F), the weathering index (W) and the mafic index (M) are calculated according to Ohta & Arai (2007).

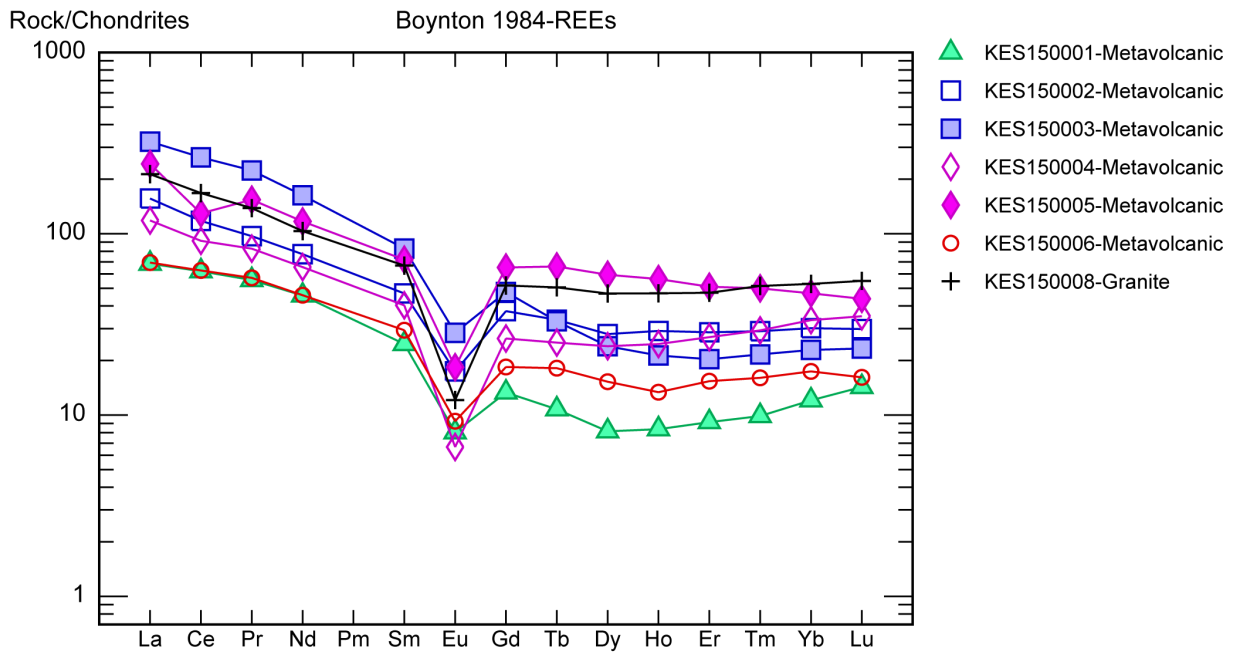


Fig. 23. Rock/chondrite spider diagram showing relationships between LREE (such as La, Ce) and HREE (such as Yb, Lu). Chondrite values follow those in Boynton (1984).

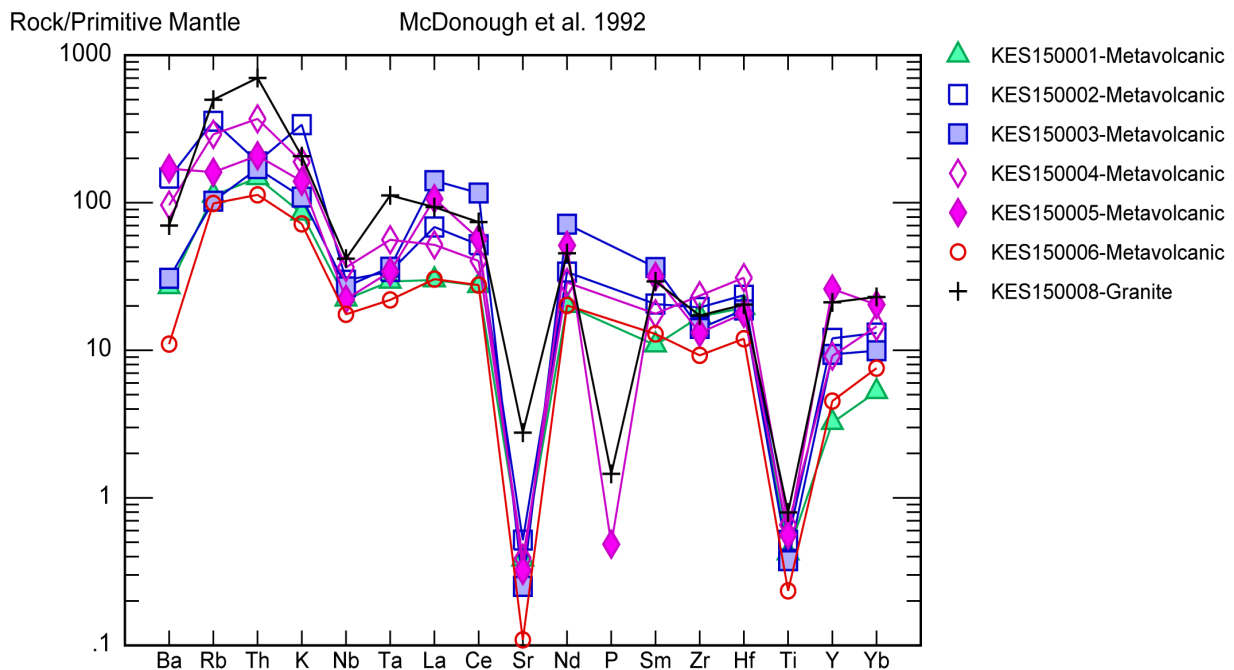


Fig. 24. Rock/primordial mantle spider diagram showing relationships between LILE (such as Ba, Rb) and HFSE (such as Zr, Ti and Y). Primitive mantle values from McDonough et al. (1992).

(>+100%); Ba at (>+80%); Sc, Y, La, Ce, Tb and Gd with (>+60%); Fe₂O₃, Rb, Pr, Nd, Sm, Dy and Ho at (>+40%); SiO₂, Er and Tm with (>+20%). Nb and Yb are slightly enriched whereas Sc and Ga show only minor depletion. TiO₂ and Lu plot on the isocon. Several elements are depleted: Na₂O and Mo with (>-80%); Zn, Ni and CaO at (>-60%); Pb, MgO and Cs with (>-40%); Be, Sn, Ta, Th and U at (>-20%). Overall, the slope of the isocon (0.79x) indicates significant mass gain of c. +27%.

KES150003 – metavolcanic rock (old Cu process plant, west of Bäckegruvan)

Fe₂O₃, Co, La, Ce, Pr, Nd, Eu and Sm are most strongly enriched with (>+200%) (Fig. 28). Other enriched components are: Gd and Tb at (>+100%); SiO₂ with (>+60%); Y and Dy at (>+40%); Ho at (>+20%). Mo, MgO, Be, Nb, Er and Tm show a slight enrichment while Pb, K₂O, TiO₂ and Ga are insignificantly depleted. Ta, Sr, Yb and Lu plot on the isocon. Zn and CaO are most strongly depleted with (>-80%). Other deplet-

ed elements are: Ni and Cs with (>-60%); Na₂O, Ba and Rb at (>-40%); Sc, Sn, Th and U (>-20%). Overall, the slope of the isocon (0.64x) indicates significant mass gain of c. +55%.

KES150005 – metavolcanic rock (Nya Bastnäs, close to the mines)

Mo, Y, La, Eu, Gd, Tb, Dy and Ho are most strongly enriched (>+200% (Fig. 29). Other enriched elements are: Ba, Co, Ce, Pr, Nd, Sm, Er, Tm and Yb at (>+100%); Lu with (>+80%); Ni and SiO₂ at (>+40%); CaO, TiO₂, Sc, Be and Sr with (>+20%). K₂O shows an insignificant enrichment while MgO, Ga, Nb, Rb, Ta, Th and U show minor depletion. Sn plots on the isocon. Depleted elements are: Na₂O and Zn at (>-60%); Pb and Cs at (>-20%). The slope of the isocon (0.64x) indicates significant mass gain of c. +57%.

KES150006 – metavolcanic rock (Bastnäs Storgruvefält, the northwestern part)

Sn, Co, SiO₂ and Eu are heavily enriched (>+200% (Fig. 30). Other enriched elements are: Fe₂O₃ and MgO with (>+100%); Ga at (>+80%); Ce, Pr, Nd, Sm, Gd and Tb with (>+60%); Dy at (>+40%); La, Ho, Er, Tm and Yb at (>+20%). Nb and Y are only slightly enriched while K₂O, TiO₂ and Ta are insignificantly depleted. Sc, Cs and Lu plot on the isocon. Elements showing depletion are: Mo, CaO and Na₂O which are almost -100% depleted. Other depleted elements are: Zn and Ba at (>-60%); Pb at Ni with (>-40%); Be, Rb, Sr, Th and U at (>-20%). The slope of the isocon (0.42x) indicates significant mass gain of c. +139%.

Average of metavolcanic rocks

In an average versus the unaltered sample (KES150004) plot (Fig. 31), Fe₂O₃, Co and Eu display strong mass gain at (>+200%). Other enriched components are: La, Ce, Pr, Nd, Sm, Gd and Tb with (>+100%); Mo and Y at (>+80%); SiO₂, Dy and Ho with (>+60%); MgO and Er at (>+40%); K₂O, Ba, Sr and Tm with (>+20%). TiO₂, Ga, Nb, Lu and Yb show insignificant mass gain whereas Sc, Rb and Ta show very minor mass loss. Several components are depleted: Na₂O at (>-80%); Zn with (>-60%); CaO, Ni with (>-40%); Pb, Be, Cs, Th, U at (>-20%). The slope of the isocon (0.63x) indicates an overall significant mass gain of c. +58%.

5.2 Geochronology

Zircons were found and separated from five samples; KES150001, KES150002, KES150003, KES150004 and KES150008, while in KES150005 only monazite was found. For KES150006, KES150007 and WL15002 no zircon or monazite was found. In WL15001 and Ö.Gytt-1, titanite and rutile were found, but time constraints and the lack of standards prevented further examination. 183 U-Th-Pb spot analyses were done in 182 zircon grains. Data that are <95%

concordant were rejected from age calculations. Of 151 spots in zircon from the metavolcanic rocks that host the REE mineralizations, 42 were culled due to the concordance criteria, leaving 109 analyses. Ages for the metavolcanic rocks were calculated with a weighted average. In sample KES150008 a large number of the spots were discordant and thus a <85% concordance criteria and an intercept age was used instead. All ages were, as noted before, calculated using Isoplot 4.15 (Ludwig, 2008).

Geochronological data is tabulated in Appendix V and Tera-Wasserburg plots for all analyzed samples are shown broken down in each sub-section and listed together in Appendix VI. ²⁰⁶Pb/²⁰⁴Pb was not measured during analysis due to mass interference from ²⁰⁴Hg. All errors are reported at the 2 sigma level unless anything else is stated. Age histograms of zircon analyses for the metavolcanic rock samples are shown at the back of this section. Zircon descriptions below follow those detailed in Corfu et al. (2003).

KES150001 – (assumed) metavolcanic rock (roadcut south of Forshammar)

Zircon crystals are ≤100 μm along the c-axis, anhedral to euhedral in shape. The population is diverse, both BSE-bright and BSE-dark cores exist. Some crystals contain BSE-bright acicular inclusions and are fractured to a variable degree (Fig. 32). 47 zircons were analyzed with one spot in each, ²⁰⁷Pb/²⁰⁶Pb-dates range from 1800 ± 14 Ma (spot S01_06 and Th/U=0.07) to 2086 ± 22 Ma (spot S01_07 and Th/U=0.52). 10 of the spots are more than 5% discordant and rejected from age calculations (Fig. 33). A ²⁰⁷Pb/²⁰⁶Pb weighted average for the remaining 37 spots yield a 1910 ± 5 Ma (MSWD=3.2; n=35/37) date (Fig. 33), with U from 180 ppm to 1423 ppm and Th/U from 0.3 to 0.7, which is shown in Fig. 44, 45 and 46 at the end of this section.

KES150002 – metavolcanic rock (outcrop north of Riddarhyttan, close to Källfallet)

Zircon crystals are ≤100 μm along the c-axis, anhedral to euhedral (Fig. 34). Most grains are homogeneous but a few show oscillatory growth zoning, sometimes pronounced and sometimes weak but all with BSE-bright cores. The majority of the grains exhibit cracks and a few grains also have BSE-bright inclusions. 43 zircons were analyzed with one spot in each, ²⁰⁷Pb/²⁰⁶Pb-dates range from 1871 ± 18 Ma (spot S02_39 and Th/U=0.75) to 2000 ± 22 Ma (spot S02_03 and Th/U=0.50). 9 of the spots are more than 5% discordant and rejected from age calculations (Fig. 35). A ²⁰⁷Pb/²⁰⁶Pb weighted average for the remaining 34 spots yield a 1899 ± 4 Ma (MSWD=2.2; n=33/34) date, with U from 274 ppm to 1223 ppm and Th/U from 0.3 to 0.7, which is shown in Fig. 44, 45 and 46 at the end of this section.

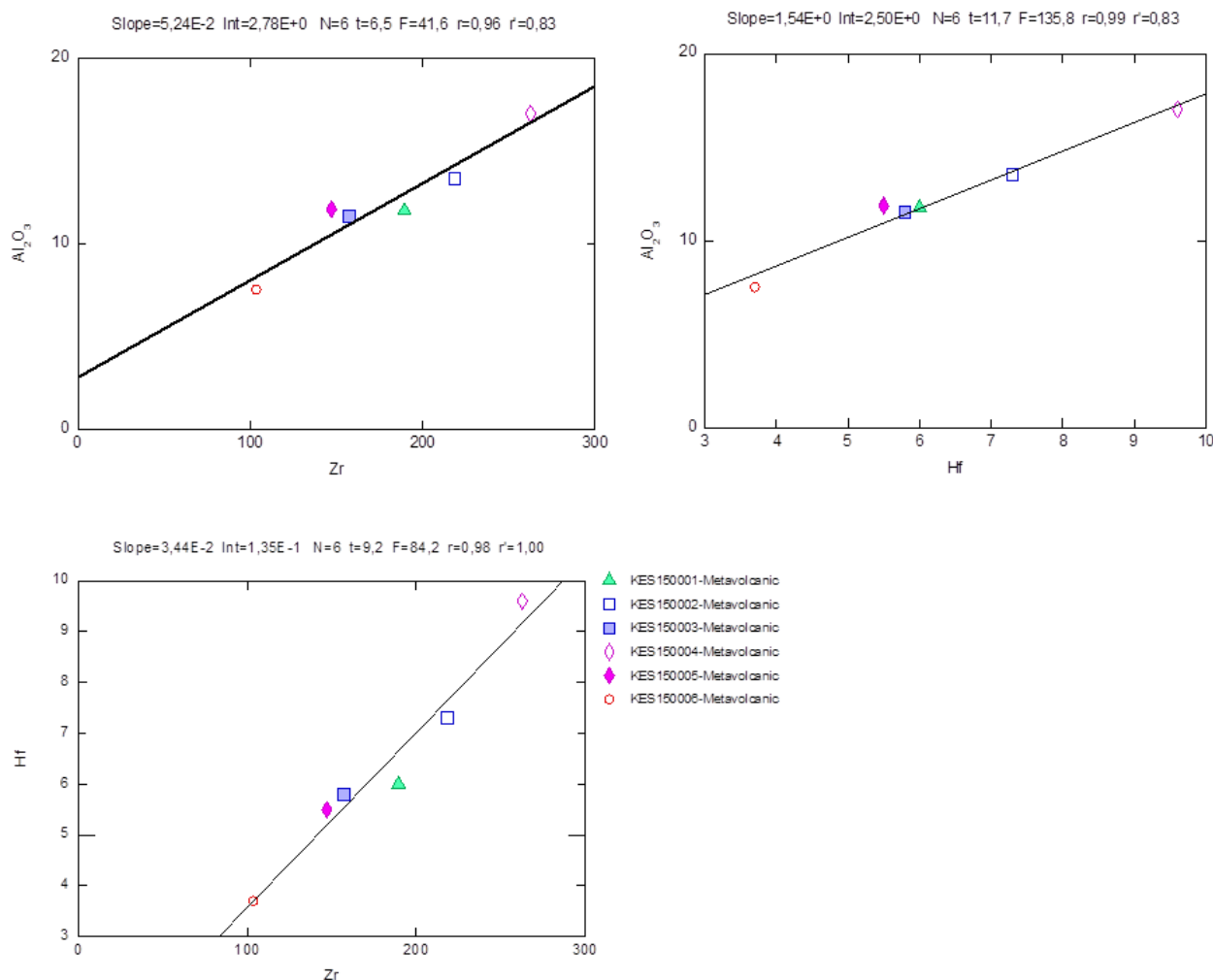


Fig. 25. Binary immobile element plots for samples KES150001-0006 with linear regressions. Top left: Al₂O₃ (wt. %) vs. Zr (ppm). Top right: Al₂O₃ (wt. %) vs. Hf (ppm). Lower left: Hf (ppm) vs. Zr ppm.

Table 7. Immobile element ratios with their calculated *r*-values. Values >95 have been highlighted.

	Al ₂ O ₃					
Al ₂ O ₃	–	TiO ₂				
TiO ₂	0.91	–	Nb			
Nb	0.94	0.75	–	Zr		
Zr	0.96	0.79	0.91	–	Hf	
Hf	0.99	0.84	0.96	0.98	–	Lu
Lu	0.55	0.80	0.44	0.32	0.44	–

KES150003 – metavolcanic rock (old Cu process plant, west of Bäckegruvan)

Zircon crystals are ≤100 μm along the c-axis and anhedral to euhedral in shape. The population is diverse, some crystals have BSE-bright cores while others have BSE-dark ones. Many grains have accessory BSE-bright mineral inclusions of apatite, these accessory minerals also often occur along the edges of the crystals (Fig. 36). The majority of the grains are cracked.

Some grains show an oscillatory growth zoning with a large variation in zonation intensity while others have a heterogeneous patch pattern. 38 zircons were analyzed with one spot in each, ²⁰⁷Pb/²⁰⁶Pb-dates range from 1592 ± 19 Ma (spot S03_08 and Th/U=0.22) to 2032 ± 25 Ma (spot S03_35 and Th/U=0.30). 13 of the spots are more than 5% discordant and rejected from age calculations (Fig. 37). A ²⁰⁷Pb/²⁰⁶Pb weighted average for the remaining 25 spots yield a 1911 ± 6 Ma

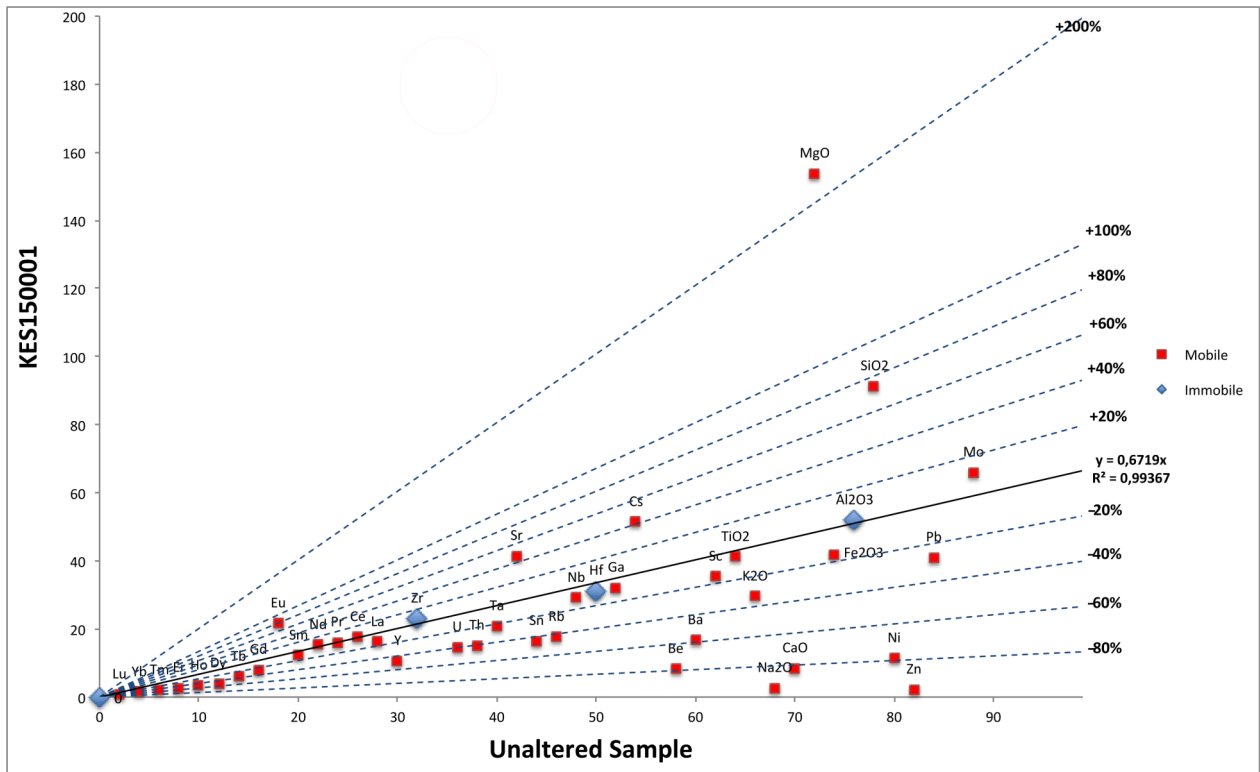


Fig. 26. Isocon diagram showing the relative mass changes that occurred during alteration. An altered sample (KES150001) is compared with that of an unaltered sample (KES150004). Blue dashed lines are inserted as references of relative net gain/loss. Al_2O_3 , Zr and Hf are considered as immobile and used in order to define an isocon that starts in the origin. Note that Co is omitted from the plot.

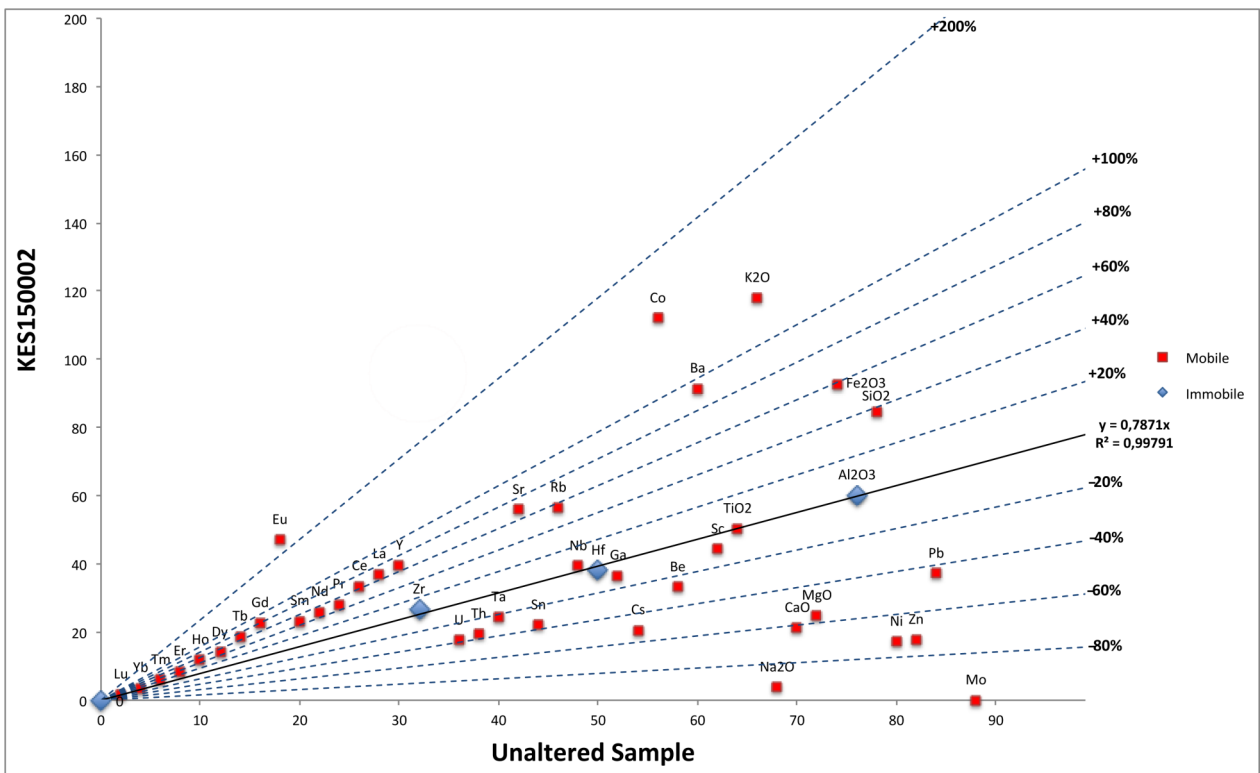


Fig. 27. Isocon diagram showing the relative mass changes that occurred during alteration. An altered sample (KES150002) is compared with that of an unaltered sample (KES150004). Blue dashed lines are inserted as references of relative net gain/loss. Al_2O_3 , Zr and Hf are considered as immobile and used in order to define an isocon that starts in the origin.

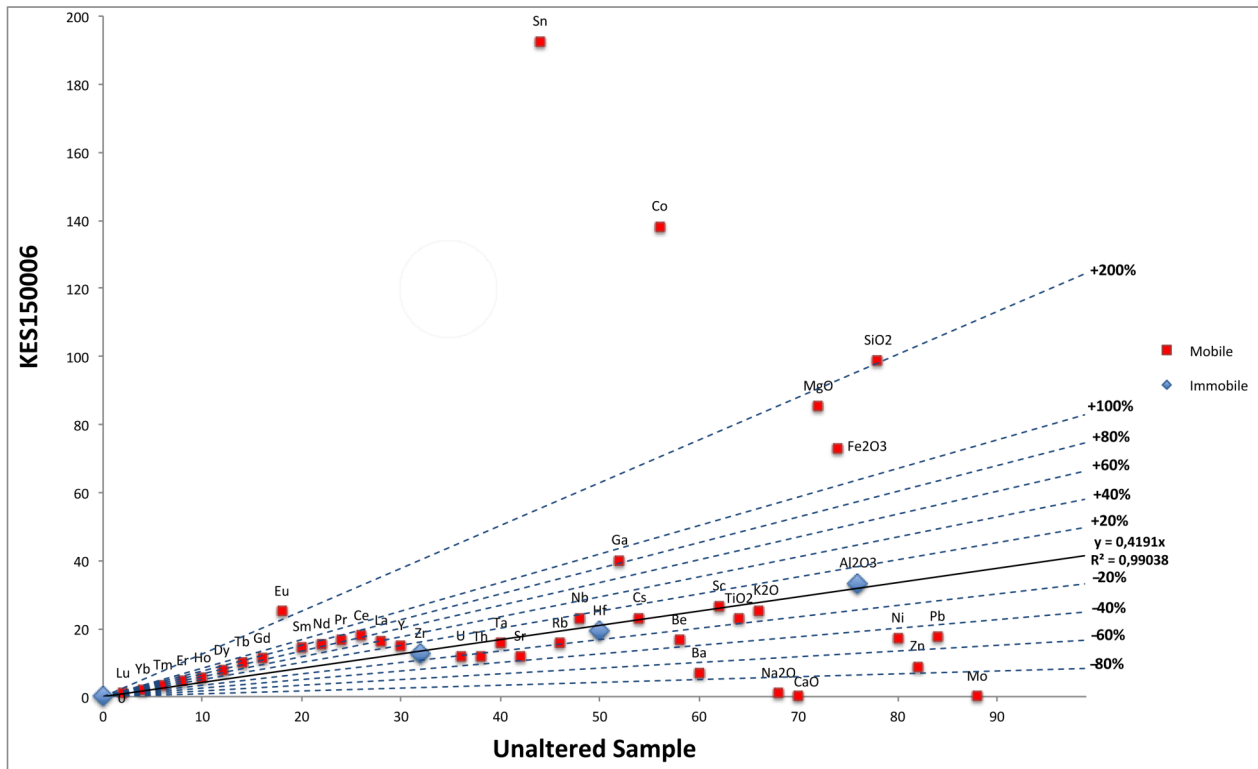


Fig. 30. Isocon diagram showing the relative mass changes that occurred during alteration. An altered sample (KES150006) is compared with that of an unaltered sample (KES150004). Blue dashed lines are inserted as references of relative net gain/loss. Al_2O_3 , Zr and Hf are considered as immobile and used in order to define an isocon that starts in the origin.

(MSWD=3.2; $n=24/25$) date, with U from 137 ppm to 1417 ppm and Th/U from 0.3 to 0.7, which is shown in Fig. 44, 45 and 46 at the end of this section.

KES150004 – metavolcanic rock (roadcut west of Bjursjön)

Zircon crystals are $\leq 100 \mu\text{m}$ along the c-axis and anhedral to euhedral in shape. About half of the crystals are homogeneous and free from zonation while the other half shows pronounced oscillatory growth zoning with both BSE-bright and BSE-dark cores (Fig. 38). In only a few grains the zoning is convolute with a heterogeneous patch pattern. The population is generally free from inclusions but fractured to various degree; some grains show trace of metamictization. 23 zircons were analyzed with one spot in each, $^{207}\text{Pb}/^{206}\text{Pb}$ -dates range from $1825 \pm 10 \text{ Ma}$ (spot S04_14 and Th/U=0.99) to $1986 \pm 12 \text{ Ma}$ (spot S04_12 and Th/U=0.77). 10 of the spots are more than 5% discordant and rejected from age calculations (Fig. 39). A $^{207}\text{Pb}/^{206}\text{Pb}$ weighted average for the remaining 13 spots yield a $1916 \pm 4 \text{ Ma}$ (MSWD=1.4; $n=12/13$) date, with U from 521 ppm to 1411 ppm and Th/U from 0.4 to 1.1 which is shown in Fig. 44, 45 and 46 at the end of this section.

KES150005 – metavolcanic rock (Nya Bastnäs, close to the mines)

Monazite crystals are $\leq 70 \mu\text{m}$ along the c-axis, anhedral to subhedral in shape with slightly rounded morphology (Fig. 40). The grains in the population are generally homogeneous with no or only a faint oscilla-

tory growth zonation and no visible cores. The grains are fractured to a variable degree and mostly free from inclusions. 59 monazites were analyzed with one spot in each, $^{207}\text{Pb}/^{206}\text{Pb}$ -dates range from $1774 \pm 52 \text{ Ma}$ (spot S05_09) to $2080 \pm 41 \text{ Ma}$ (spot S05_57). 8 of the spots are more than 5% discordant and rejected from age calculations (Fig. 41). A $^{207}\text{Pb}/^{206}\text{Pb}$ weighted average for the remaining 51 spots yield a $1824 \pm 7 \text{ Ma}$ (MSWD=1.2; $n=48/51$) date.

KES150008 – Granite (Högfors Storgruva)

Zircon crystals are $\leq 120 \mu\text{m}$ along the c-axis, subhedral to euhedral in shape. Both BSE-bright and BSE-dark cores exist. Almost every grain in the population show oscillatory growth zoning that is more or less overprinted by irregular BSE-bright domains (Fig. 42). The grains are generally fractured and a few grains have inclusions. 31 zircons were analyzed with one spot in each and one zircon with two spots. $^{207}\text{Pb}/^{206}\text{Pb}$ -dates range from $1583 \pm 12 \text{ Ma}$ (spot S08_23 and Th/U=0.55) to $1850 \pm 9 \text{ Ma}$ (spot S08_40 and Th/U=0.08). Almost the entire population plots highly discordant with 15 analyses being within a <15% discordance limit. An intercept age (Fig. 43), yield a $1822 \pm 10 \text{ Ma}$ (MSWD=1.7) date, with U from 811 ppm to 4283 ppm and Th/U from 0.3 to 33.1. Spot S08_16 ($1823 \pm 13 \text{ Ma}$) and S08_17 ($1805 \pm 16 \text{ Ma}$) were carried out in the same zircon.

Histogram plots based on <5% discordance values for the felsic metavolcanic samples KES150001-0004 are shown in Fig. 44. Due to discordance in almost all

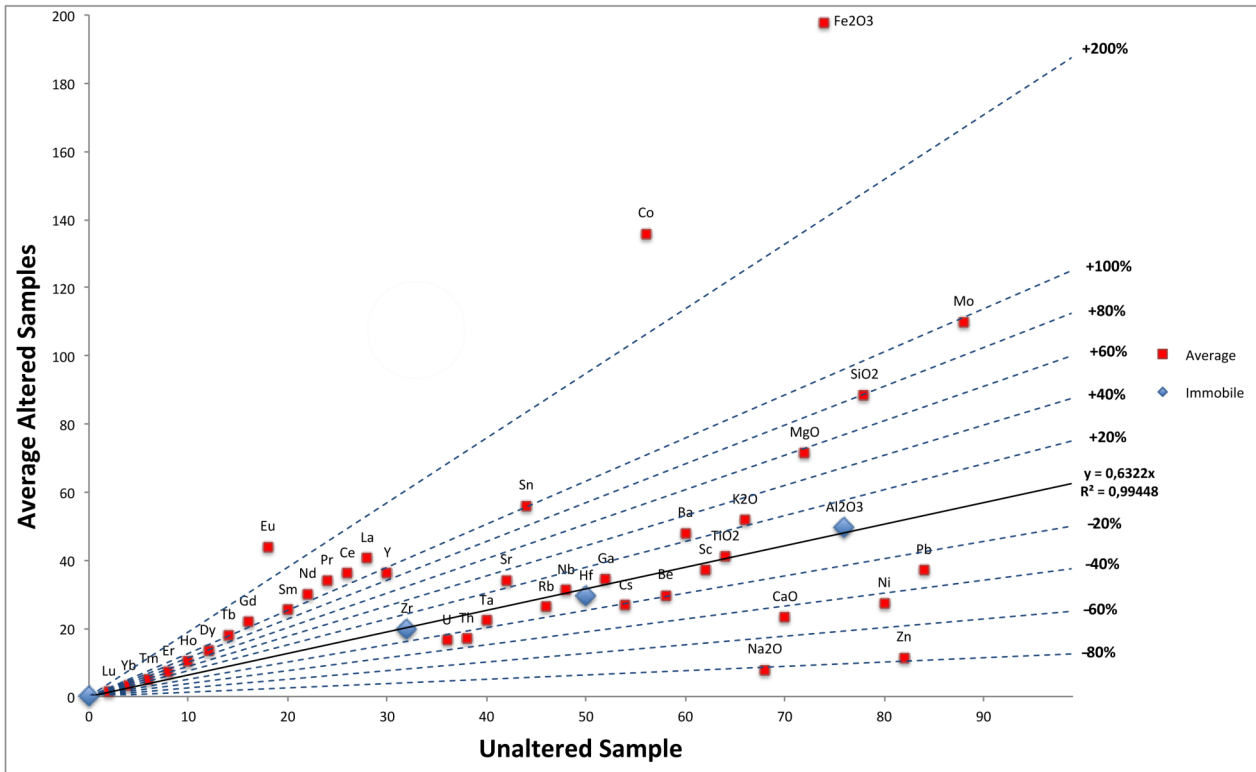


Fig. 31. Isocon diagram showing the relative mass changes that occurred during alteration. The averages of the altered samples are compared with that of an unaltered sample (KES150004). Blue dashed lines are inserted as references of relative net gain/loss. Al_2O_3 , Zr and Hf are considered as immobile and used in order to define an isocon that starts in the origin.

analyzed zircons no histogram was made for KES150008. Plots of Th/U vs. $^{207}\text{Pb}/^{206}\text{Pb}$ ages for the different samples are shown in Fig. 45. In Fig. 46, diagrams displaying Th/U vs. concordance are found.

6 Discussion

6.1 Geochemical signatures of the metavolcanic rocks

The metavolcanic rocks in this study are mostly of rhyolitic composition. Al_2O_3 is rather high in comparison with the alkali elements and the rocks are strongly peraluminous. There is a general variation in major element concentration between samples KES150001-0006. FeO_t is almost constant for any given MgO while CaO is extremely low with <0.5 wt% (sometimes even below detection limit) in all the samples. This suggests that fractional crystallization processes plays only a minor role for the cause of the element variation. Instead, alteration processes likely more readily explain the geochemical variations. If the samples originate from a similar rhyolitic precursor, they must thus have undergone various degrees of alteration, accompanied by mass and volume changes in order to accompany for these variations.

The chondrite and mantle normalised trace element patterns are similar to those presented by e.g. Holtstam et al. (2014) and Stephens et al. (2009) and distinctive for the Svecofennian volcanic and sub-volcanic suite of rocks. Especially notable are the pro-

nounced negative anomalies for Nb, Ta, Sr, P (several samples in this study were below detection limit) and Ti, which is a pattern comparable to that found in a normal to mature, active continental margin (Stephens et al. 2009; Brown et al. 1984). However, it should be noted that Cs, Pb, Sr, P and Ti are on average lower than comparative values from a mature arc environment, e.g. Andean rhyolites (Fig. 47), GEOROC, 2016). The (La/Yb)_{chond} values indicate a depletion in HREE and enrichment of LREE for all samples, something that is also seen in the primitive mantle and chondrite normalized REE spider diagrams. REE contents are subparallel but generally higher than those seen in the Andean rhyolites. All samples display distinct negative Eu anomalies, with both Eu/Eu* and Sr lower than arc rhyolites in general. The negative Eu anomalies are normally attributed to either plagioclase fractionation or alteration, but since there is no negative CaO trend, as it would normally be during fractionation, alteration is likely the responsible process. An interesting and thought-provoking line of thought is thus how much of the primary major and trace element signals that remain in the rocks and how much of the geochemical variation that can be contributed to alteration processes, something that will be further examined in the next section.

6.2 Isocon data

6.2.1 Implications of the isocon diagrams

As has been shown in the different discrimination dia-

grams, there is a large internal variability among the different felsic metavolcanic rock samples, which suggests that a whole range of elements must have been either gained or lost during alteration. Assessing these changes are, however, not straightforward since the major elements are normalized to 100% and any apparent changes will not represent the true values. To exemplify this, a hypothetical increase in Al_2O_3 during alteration can be used. An increase in this one component would seem to lead to depletion in all other components due to the normalization to 100 wt.%. There is, conversely, no absolute decrease, only a relative, since the amount of all elements stays the same except for Al_2O_3 that increases. The advantage of instead using the isocon method is that it uses a suite of generally immobile elements to create a line of reference, an isocon, which all gains and losses are compared to. Thus it allows for the evaluation of gains and losses during alteration in a more proper way than by simply comparing values for the different components with each other.

An important point to keep in mind is that the selection and designation of the least altered sample is of uttermost importance since it is the sample that everything will be compared with. In this study this sample was carefully chosen based on a number of factors: field evidence, thin section analysis and the index of alteration and the weathering index diagram. There are, however, always uncertainties involved when determining what sample that is least altered/unaltered, and in this case there is likely no completely unaltered samples.

The isocon diagrams display large variations in net mass gain/loss among the different samples, both for major- and trace elements. This implies that few of the signatures shown in major- and trace element data is of primary igneous origin but is rather due to one or several stages of alteration, which has been suggested and addressed by numerous workers in the Bergslagen region (e.g. Stephens et al. 2009 and references therein). The isocon plots do, nonetheless, further support the interpretation that the variation in the geochemical data is not caused by fractional crystallization, as discussed above. In addition to this, the precursor-alteration relationship is supported by the binary immobile element plots where elements commonly viewed as immobile (such as Al, Zr and Hf) indeed have similar ratios in the different felsic metavolcanic rocks as well as good linear correlations in the isocon diagrams. This also holds true in the weathering index diagram where all the samples plot along the lower axis, creating a linear trend.

SiO_2 ; MgO, K_2O ; Co; Eu and Fe_2O_3 were gained in three (or more) of the five samples whereas Pb; Ni; Zn; Na_2O ; Th and U were lost in three (or more) of the samples. The Harker variation diagrams showed that CaO is unusually low, a fact that can be explained by the isocon diagrams. All plots except KES150005 vs. unaltered show that CaO was depleted between -60% to -100%. Another component that is strongly depleted

is Na_2O that had a mass loss between -40% to -100%. K_2O varied from +100% to -20% and MgO from +200% to -40%. Al_2O_3 has, as already noted, remained rather immobile and the peraluminous nature of the rocks is hence more readily explained by a pronounced loss of Na_2O and a slight overall increase in K_2O instead than by a dramatic increase of Al_2O_3 .

All the metavolcanic samples have undergone rather significant overall mass gain, ranging from +27% to +139%. When summarized the mass gains are: KES15001: +49%; KES150002: +27%; KES150003: +55%; KES150005: +57% and KES150006: +139%.

6.2.2 Pitfalls with the isocon method

As discussed earlier, the isocon was first defined by a linear regression through points in the origin, and the immobile elements Al, Zr and Hf. It should, however, be noted that other components could be used in defining the isocon. Three such components are: Er, Ho, and MgO because these components have CiA/CiO values close to 1 when the average values are used. An example of an isocon diagrams based on a linear regression through the origin and these three components is shown in Fig. 48. There are however large internal variations in both Er, Ho as well as in MgO. MgO is often a mobile component and hence a poor candidate when searching for immobile elements. The linear regression had an almost perfect fit with $y=0.9942x$ and since the net mass change is a direct function of the slope of the isocon this suggests negligible net mass change.

In this example, Eu, Co and Fe_2O_3 display strong mass gain in the order of (>+150%). Light and middle REE are less enriched where La, Ce, Pr, Nd, Gd display mass gains around (>+40%). Mo, Sn, Y, Sm and Tb at (>+20%); SiO_2 with (>+10%). Several components are depleted: Na_2O and Zn with (>-80%); Ni and CaO at (>-60%); Pb, Sc, Be, Cs, Hf, Rb, Ta, Th and U with (>-40%); Al_2O_3 , K_2O , TiO_2 , Ba, Ga, Nb and Zr at (>-20%) and Sr with (>-10%).

The internal variations in concentration of each component can be seen when the averages and each specific altered sample are plotted against KES150004 (Fig. 49) in isocon diagrams similar to that in Fig. 48. Note that the Fe-value for KES150005 is 617% and the Co-value for KES150001 is 215% and these are omitted from the plot. The internal variation between the components is pronounced. Depending on which of the samples that are investigated, several of the following components exhibit both enrichment and depletion: Mo, Fe, Mg, K, Ba, Rb, Sn, Sr and all the LREE except Eu, which is enriched in all samples.

It should be noted that the difference between using MgO, Er and Ho or Al_2O_3 , Zr and Hf when defining the isocon is pronounced. The plots went from having isocon slopes equal to 1, indicating zero mass gain/loss to slopes far less than 1, indicating significant mass gain. The reason to this is probably because of the average values used for MgO, Er and Ho. It is important to note that averaging destroys not only any

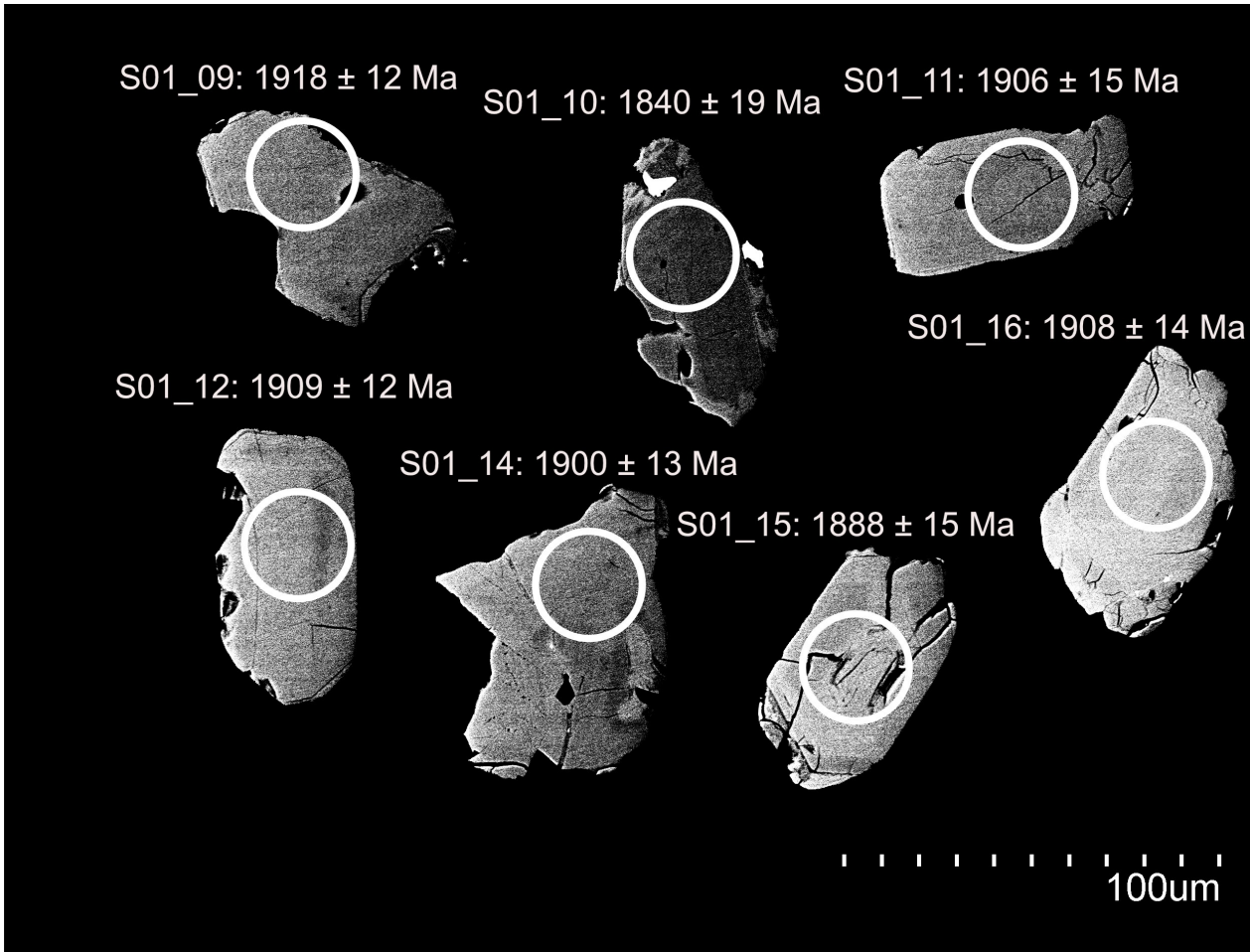


Fig. 32. BSE-images of selected zircon grains from metavolcanic sample KES150001. Analysis sites for U-Pb LA-ICP-MS are marked with white circles and corresponding $^{207}\text{Pb}/^{206}\text{Pb}$ ages are given.

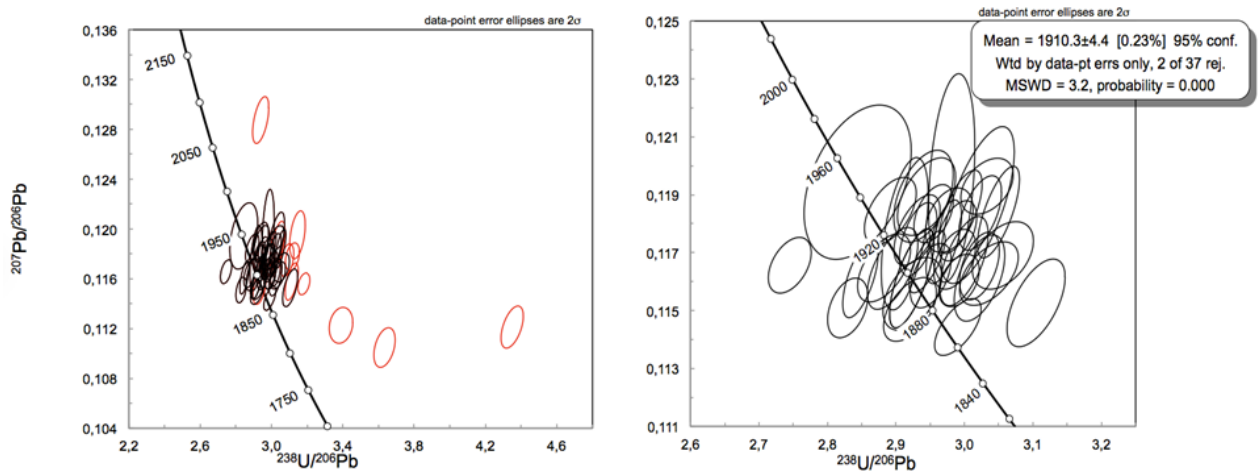


Fig. 33. Tera-Wasserburg plots for sample KES150001 (zircon) and its associated weighted average calculation based on $^{207}\text{Pb}/^{206}\text{Pb}$ ages. Analyses with $>5\%$ discordance are marked as red and rejected.

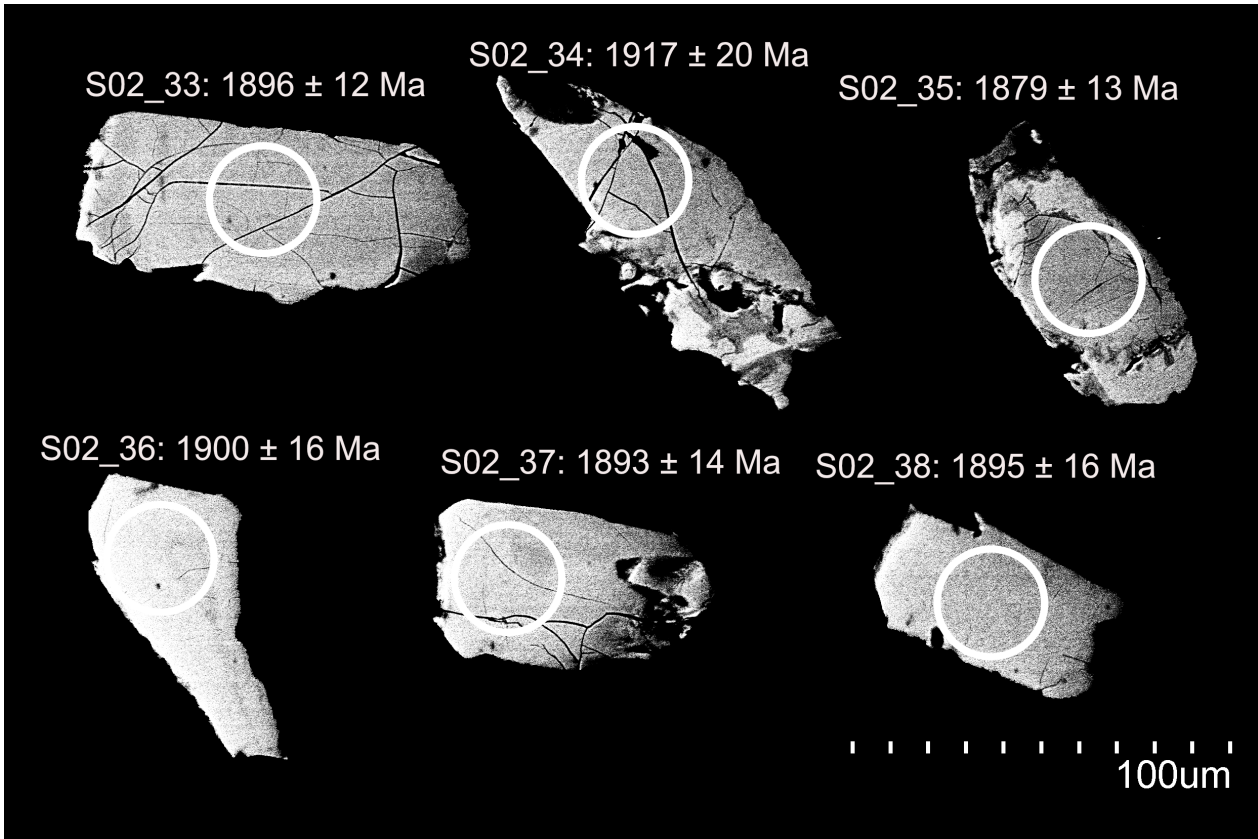


Fig. 34. BSE-images of selected zircon grains from metavolcanic sample KES150002. Analysis sites for U-Pb LA-ICP-MS are marked with white circles and corresponding $^{207}\text{Pb}/^{206}\text{Pb}$ ages are given.

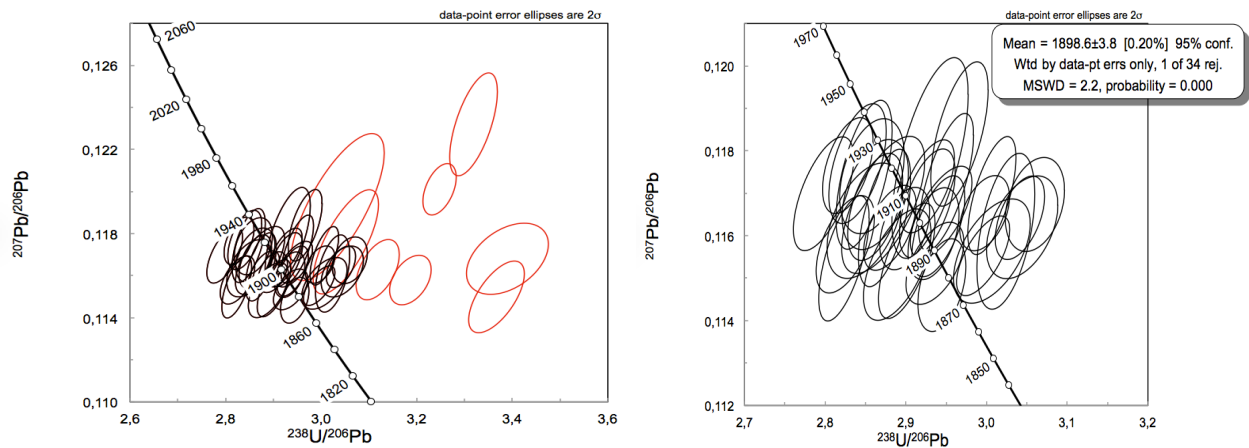


Fig. 35. Tera-Wasserburg plots for sample KES150002 (zircon) and its associated weighted average calculation based on $^{207}\text{Pb}/^{206}\text{Pb}$ ages. Analyses with $>5\%$ discordance are marked as red and rejected.

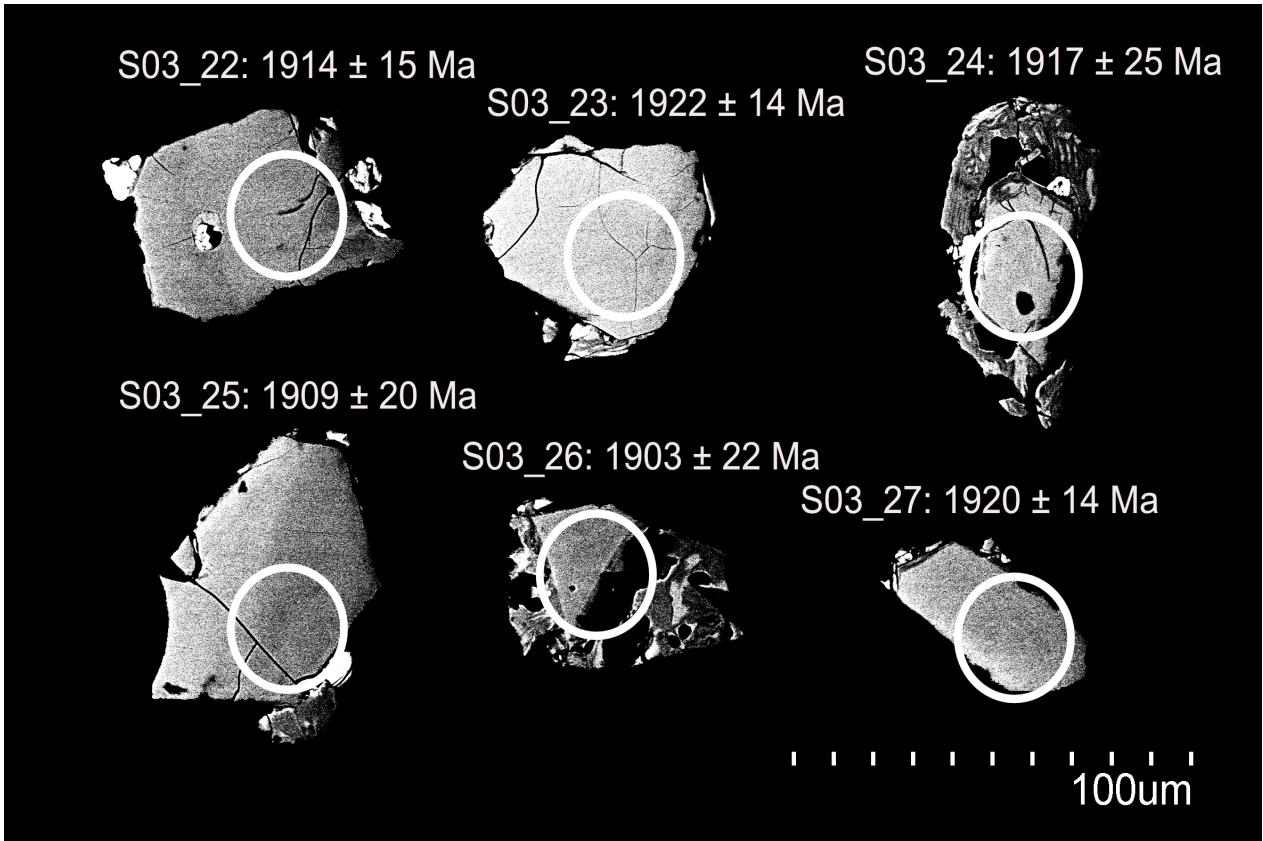


Fig. 36. BSE-images of selected zircon grains from metavolcanic sample KES150003. Analysis sites for U-Pb LA-ICP-MS are marked with white circles and corresponding $^{207}\text{Pb}/^{206}\text{Pb}$ ages are given.

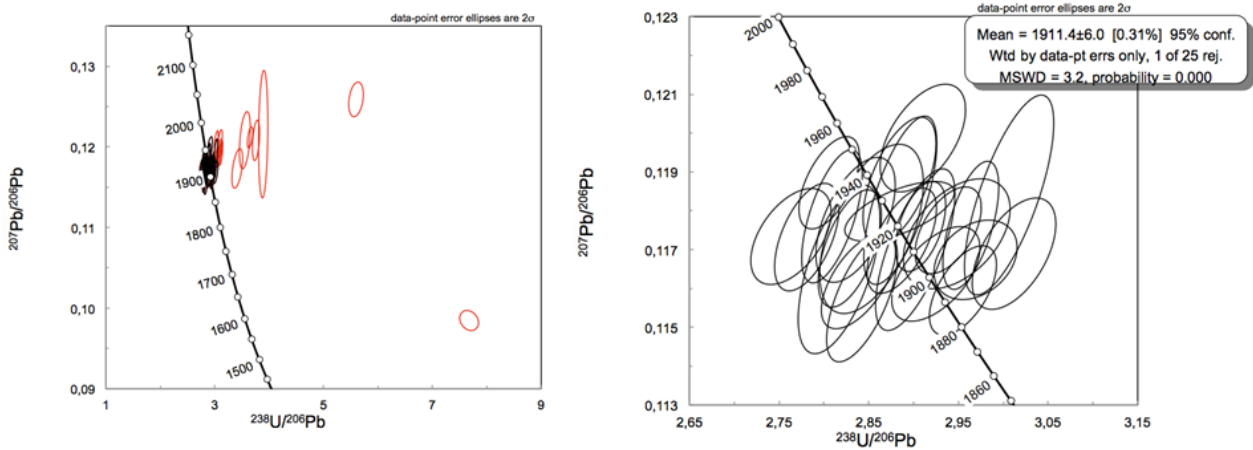


Fig. 37. Tera-Wasserburg plots for sample KES150003 (zircon) and its associated weighted average calculation based on $^{207}\text{Pb}/^{206}\text{Pb}$ ages. Analyses with $>5\%$ discordance are marked as red and rejected.

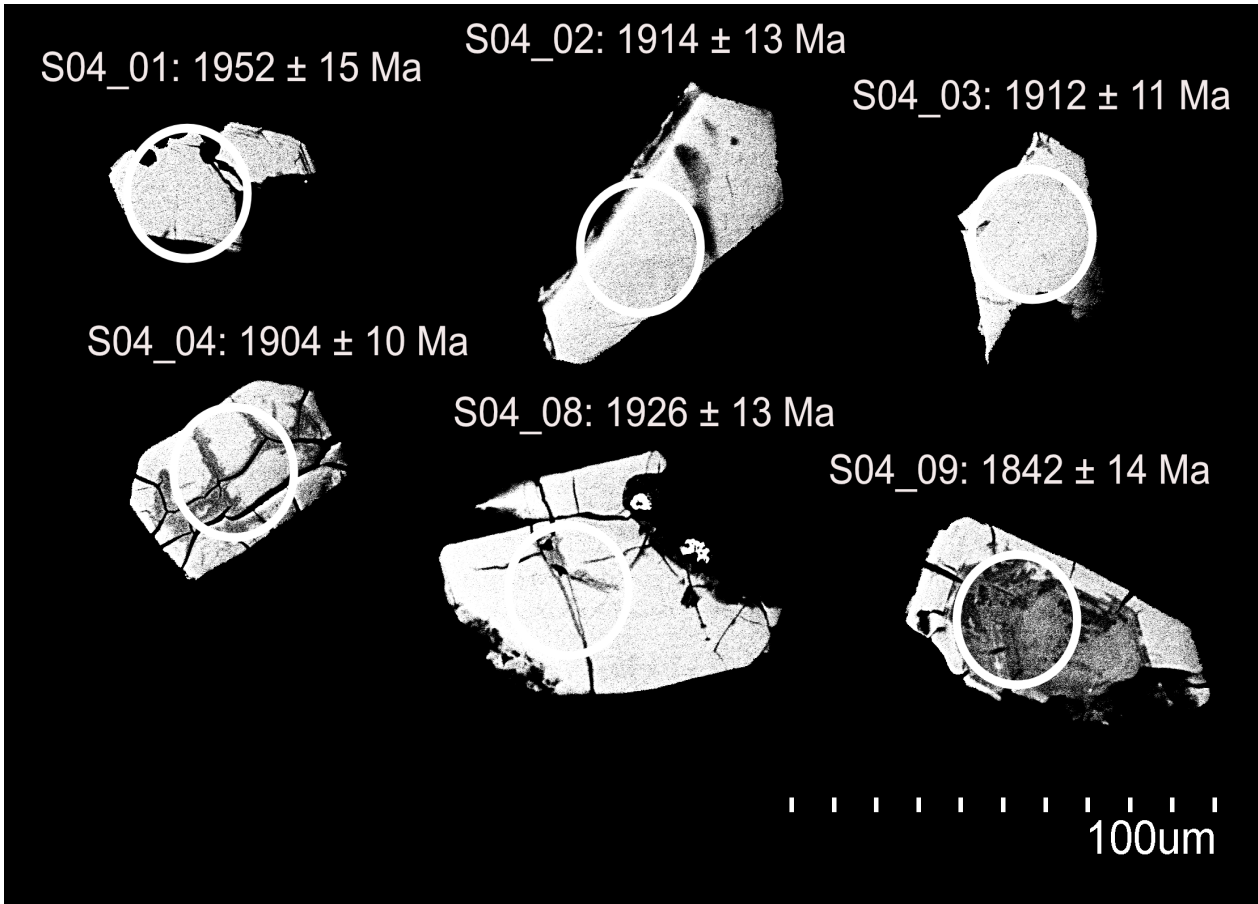


Fig. 38. BSE-images of selected zircon grains from metavolcanic sample KES150004. Analysis sites for U-Pb LA-ICP-MS are marked with white circles and corresponding $^{207}\text{Pb}/^{206}\text{Pb}$ ages are given.

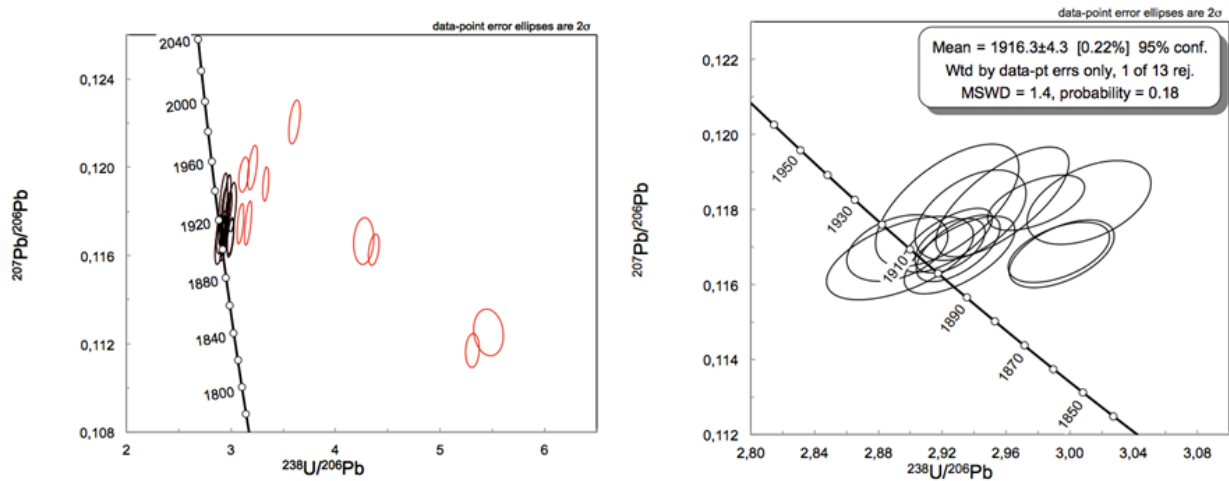


Fig. 39. Tera-Wasserburg plots for sample KES150004 (zircon) and its associated weighted average calculation based on $^{207}\text{Pb}/^{206}\text{Pb}$ ages. Analyses with >5% discordance are marked as red and rejected.

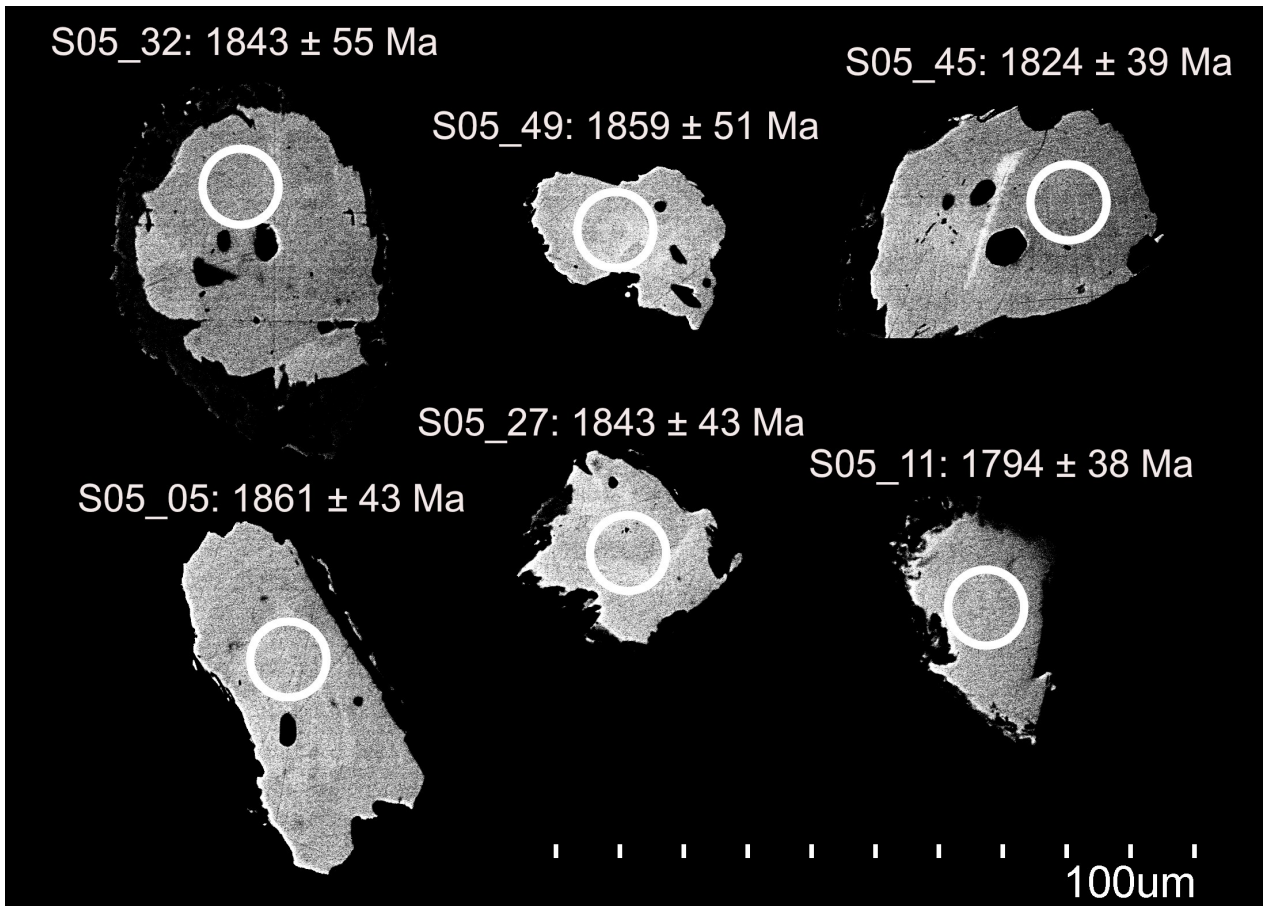


Fig. 40. BSE-images of selected monazite grains from metavolcanic sample KES150005. Analysis sites for U-Pb LA-ICP-MS are marked with white circles and corresponding $^{207}\text{Pb}/^{206}\text{Pb}$ ages are given

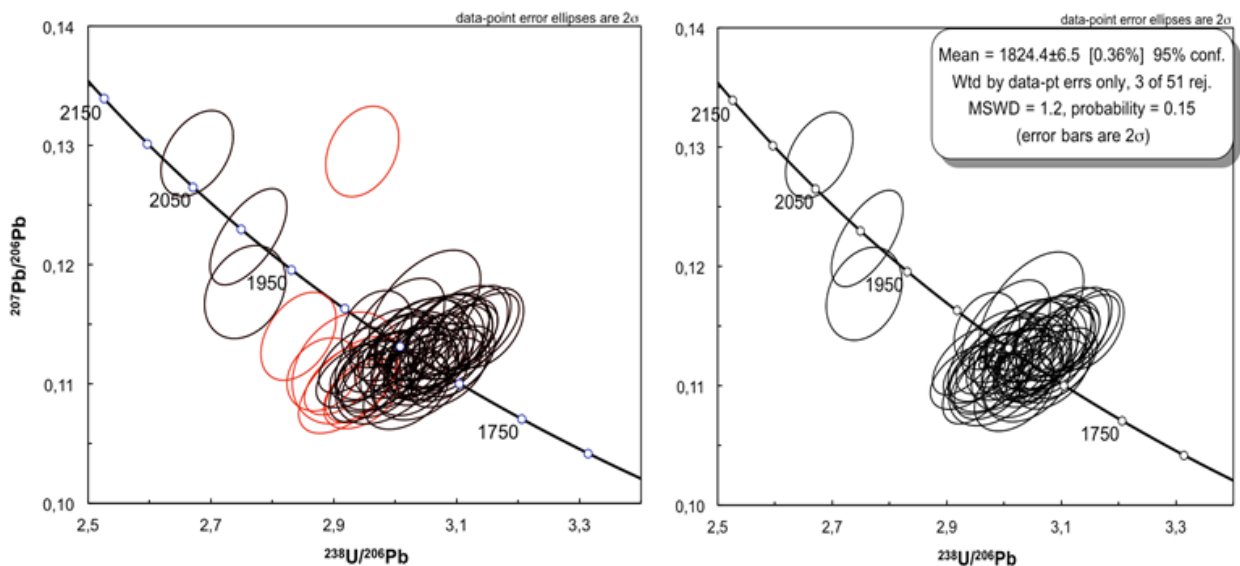


Fig. 41. Tera-Wasserburg plots for sample KES150005 (monazite) and its associated weighted average calculation based on $^{207}\text{Pb}/^{206}\text{Pb}$ ages. Analyses with $>5\%$ discordance are marked as red and rejected.

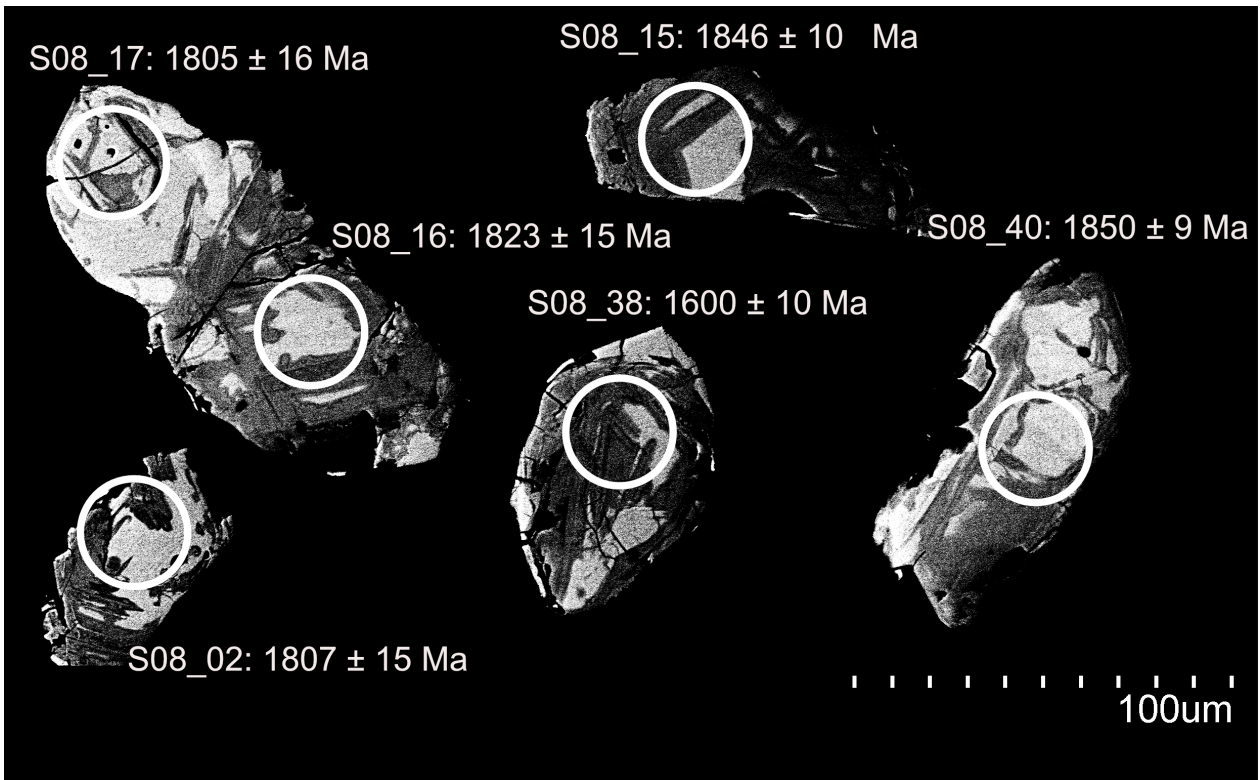


Fig. 42. BSE-images of selected zircon grains from granite sample KES150008. Analysis sites for U-Pb LA-ICP-MS are marked with white circles and corresponding $^{207}\text{Pb}/^{206}\text{Pb}$ ages are given. Note that there are two spots in the grain in the upper left corner of the picture.

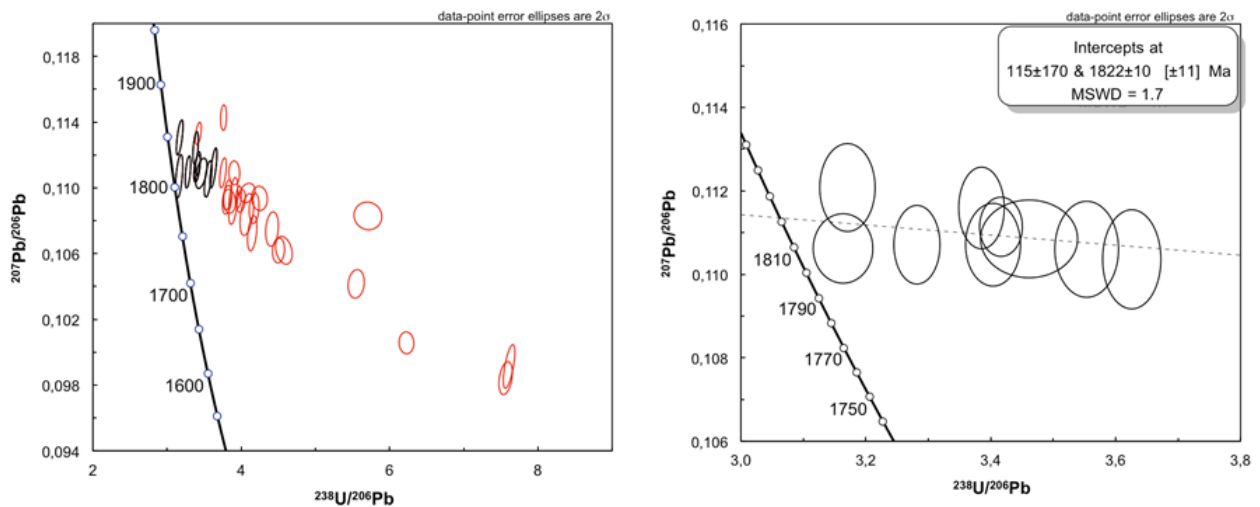


Fig. 43. Tera-Wasserburg plots for sample KES150008 (zircon) and its associated intercept age. Analyses with >15% discordance are marked as red and rejected.

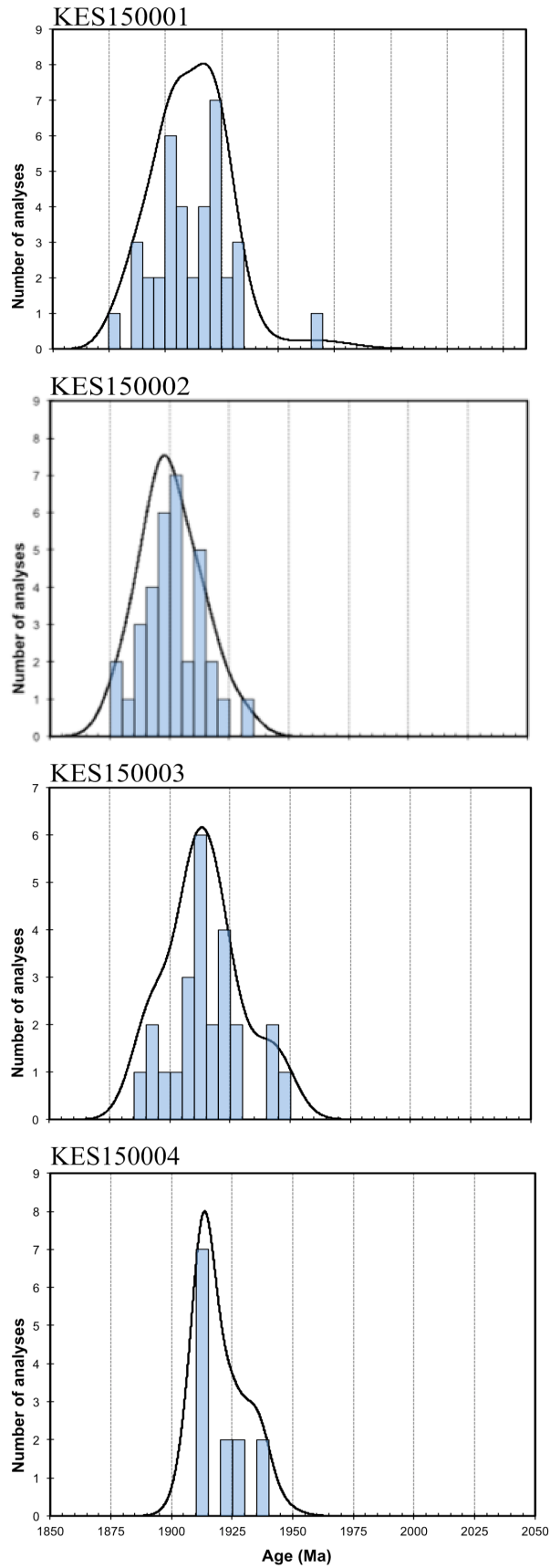


Fig. 44. Zircon geochronology histogram for the felsic metavolcanic rocks and relative probability plots showing the number of age analyses belonging to each 5 Ma age bracket with a range from 1850 to 2050 Ma. The plots were created using Isoplot 4.15 (Ludwig, 2008) based on $^{207}\text{Pb}/^{206}\text{Pb}$ ages, their 2 sigma errors and only using analyses with <5% discordance.

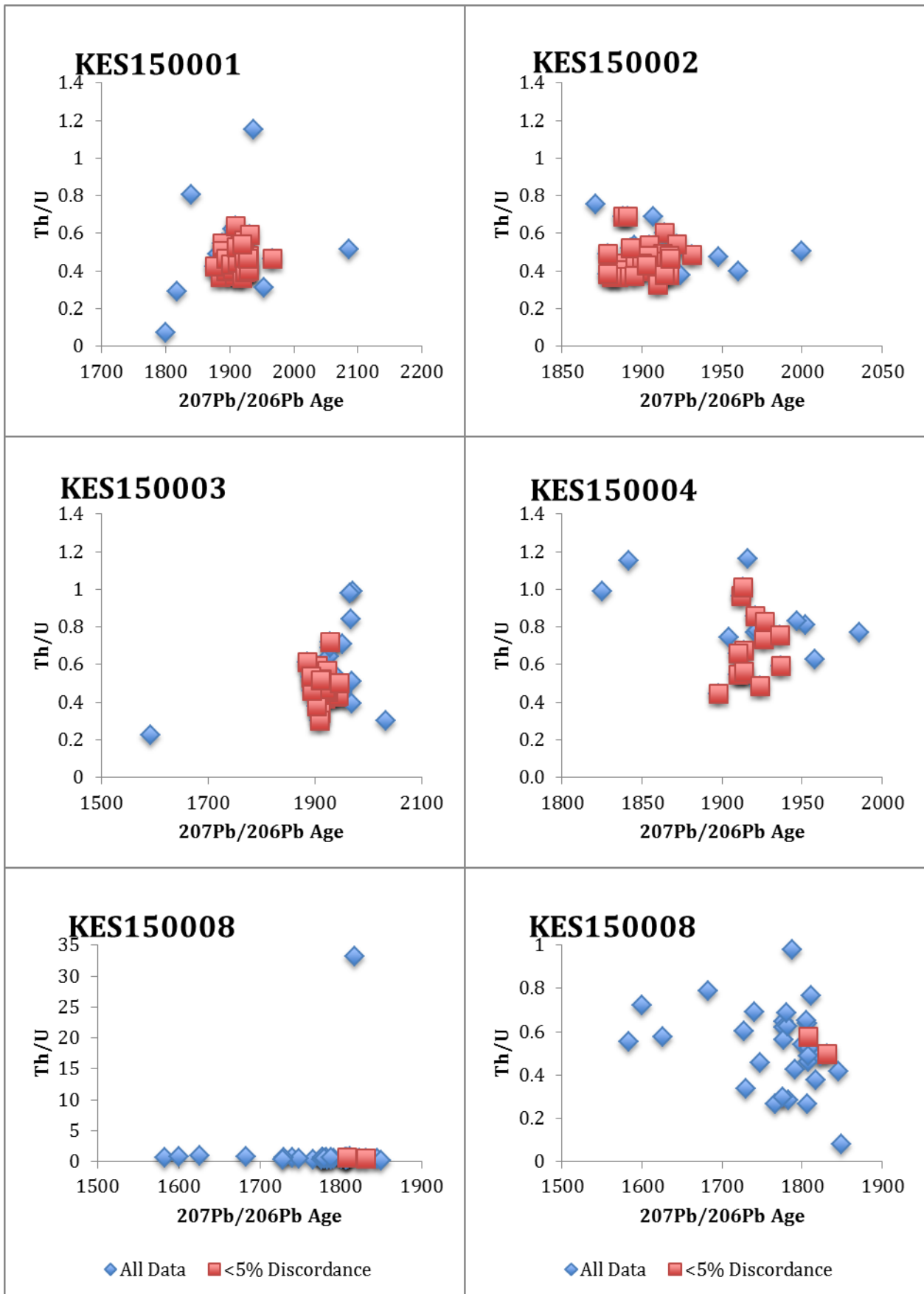


Fig. 45. Plots of Th/U vs. $^{207}\text{Pb}/^{206}\text{Pb}$ Age. One analysis in KES150008 yielded a much higher Th/U ratio than the rest of the analyses. In order to overcome the distortion of the diagram a new plot was made where the single high Th/U analysis was omitted.

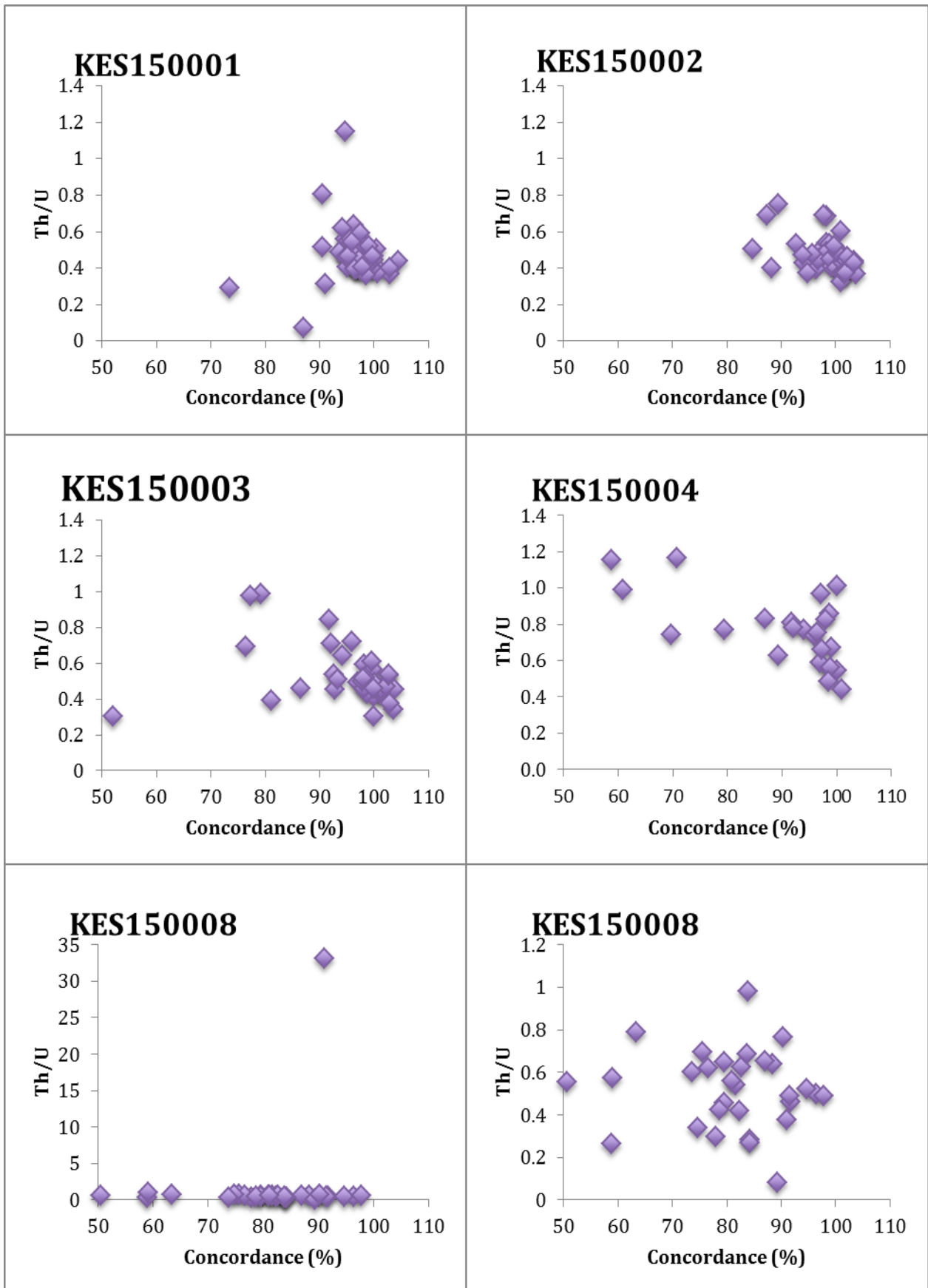


Fig. 46. Th/U vs. concordance. One analysis in KES150008 yielded a much higher Th/U ratio than the rest of the analyses in that population. In order to overcome the distortion of the diagram a new plot was made where the single high Th/U analysis was omitted.

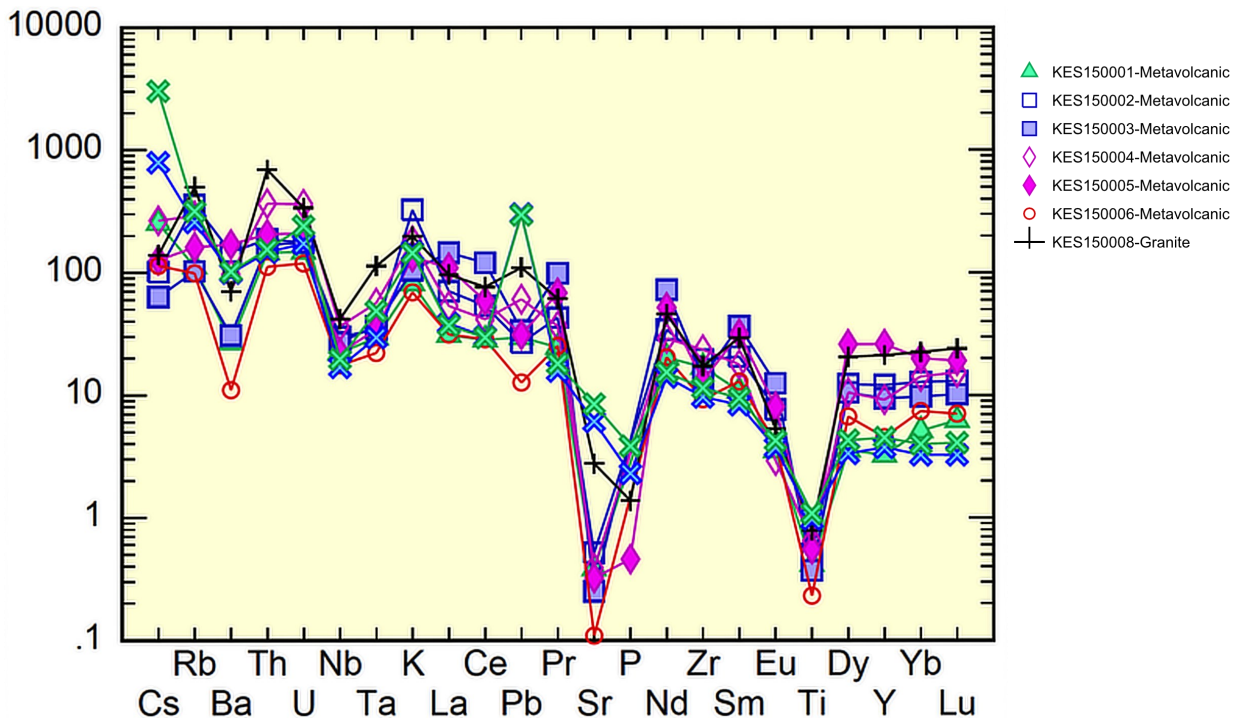


Fig. 47. Primitive mantle normalised plot of metarhyolites and median (blue x) and mean (green x) Andean rhyolites from GEOROC (n=159). Note the on average lower Cs, Pb, Sr, P and Ti concentrations in the Bastnäs samples, while REE contents are subparallel but higher in the Bastnäs samples.

variations that are due to heterogeneity but also changes caused by progressive alteration and it is consequently wiser to use the plots based on Al_2O_3 , Zr and Hf.

6.3 Nature of the alteration process(es)

The whole-rock Na_2O - K_2O - MgO triangular diagram after Hallberg (2003) and Holtstam et al. (2014) shows that the alteration discussed above, to variable degree, led to a redistribution and enrichment or depletion of multiple elements. One example of enrichment is that of K_2O which is also highlighted by the igneous spectrum of Hughes (1973) where all samples except for the least altered KES150004 plot in the K-rich part.

6.4 Geochronology

Zircon U-Pb dating of the felsic metavolcanic rocks yielded dates that span from 1899 ± 4 Ma (MSWD=2.2); 1910 ± 5 Ma (MSWD=3.2); 1911 ± 6 Ma (MSWD=3.2) to 1916 ± 4 Ma (MSWD=1.4). These ages can be compared with similar ages of felsic metavolcanic rocks from the Svecofennian volcanic and subvolcanic suite of intrusive rocks from different locations in Bergslagen (Fig. 50, 51; table 3; Stephens et al. 2009 and references therein). It should be noted that a majority of the ages from Stephens et al. (2009, and references therein) are younger than 1900 Ma, which only holds true for one out of four ages in this thesis. The older ages in this study suggests that at

least some felsic metavolcanic rocks in the REE-line are slightly older than previously documented in this part of Bergslagen, and that magmatism might either have formed a continuum or was episodic between 1920 to 1876 Ma. One of the ages in the data from Stephens et al. (2009) is significantly younger than the rest (Fig. 50). The authors note that the zircons in that fraction might very well be of a younger generation than the other crystals found in the same sample.

The zircon dates in this study are interpreted as igneous crystallization ages. The MSWD-values (2.2; 3.2; 3.2 and 1.4, respectively) are a bit high for the first three. This slight excess scatter could either be due to underestimated analytical error or some kind of geological disturbance, occurring after igneous crystallization. Given the extensive hydrothermal alteration seen in these rocks, a geological explanation is plausible. The igneous origin is supported by, in general, relatively high Th/U values (>0.2). Analyses indicating younger dates than those presented above generally plot discordant. Discordance patterns are similar to those seen during both episodic Pb-loss and recent Pb-loss, likely the result of mixing between metamorphic and igneous domains in the zircons and Pb-loss during metamorphism/metamictization, respectively.

The analyses of the felsic metavolcanic rocks may be correlated with the episode of subduction zone hinge-line retreat suggested by Hermansson (2008) during 1.91-1.89 Ga, which caused back-arc extension and bimodal volcanism (in agreement with Allen et al.

1996). The dates from this study can be considered as maximum ages, both for the volcanism of this episode as well as for the REE mineralization that the felsic metavolcanic rocks are hosting. In addition to this, some of the zircon analyses are indicative of the existence of pre-1.91 Ga crust, something that is also noted from other areas of the Bergslagen region (e.g. Stephens et al. 2009 and references within). It has been suggested that pre-1.91 Ga material is related to juvenile volcanic-arc crust, formed at approximately 2.1-1.9 Ga, which probably made up a continental basement to the Bergslagen region (e.g. Lahtinen & Huhma 1997 and references therein; Rutanen & Andersson 2009; Andersson et al. 2011).

A 1824 ± 7 Ma (MSWD=1.2) date for a population of monazites in one of the felsic metavolcanic rocks may be correlated with the 1822 ± 10 (MSWD=1.7) zircon date of the single granite (Fig. 51). The analysis of the granite is far from perfect and the date should be used with a degree of caution. Almost all the grains in the granite population plot discordantly. The discordance patterns indicate episodic Pb-loss, likely caused either by metamorphism or low-T processes (e.g. Harley et al. 2007). The sometimes extreme U-values indicate that many of the zircons are susceptible to metamictisation. The 1824 ± 7 Ma (MSWD=1.2) date of the monazites is statistically good with a low MSWD value. The fact that the monazites yield a date that is significantly younger than those of the zircons in the metavolcanic rocks might have several plausible explanations, which will be discussed in this and the following sections. Monazite is a mineral well-known for its ability to consist of different age domains, a fact that complicates the analytical work and increases the risk of obtaining a mixing age. This problem is generally avoided by utilizing textural control- and spot dating methods, like in this thesis. It is, however, always possible that the dates are affected by some degree of mixing (this is also true for the zircon analyses).

The dates from the granite and the monazites are within error of each other and this may suggest that the monazites found in the metavolcanic rocks, at least locally, crystallized or recrystallized synchronous with emplacement and crystallization of the granite intrusion. These two dates may be related to the presumed late Svecofokarelian phase (c. 1.85-1.78 Ga) of regional metamorphism and ductile deformation favored by e.g. Andersson (1997); Stephens et al. (2009). It is also possible that the crystallization of monazite is primarily linked to the regional metamorphism and only secondarily to the granite.

The actual REE mineralization, found as horizons in the metavolcanic rocks, has been ascribed to synvolcanic interaction between hydrothermal fluids and pre-existing limestone (e.g. Sahlström et al. 2014; Holtstam & Andersson 2014; Jonsson & Högdahl 2013; Holtstam & Andersson 2007) and it would be interesting to investigate if monazites in the REE mineralization yield the same dates as monazites in the host rock. Holtstam et al. (2014) proposes that the REE mineralization formed due to originally magmatic fluids and later fluids driven by plutonic activity deeper in the newly formed crust. Further analyses of monazites in both the host rocks and

within the REE-mineralization could likely give more information about how and when the mineralization formed.

Differences in age between monazites and zircons is a feature noticed also by several authors in earlier studies (e.g. Rubatto et al. 2001; Zeh et al. 2003; McFarlane et al. 2006; Kelsey et al. 2008; Högdahl et al. 2012) and it has been ascribed to melt-bearing rocks having LREE supersaturation, governed by processes not involving dissolution of monazite already in place; indicated by precipitation of monazite, before/together/after zircon (Högdahl et al. 2012). Since this monazite date is the first of its kind within the host rocks of the REE-line, it needs to be reinforced by additional datings before further, more deep-going and reliable conclusions can be made.

The dates of monazites and zircons in the metavolcanic rocks in this study may be compared with dates of minerals from within the REE-mineralization in three previous studies: (1) uraninite datings from Welin (1963, 1980) giving a 1760 Ma date; (2) uraninite datings from Sahlström (2014) ranging from 1623 to 1898 Ma and (3) Sm-Nd on five different REE-minerals yielding a 1875 ± 110 Ma (MSWD=0.79) date and Re-Os on molybdenite, which occurs as part of sulfides interstitial with the REE-minerals, obtained from three deposits, giving dates of 1842 ± 4 Ma, 1863 ± 4 Ma and 1904 ± 6 Ma from Holtstam et al. (2014). The uraninite data from both Welin (1963, 1980) and Sahlström (2014) indicates open-system behavior and it is thus hard to interpret which of all the dates that is the most geologically significant. The oldest date of Sahlström (2014) is 1898 Ma, which is probably a maximum age. The Sm-Nd date of Holtstam et al. (2014) has a too large uncertainty associated with it to be used in a more precise interpretation. The Re-Os dates (Holtstam et al. 2014) have lower uncertainties but then there is always the risk of mixing between different age domains within the molybdenite that needs to be kept in mind. Re-Os crystallization ages from Holtstam et al. (2014) combined with the presumed maximum age of Sahlström (2014) are all older than the monazite and granite crystallization ages and in line with or younger than the crystallization ages of the metavolcanic rocks investigated in this study.

6.5 Key issues for future work

The extent of this study has been limited by time constraints and budget. More analyses are needed in order to get a deeper understanding of the geochronological relations between felsic metavolcanic host rocks and the REE-mineralizations within the REE line. The mineralization itself is diverse and by dating different REE-minerals from the same locality it can be assessed whether or not the minerals formed simultaneously or during different episodes. It would also be interesting to try to date zircon and monazite from the same locality (this was never possible in this study). Further studies would also be able to either reinforce or weaken the dates of the granite and monazite, leading to statistically more robust data.

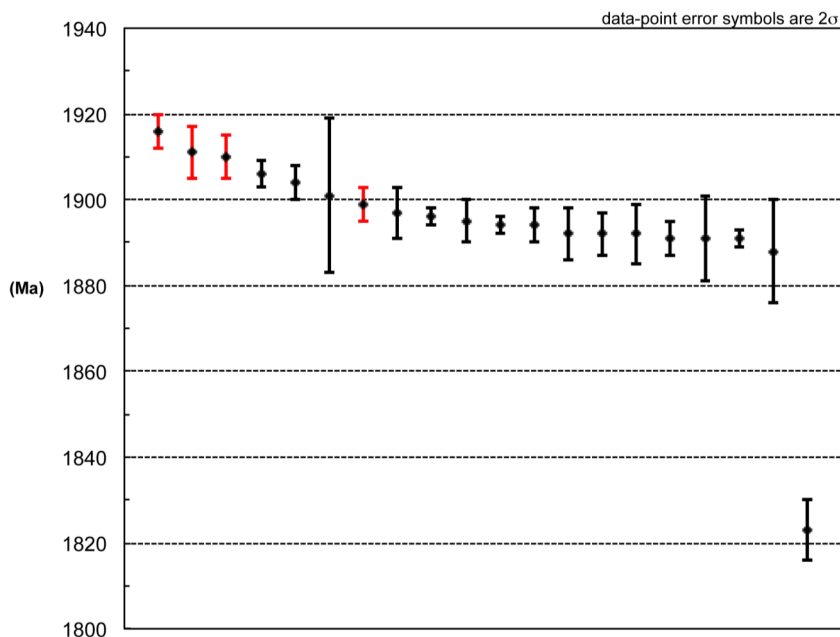


Fig. 50. Ages of metavolcanic rocks (Svecofennian volcanic and subvolcanic intrusive rocks) in the Bergslagen region from Stephens et al. and references therein (2009) and this study (red error bars).

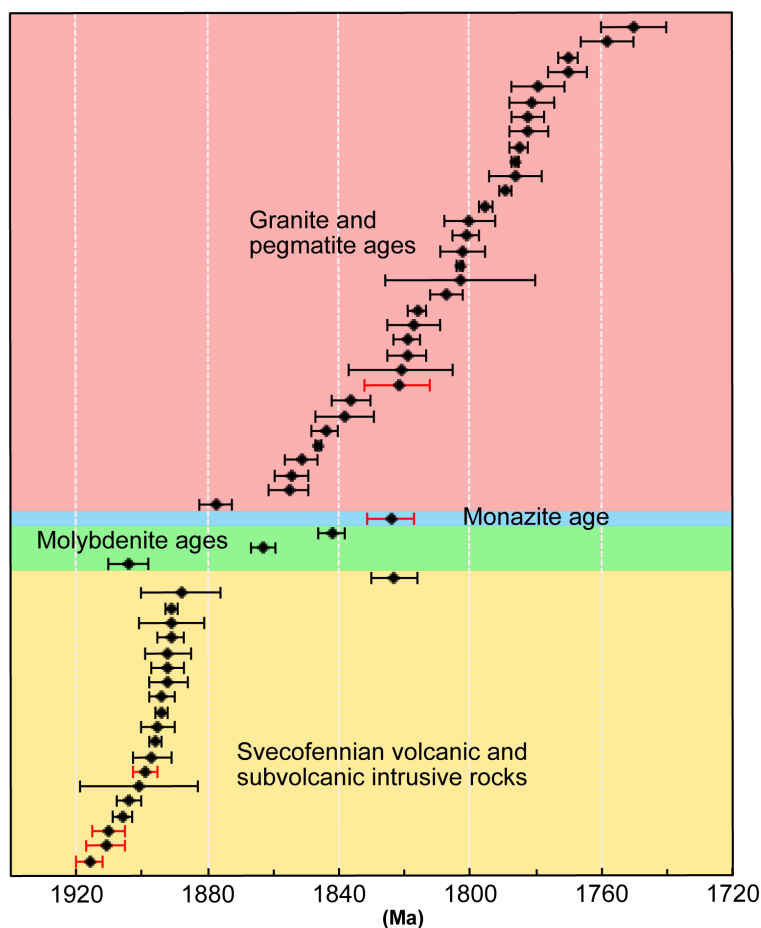


Fig. 51. Comparison of ages from the metavolcanic rocks (Svecofennian volcanic and subvolcanic intrusive rocks; Stephens et al. 2009 and references therein) together with molybdenite ages (Holtstam et al. 2014) and the monazite age as well as granite and pegmatite ages (Stephens et al. 2009 and references therein). Dates with red error bars are from this study. It should be noted that ages are reported in different formats, some are e.g. $^{207}\text{Pb}/^{206}\text{Pb}$ weighted average ages while others are upper intercept ages (UI). Modified from Stephens et al. 2009.

7 Conclusions

- ◆ The felsic metavolcanic rocks hosting the REE-mineralizations are mostly consisting of a variably altered rhyolite precursor.
- ◆ Whole rock chemistry data and isocon analyses indicate that few of the geochemical signals in the felsic metavolcanic rocks are of primary, igneous, origin and that geochemical differences among the samples are not the result of fractional crystallization processes.
- ◆ Variable degree of alteration led to redistribution and enrichment of SiO₂; MgO; K₂O; Co; Eu and Fe₂O₃ and depletion of Pb; Ni; Zn; Na₂O; CaO; Th and U.
- ◆ Isocon analyses indicate significant mass gain in all the metavolcanic samples, ranging from +27% to 139%
- ◆ REE patterns are similar to those presented by numerous authors for the Svecofennian volcanic and subvolcanic suite of intrusive rocks (1.91-1.89 Ga) and as stated by earlier workers comparable with those found in a normal to mature, active continental margin.
- ◆ The geochronological data from four localities with felsic metavolcanic rocks within this part of the REE-line give dates of: 1910 ± 5 Ma (MSWD=3.2); 1899 ± 4 Ma (MSWD=2.2); 1911 ± 6 Ma (MSWD=3.2) and 1916 ± 4 Ma (MSWD=1.4).
- ◆ The ages are interpreted as igneous crystallization ages and indicate that several localities with felsic metavolcanic rocks in the REE-line are older than in Bergslagen as whole.
- ◆ The dates from this study combined with presently available geochronology data for metavolcanic rocks in Bergslagen suggests that magmatism might either have formed a continuum or was episodic between 1920 to 1876 Ma.
- ◆ A 1824 ± 7 Ma (MSWD=1.2) date for a population of the REE-phosphate mineral monazite in one of the felsic metavolcanic rocks can be correlated with a population of strongly discordant zircons, yielding a 1822 ± 10 (MSWD=1.7) date of the single granite that was dated.
- ◆ The monazite and granite dates are overlapping, suggesting that at least part of the monazites in the felsic metavolcanic rocks either crystallized or recrystallized during the presumed late Svecofennian phase (c. 1.85-1.78 Ga) of regional metamorphism and ductile deformation and like-

ly due to heat and fluids from emplacement and crystallization of the granite intrusion.

- ◆ Further studies are required in order to either reinforce or weaken the dates of the granite and monazite, leading to statistically more robust data.

8 Acknowledgements

This work would not have been possible without the support, constructive feedback and help of so many. Thank you all! I am most grateful to my two supervisors: Anders Scherstén from the Department of Geology at Lund University (LU) and Erik Jonsson from the Geological Survey of Sweden (SGU) for helping me set up and finish the great endeavour that this project has come to be.

My most sincere and humble thanks to: Tomas Næraa (LU) for helping me run the LA-ICP-MS analyses and the subsequent data reduction; Andreas Petersson, Leif Johansson, Ulf Söderlund and Ashley Gumsley (LU) for helping me with both practical and theoretical problems and the staff at the Geo Library (LU) for assistance in finding all the great articles and books I have used.

Last but not least I would like to thank my fellow student Andreas Olsson for our fruitful discussions as well as my other friends and especially my family for all their wholehearted support and help during this entire process. Thank you for putting up with my early mornings, long working days and late evenings. Without your help this project would still remain unfinished...

The Department of Geology (LU) and the geological survey of Sweden (SGU) are thanked for their financial support.

9 References

- Andersson, U.B., 1997: The late Svecofennian, high grade contact and regional metamorphism in southwestern Bergslagen (central southern Sweden). Final report 970519, *SGU project 03-819/93*, 36 pp., (unpublished).
- Andersson, U.B. (ed.), 2004: The Bastnäs-type REE-mineralisations in north-western Bergslagen, Sweden. *SGU Rapport & Meddelanden 119*, 1-36.
- Andersson, U.B., Högdahl, K., Sjöström, H., Bergman, S., 2006: Multistage growth and reworking of the Palaeoproterozoic crust in the Bergslagen area, southern Sweden: evidence from U-Pb geochronology. *Geological Magazine 143*, 679-697.
- Andersson, U.B., Begg, G.C., Griffin, W.L., Högdahl, K., 2011: Ancient and juvenile components in the continental crust and mantle: Hf isotopes in zircon from Svecofennian magmatic rocks and rapakivi granites in Sweden. *Lithosphere 6*, 409-419.
- Babcock, R.S., 1973: Computational models of metasomatic processes. *Lithos 6*, 279-290.
- Barrell, J., 1917: Rhythms and the measurement of

- geologic time. *Bulletin of the Geological Society of America* 18, 745-904.
- Bateman, H., 1910: Solution of a system of differential equations occurring in the theory of radioactive transformations. *Proceedings of the Cambridge Philosophical Society* 15, 423-427.
- Bayliss, P., Levinson, A.A., 1988: A system of nomenclature for rare-earth mineral species: revision and extension. *American Mineralogist* 73, 422-423.
- Beunk, F.F., Kuipers, G., 2012: The Bergslagen ore province, Sweden: review and update of an accreted oroclinal, 1.9-1.8 Ga BP. *Precambrian Research* 216-219, 95-119.
- Binnemans, K., Jones, P.T., Blanpain, B., Van Gerven, T., Yang, Y., Walton, A., Buchert, M., 2013: Recycling of rare earths: a critical review. *Journal of Cleaner Production* 51, 1-22.
- Bogdanova, S., Gorbatshev, R., Skridlaite, G., Soesoo, G., Taran, L., Kurlovich, D., 2015: Trans-Baltic Palaeoproterozoic correlations towards the reconstruction of supercontinent Columbia/Nuna. *Precambrian Research* 259, 5-33.
- Boynton, W.V., 1984: Cosmochemistry of rare earth elements: meteorite studies. In P. Hendersen (ed.): *Rare earth element geochemistry*, 63-114. Elsevier, Amsterdam.
- Brown, G.C., Thorpe, R.S., Webb, P.C., 1984: The geochemical characteristics of granitoids in contrasting arcs and comments on magma sources. *Journal of the Geological Society of London* 141, 413-426.
- Bruker Aurora M90 ICP-MS Product Brochure from 01-2013. From: https://www.bruker.com/fileadmin/user_upload/8-PDF-Docs/Separations_MassSpectrometry/Literature/Brochures/1815831_aurora_ICP-MS_Brochure_01-2013_eBook.pdf
Accessed on: 2015-10-15.
- Corfu, F., Hanchar, J.M., Hoskin, P.W.O., Kinny, P., 2003: Atlas of Zircon Textures. In J.M. Hanchar & P.W.O Hoskin (eds.): *Zircon*, 469-500. Reviews in Mineralogy and Geochemistry 53.
- Cottle, J.M., Horstwood, M.S.A., Parrish, R.R., 2009a: A new approach to single shot laser ablation analysis and its application to U/Pb geochronology. *Journal of Analytical Atomic Spectrometry* 24, 1355-1363.
- Cottle, J.M., Searle, M.P., Horstwood, M.S.A., Waters, D.J., 2009b: Timing of midcrustal metamorphism, melting, and deformation in the Mount Everest Region of Southern Tibet revealed by U-Th-Pb geochronology. *Journal of Geology* 117, 643-664.
- Du, X., Graedel, T.E., 2011: Uncovering the global life cycles of the rare earth elements. *Scientific Reports* 1, 145.
- Egerton, R.F., 2005: *Physical principles of electron microscopy: An introduction to TEM, SEM, and AEM*. Springer, New York. 202 pp.
- Faure, G., Mensing, T.M., 2005: *Principles of isotope geology*, 3rd edition. John Wiley & Sons, Hoboken. 589 pp.
- Feng, R., Machado, N., Ludden, J., 1993: Lead geochronology of zircon by LaserProbe-inductively coupled plasma mass spectrometry (LP-ICPMS). *Geochimica et Cosmochimica Acta* 57: 3479-3486.
- Finch, R.J., Hanchar, J.M., 2003: Structure and chemistry of zircon and zircon-group minerals. In J.M Hanchar & P.W.P Hoskin (eds.): *Zircon*, 1-25. Reviews in Mineralogy and Geochemistry 53.
- Finlow-Bates, T., Stumpfl, E.F., 1981: The behavior of the so-called immobile elements in hydrothermally altered rocks associated with volcanogenic submarine-exhalative ore deposits. *Mineralium Deposita* 16, 319-328.
- Frei, D., Gerdes, A., 2009: Precise and accurate in situ U-Pb dating of zircon with high sample throughput by automated LA-SF-ICP-MS. *Chemical Geology* 261, 261-270.
- Fryer, B.J., Jackson, S.E., Longerich, H.P., 1993: The application of laser ablation microprobe-inductively coupled plasma-mass spectrometry (LAM- ICP-MS) to in situ U-Pb geochronology. *Chemical Geology* 109, 1-8.
- Gaál, G., Gorbatshev, R., 1987: An outline of the Precambrian evolution of the Baltic shield. *Precambrian Research* 35, 15-52.
- Grant, J.A., 1986: The isocon diagram – a simple solution to Gresens' equation for metasomatic alteration. *Economic Geology* 81, 1978-1982.
- Grant, J.A., 2005: Isocon analysis: a brief review of the method and applications. *Physics and Chemistry of the Earth* 30, 997-1004.
- Geijer, P., 1961: The geological significance of the cerium mineral occurrences of the Bastnäs type in central Sweden. *Arkiv för Mineralogi och Geologi* 3, 99-105.
- Geijer, P., Carlborg, H., 1923: *Riddarhytte malmfält i Skinnskattebergs socken, Västmanlands län. Kungliga Kommerskollegium, Beskrivningar över mineralfyndigheter* 1, 1-343.
- Geijer, P., Magnusson, N.H., 1944: De mellansvenska järnmalmernas geologi, *SGU Ca* 35, 1-654.
- Goodenough, K.M., Schilling, J., Jonsson, E., Kalvig, P., Charles, N., Tuduri, J., E.A. Deady., Sadeghi, M., Schiellerup, H., Müller, A., Bertrand, G., Arvanitidis, N., Eliopoulos, D.G., Shaw, R.A., Thrane, K., Keulen, N., 2016: Europe's rare earth element resource potential: an overview of REE metallogenetic provinces and their geodynamic setting. *Ore Geology Reviews* 72, 838-856.
- Gorbatshev, R., Bogdanova, S., 1993: Frontiers in the Baltic Shield. In R. Gorbatshev (ed.), The Baltic Shield. Special volume. *Precambrian Research* 64, 3-21.
- Gresens, R.L., 1967: Composition-volume relationships of metasomatism. *Chemical Geology* 2, 47-65.

- Guillong M., Horn I., and Günther, D., 2003: A comparison of 266 nm, 213 nm and 193 nm produced from a single solid state Nd:YAG laser for laser ablation ICP-MS. *Journal of Analytical Atomic Spectrometry* 18, 1224-1230.
- Guyonnet, D., Planchon, M., Rollat, A., Escalon, V., Tuduri, J., Charles, N., Vaxelaire, S., Dubois, D., Fargier, H., 2015: Material flow analysis applied to rare earth elements in Europe. *Journal of Cleaner Production* 107, 215-228.
- Hallberg, A., 2003: Styles of hydrothermal alteration and accompanying chemical changes in the Sängen formation, Bergslagen, Sweden, and adjacent areas. Economic geology research and documentation 2, 2001-2002. *SGU Rapport & Meddelanden* 113, 4-35.
- Harley, S. L., Kelly, N. M., Möller, A., 2007: Zircon behaviour and the thermal histories of mountain chains. *Elements* 3, 25-30.
- Hermansson, T., Stephens, M.B., Corfu, F., Page, L.M., Andersson, J., 2008: Migratory tectonic switching, western Svecofennian orogeny, central Sweden, Constraints from U/Pb zircon and titanite geochronology. *Precambrian Research* 161, 250-278.
- Hirata, T., Nesbitt, R.W., 1995: U-Pb isotope geochronology of zircon: Evaluation of the laser probe-inductively coupled plasma mass spectrometry technique. *Geochimica et Cosmochimica Acta* 59, 2491-2500.
- Hisinger, W., Berzelius, J.J., 1804: *Cerium, en ny metall, funnen i Bastnäs Tungsten, från Riddarhyttan i Westmanland*. Henrik A Nordström förlag, Stockholm. 1-24.
- Hodges, K.V., 2003: Geochronology and Thermochronology in Orogenic systems, In R.L. Rudnick (ed.): *The Crust, Treatise on geochemistry* 3, 263-292. Elsevier, Oxford.
- Holmes, A., 1911: The association of lead with uranium in rock-minerals and its application to the measurement of geological time. *Proceedings of the Royal Society of London* 85, 248-256.
- Holmes, A., 1946: An estimate of the age of the Earth. *Nature* 157, 680-684.
- Holtstam, D., Andersson, U.B., 2007: The REE minerals of the Bastnäs-type deposits, south-central Sweden. *Canadian Mineralogist* 45, 1073-1114.
- Holtstam, D., Andersson, U.B., Broman, C., Mansfeld, J., 2014: Origin of REE mineralization in the Bastnäs-type Fe-REE-(Cu-Mo-Bi-Au) deposits, Bergslagen, Sweden. *Mineralium Deposita* 49, 933-966.
- Houtermans, F.G., 1946: Die Isotopenhäufigkeiten im natürlichen Blei und das Alter des Urans. *Naturwissenschaften* 33, 185-186.
- Hughes, C.J., 1973: Spilites, keratophyres and the igneous spectrum. *Geological Magazine* 109, 513-527.
- Humphries, M., 2013: Rare Earth Elements: The Global Supply Chain. *Congressional Research Service*, 1-27.
- Högdahl, K., Andersson, U.B., Eklund, O., (eds.) 2004: The Transscandinavian Igneous Belt: a review of its character and evolution. *Geological Survey of Finland, Special Paper* 37. 125 pp.
- Högdahl, K., Sjöström, H., Bergman, S., 2009: Ductile Shear zones related to crustal shortening and domain boundary evolution in the central Fennoscandian Shield. *Tectonics* 28, 1-18.
- Högdahl, K., Majka, J., Sjöström, H., Persson Nilsson, K., Claesson, S., Konečný, P., 2012: Reactive monazite and robust zircon growth in diatexites and leucogranites from a hot, slowly cooled orogen: implications for the Palaeoproterozoic tectonic evolution of the central Fennoscandian Shield, Sweden. *Contributions to Mineralogy and Petrology* 163, 167-188.
- Ihre, P., Sädbom S., 1986: *Riddarhytte malmfält. Prospekteringsarbeten 1986. Sveriges Geologiska AB*. Unpublished prospecting report, Division prospektering PRAP 86541. 261 pp.
- Irvine, T.N., Baragar, W.R.A., 1971: A guide to the chemical classification of the common volcanic rocks. *Canadian Journal of Earth Sciences* 8, 523-548.
- Jaffey, A.H., Flynn, K.F., Glendenin, L.F., Bentley, W.C., Essling, A. M., 1971: Precision measurements of half-lives and specific activities of ^{235}U and ^{238}U . *Physical Review C* 4, 1889-1906.
- Jansson, N.F., 2011: *The origin of iron ores in Bergslagen, Sweden, and their relationships with polymetallic sulphide ores*. PhD thesis. Luleå University of Technology. 73 pp.
- Jonsson, E., Billström, K., 2009: Lead isotope systematics in the Långban deposit and adjacent sulphide mineralisations in western Bergslagen, Sweden. *GFF* 131, 215-227.
- Jonsson, E., Högdahl, K., 2013: New evidence for the timing of formation of Bastnäs-type REE mineralisation in Bergslagen, Sweden. *12th SGA Biennial Meeting. Mineral Deposit Research for a high-tech world*. Sweden, 2013. Proceedings 4.
- Jonsson, E., Högdahl, K., Sahlström, F., Nysten, P., Sadeghi, M., 2014: The Palaeoproterozoic skarn-hosted REE mineralisations of Bastnäs-type: overview and mineralogical – geological character. *ERES2014: 1st European Rare Earth Resource Conference, Milos 4-7 September 2014*.
- Kelsey, D. E., Clark, C., Hand, M., 2008: *Thermobarometric modelling of zircon and monazite growth in melt-bearing systems: Examples using model metapelitic and metapsammittic granulites*. 2 ed., Blackwell Publishing Inc. 199-212 pp.
- Košler, J., Sylvester, P.J., 2003: Present trends and the future of zircon in geochronology: Laser Ablation ICPMS. In J.M. Hanchar & P.W.O Hoskin (eds.): *Zircon*, 243-271. *Reviews in Mineralogy and Geochemistry* 53.

- Kumpulainen, R.A., Mansfeld, J., Sundblad, K., Neymark, L., Bergman, T., 1996: Stratigraphy, age and Sm-Nd isotope systematics of the country rocks to Zn-Pb sulphide deposits, Ämmeberg district, Sweden. *Economic Geology* 91, 1009-1021.
- Lahtinen, R., Huhma, H., 1997: Isotopic and geochemical constraints on the evolution of the 1.93-1.79 Ga Svecofennian crust and mantle in Finland. *Precambrian Research* 82, 13-34.
- Lahtinen, R., Korja, A., Nironen, M., 2005: Palaeoproterozoic tectonic evolution. In M. Lehtinen, P.A. Nurmi and O.T. Rämö (eds.): *Precambrian Geology of Finland: Key to the Evolution of the Fennoscandian Shield*, 481-532. Elsevier, New York.
- Lahtinen, R., Garde, A.A., Melezhik, V.A., 2008: Paleoproterozoic evolution of Fennoscandia and Greenland. *Episodes* 31, 20-28.
- Lahtinen, R., Johnston, S.T., Nironen, M., 2014: The Bothnian coupled oroclines of the Svecofennian Orogen: a Palaeoproterozoic terrane wreck. *Terra Nova* 26, 330-335.
- Lee, J. K.W., Williams, I.S., Ellis, D.J., 1997: Pb, U and Th diffusion in natural zircon. *Nature* 390, 159-163.
- Le Bas, M.J., Le Maitre, R.W., Steckeisen, A., Zanetti, B., 1986: A chemical classification of volcanic rocks based on the total alkali-silica diagram. *Journal of Petrology* 27, 745-750.
- Le Roux, J. L., Glendenin, L.E., 1963: Half-life of ²³²Th, *Proceedings of the National Meeting on Nuclear Energy*, 83-94. Pretoria, South Africa, April 1963.
- Ludwig, K.R., 1998: On the treatment of concordant uranium-lead ages. *Geochimica et Cosmochimica Acta* 62, 665-676.
- Ludwig, K.R., 2008: Isoplot 3.70. A geochronological toolkit for Microsoft Excel. *Berkeley Geochronology Center Special Publications* 4.
- Lundqvist, T., Vaasjoki, M., Persson, P.-O., 1998: U-Pb ages of plutonic and volcanic rocks in the Svecofennian Bothnian Basin, Central Sweden, and their implications for the Palaeoproterozoic evolution of the Basin. *GFF* 120, 357-363.
- Lundström, I., Allen, R.L., Persson, P.-O., Ripa, M., 1998: Stratigraphies and depositional ages of Svecofennian, Paleoproterozoic metavolcanic rocks in E. Svealand and Bergslagen, south central Sweden. *GFF* 120, 315-320.
- MacLean, W.H., Kranidiotis, P., 1987: Immobile elements as monitors of mass transfer in hydrothermal alteration: Phelps massive sulphide deposit, Matagami, Quebec. *Economic Geology* 82, 951-962.
- MacLean, W.H., 1988: Rare earth element mobility at constant inter-REE ratios in the alteration zone at the Phelps Dodge massive sulfide deposit, Matagami, Quebec. *Mineralium Deposita* 23, 231-238.
- MacLean, W.H., 1990: Mass changes in altered rock series. *Mineralium Deposita* 25, 44-49.
- MacLean, W.H., Barrett, T.J., 1993: Lithogeochemical techniques using immobile elements. *Journal of Geochemical Exploration* 48, 109-133.
- McDonough, W.F., Sun, S.S., Ringwood, A.E., Jagoutz, E., Hoffman, A.W., 1992: Potassium, rubidium and cesium in the Earth and Moon and the evolution of the mantle of the Earth. *Geochimica et Cosmochimica Acta* 56, 1001-1012.
- Mcfarlane, C. R. M., Connelly, J. N., Carlson, W. D., 2006: Contrasting response of monazite and zircon to a high-T thermal overprint. *Lithos* 88, 135-149.
- Nironen, M., 1997: The Svecofennian Orogen: a tectonic model. *Precambrian Research* 86, 21-44.
- Ohta, T., Hiroyoshi, A., 2007: Statistical empirical index of chemical weathering in igneous rocks: A new tool for evaluating the degree of weathering. *Chemical Geology* 240, 280-297.
- Rubatto, D., Williams, S. I., Buick, S. I., 2001: Zircon and monazite response to prograde metamorphism in the Reynolds Range, central Australia. *Contributions to Mineralogy and Petrology* 140, 458-468.
- Rutanen, H., Andersson, U.B., 2009: Mafic plutonic rocks in a continental-arc setting: geochemistry of 1.87-1.78 rocks from south-central Sweden and models of their palaeotectonic setting. *Geological Journal* 44, 241-279.
- Sahlström, F., 2014: *Stable isotope systematics of skarn-hosted REE-silicate – magnetite mineralizations in central Bergslagen, Sweden*. Master's thesis, department of Earth Sciences, Uppsala University.
- Sahlström, F., Jonsson, E., Högdahl, K., Harris, C., 2014: Magnetite oxygen isotope constraints on the genesis of Bastnäs-type REE mineralization in Bergslagen, Sweden. In M.D. Johnson (ed.): *31st Nordic Geological Winter Meeting, abstract volume*. 60 pp.
- Sahlström, F., Jonsson, E., Högdahl, K., Harris, C., Troll, V.R., Jolis, E.M., 2015: O and C isotope study of Bastnäs-type rare earth element mineralization, Bergslagen, Sweden. *PACRIM 2015 congress, Hong Kong, China 18-21 March 2015*.
- Schoene, B., 2014: U-Th-Pb Geochronology, In H.D. Holland & K.K. Turekian (eds.): *Treatise on Geochemistry* 4, 341-378. Elsevier, Oxford.
- Searle, M.P., Noble, S.R., Cottle, J.M., Waters, D.J., Mitchell, A.H.G., Hlaing, T., Horstwood, M.S.A., 2007: Tectonic evolution of the Mogok metamorphic belt, Burma (Myanmar) constrained by the U-Th-Pb dating of metamorphic and magmatic rocks. *Tectonics* 26, 1-24.
- Soddy, F., 1913: Intra-atomic charge. *Nature* 92, 399-400.
- Stephens, M.B., Ripa, M., Lundström, I., Persson, L., Bergman, T., Ahl, M., Wahlgren, C.-H., Persson, P.-O., Wickström, L., 2009: Synthesis of bedrock geology in the Bergslagen region, Fennoscandian Shield, south-central Sweden. *SGU Ba* 58, 1-259.
- Strömberg, A., 1980: Berggrundsgeologiska kartan 12

- F Ludvika SO (bed rock map). *SGU, Serie Af 128*.
- Söderlund, U., Johansson, L., 2002: A simple way to extract baddeleyite (ZrO₂). *Geochemistry, Geophysics, Geosystems* 3, 1-7.
- Taylor, S.R., McLennan, V.R., 1985: *The continental crust: its composition and evolution*. Blackwell Scientific Publications, Oxford. 312 pp.
- Taylor, S.R., Rudnick, R.L., McLennan, S.M., Eriksson, K.A., 1986: Rare earth element patterns in Archean high-grade metasediments and their tectonic significance. *Geochimica et Cosmochimica Acta* 50, 2267-2279.
- Tegengren, FR., 1924: Sveriges ädlare malmer och bergverk. *SGU Ca 17*, 1-406.
- Tera, F., Wasserburg G.J., 1972a: U-Th-Pb systematics in lunar highland samples from the Luna 20 and Apollo 16 missions. *Earth and Planetary Science Letters* 17, 36-51.
- Tera, F., Wasserburg G.J., 1972b: U-Th-Pb systematics in three Apollo 14 basalts and the problem of initial Pb in lunar rocks. *Earth and Planetary Science Letters* 14, 281-304.
- Trägårdh, J. 1988: Cordierite-mica-quartz schists in a Proterozoic volcanic iron ore-bearing terrain, Rid darhyttan area, Bergslagen, Sweden. *Geologie en Mijnbouw* 67, 397-409.
- Trägårdh, J. 1991: Metamorphism of magnesium-altered felsic volcanic rocks from Bergslagen, central Sweden. A transition from Mg-chlorite- to cordierite-rich rocks. *Ore Geology Reviews* 6, 485-497.
- Villeneuve, M., Sanderman, H.A., Davis, W.J., 2000: A method for intercalibration of U-Th-Pb and ⁴⁰Ar-³⁹Ar ages in the Phanerozoic. *Geochimica et Cosmochimica Acta* 64, 4017-4030.
- Welin, E., 1963: The interpretation of discordant U/Pb age data from central Sweden. *GFF* 85, 223-235.
- Welin, E., 1980: Tabulation of recalculated radiometric ages published 1960-1979 for rocks and minerals in Sweden. *GFF* 101, 309-320.
- Welin, E., 1987: The depositional evolution of the Svecofennian supracrustal sequence in Finland and Sweden. *Precambrian Research* 35, 95-113.
- Wendt, I., 1984: A three-dimensional U/Pb discordia plane to evaluate samples with common lead of unknown isotopic composition. *Chemical Geology* 46, 1-12.
- Wetherill, G.W., 1956: Discordant uranium-lead ages. *Transactions of the American Geophysical Union* 37, 320-326.
- Williams, M.L., Jercinovic, M.J., Hetherington, J.C., 2007: Microprobe monazite geochronology: understanding geologic processes by integrating composition and chronology. *Annual Review of Earth and Planetary Sciences* 35, 137-175.
- Winchester, J.A., Floyd, P.A., 1977: Geochemical discrimination of different magma series and their differentiation products using immobile elements. *Chemical Geology* 20, 325-343.
- U.S. Department of the Interior (DOI), United States Geological Survey (USGS), 2012: *Minerals Yearbook, Rare Earths*.
- U.S. Department of the Interior (DOI), United States Geological Survey (USGS). <http://crustal.usgs.gov/laboratories/icpms/intro.html> Accessed 2015-10-15.
- Zeh, A., Williams, I. S., Braetz, H., Millar I. L., 2003: Different age response of zircon and monazite during tectono-metamorphic evolution of a high grade paragneiss from the Ruhla crystalline complex, central Germany. *Contributions to Mineralogy and Petrology* 145, 691-706.
- www.eurare.eu, accessed on 1/4-2015.
- www.georock.com, accessed on 1/3-2016.
- www.rareelementresources.com, accessed on 18/1-2016.
- www.rockware.com, accessed on 25/2-2016.

Appendix I - Whole Rock Data

Analyte	Unit	Metavolcanic						BIF	Granite
		KES150001	KES150002	KES150003	KES150004	KES150005	KES150006	KES150007	KES150008
SiO2	wt. %	78.43	72.53	77.19	66.98	67.42	84.80	49.14	73.39
Al2O3	wt. %	11.53	13.34	11.29	16.87	11.49	7.39	0.09	13.31
Fe2O3	wt. %	0.86	1.90	3.38	1.52	12.67	1.50	48.96	2.21
MgO	wt. %	4.40	0.71	1.56	2.06	1.13	2.44	0.80	0.48
CaO	wt. %	0.04	0.10	0.04	0.33	0.26	<0.01	0.18	0.39
Na2O	wt. %	0.23	0.32	1.81	5.76	0.93	0.08	<0.01	2.94
K2O	wt. %	2.45	9.78	3.16	5.47	4.04	2.08	<0.01	5.97
TiO2	wt. %	0.09	0.11	0.08	0.14	0.12	0.05	<0.01	0.17
P2O5	wt. %	<0.01	<0.01	<0.01	<0.01	0.01	<0.01	<0.01	0.03
MnO	wt. %	<0.01	0.03	<0.01	0.10	0.05	<0.01	<0.01	0.02
Cr2O3	wt. %	<0.002	<0.002	<0.002	<0.002	<0.002	<0.002	<0.002	<0.002
Ni	PPM	<20	<20	<20	<20	<20	<20	<20	<20
Sc	PPM	4	5	3	7	6	3	2	5
LOI	wt. %	1.7	0.9	1.3	0.6	1.6	1.5	0.6	0.8
Sum	wt. %	99.76	99.76	99.82	99.80	99.70	99.86	99.79	99.77
Ba	PPM	188	1027	215	674	1190	77	<1	490
Be	PPM	1	4	5	7	6	2	3	9
Co	PPM	86.4	45.0	45.1	22.5	41.2	55.5	57.5	69.5
Cs	PPM	2.0	0.8	0.5	2.1	1.0	0.9	<0.1	1.1
Ga	PPM	18.8	21.4	18.9	30.4	18.4	23.4	2.2	17.3
Hf	PPM	6.0	7.3	5.8	9.6	5.5	3.7	<0.1	6.3
Nb	PPM	15.8	21.3	19.2	26.0	15.8	12.5	0.6	29.8
Rb	PPM	71.0	226.7	65.1	184.7	102.3	62.8	0.5	317.0
Sn	PPM	3	4	4	8	5	35	3	14
Sr	PPM	8.1	10.9	5.3	8.2	6.8	2.3	0.9	58.4

Appendix II - LA-ICP-MS Methodology I

LA-ICP-MS U-Th-Pb dating methodology, Department of Geology, Lund University

Laboratory & Sample Preparation	
Laboratory name	LA-ICP-MS Lund University
Sample type / mineral	Zircon
Sample preparation	Conventional mineral separation, 1 inch resin mount, 1 μm polish to finish.
Imaging	BSE-imaging, Hitachi S-4300N, 10 mm working distance.
Laser ablation system	
Make, Model & type	Photon Machines, Analyte G2, excimer laser
Sample holder	HelEx II Active 2-volume
Laser wavelength	193 nm
Pulse width	<4 ns
Fluence	4.39 J/cm ²
Repetition rate	7 Hz
Spot size	25 μm
Sampling mode/pattern	25 μm single spot analyses
Carrier gas	He, Ni
Background collection	20 seconds
Ablation duration	20 seconds
Wash-out delay	7 seconds
Cell carrier gas flow	C 1 l/min
ICP-MS Instrument	
Make, Model & type	Bruker, Aurora, quadropole ICP-MS
Sample introduction	Via conventional tubing
RF power	Approx. 1000-1100 W
Sample gas flow	~1.0 l/min Ar
Detection system	Single collector
Masses measured	202, 206, 207, 208, 232, 238
Integration time per peak	10-30 ms
Total integration time per reading	Approx. 0.1 sec
Sensitivity	4000-7000 cps ²⁰⁷ Pb (GJ1)
Data Processing	
Gas blank	20 second on-peak
Calibration strategy	GJ-1 used as primary reference material, 91500 used as secondary reference material. Ilivertalik granite (2.8 Ga) used as in-house reference material.
Reference Material info	91500: ²⁰⁷ Pb/ ²⁰⁶ Pb Age = 1065 \pm 20 Ma Ilivertalik: ²⁰⁷ Pb/ ²⁰⁶ Pb Age = Approx. 2.80 Ga

Data processing package used	Iolite Software, downhole correction following Paton et al. (2010), DRS: X_U_Pb_Geochron4. Isoplot 4.15 (Ludwig, 2008)
Mass discrimination	Standard-sample bracketing with $^{207}\text{Pb}/^{206}\text{Pb}$ and $^{206}\text{Pb}/^{238}\text{U}$ normalised to reference material GJ-1
Common-Pb correction, composition and uncertainty	Analyses with high common-Pb rejected during data reduction
Uncertainty level & propagation	Ages are quoted at 2 sigma internal errors
Quality control / Validation	GJ-1 (Jackson et al. 2004); 91500 (Weidenbeck et al. 1995)

Appendix III - LA-ICP-MS Methodology II

LA-ICP-MS U-Th-Pb dating methodology, Department of Geology, Lund University

Laboratory & Sample Preparation	
Laboratory name	LA-ICP-MS Lund University
Sample type / mineral	Monazite
Sample preparation	Conventional mineral separation, 1 inch resin mount, 1 μm polish to finish.
Imaging	BSE-imaging, Hitachi S-4300N, 10 mm working distance.
Laser ablation system	
Make, Model & type	Photon Machines, Analyte G2, excimer laser
Sample holder	HelEx II Active 2-volume
Laser wavelength	193 nm
Pulse width	<4 ns
Fluence	4.39 J/cm ²
Repetition rate	7 Hz
Spot size	10 and 12 μm
Sampling mode/pattern	25 μm single spot analyses
Carrier gas	He, Ni
Background collection	20 seconds
Ablation duration	20 seconds
Wash-out delay	7 seconds
Cell carrier gas flow	C 1 l/min
ICP-MS Instrument	
Make, Model & type	Bruker, Aurora, quadropole ICP-MS
Sample introduction	Via conventional tubing
RF power	Approx. 1000-1100 W
Sample gas flow	~1.0 l/min Ar
Detection system	Single collector
Masses measured	202, 206, 207, 208, 232, 238
Integration time per peak	10-30 ms
Total integration time per reading	Approx. 0.1 sec
Sensitivity	4000-7000 cps ²⁰⁷ Pb
Data Processing	
Gas blank	20 second on-peak
Calibration strategy	44069 used as a primary reference material in two sequences and in-house standard Bjertnes (506 Ma) as primary reference material in a third

Reference Material info	44069 (Aleinikoff et al. 2006)
Data processing package used	Iolite Software, downhole correction following Paton et al. (2010), DRS: X_U_Pb_Geochron4. Isoplot 4.15 (Ludwig, 2008)
Mass discrimination	Standard-sample bracketing with $^{207}\text{Pb}/^{206}\text{Pb}$ and $^{206}\text{Pb}/^{238}\text{U}$ normalised to reference material 44069
Common-Pb correction, composition and uncertainty	Analyses with high common-Pb rejected during data reduction
Uncertainty level & propagation	Ages are quoted at 2 sigma internal errors
Quality control / Validation	44069: $^{207}\text{Pb}/^{206}\text{Pb}$ Age = 1065 ± 20 Ma Bjertnes: $^{207}\text{Pb}/^{206}\text{Pb}$ Age = 506 ± 2 Ma

Appendix IV Isocon Data

Panel A

In Panel A the average for each component is calculated (KES150004 is considered as least altered/unaltered and thus excluded).

Component	KES150001	KES150002	KES150003	KES150004	KES150005	KES150006	Average (KES150004 excluded)
SiO2	78.43	72.53	77.19	66.98	67.42	84.80	71.34
Al2O3	11.53	13.34	11.29	16.87	11.49	7.39	13.31
Fe2O3	0.86	1.90	3.38	1.52	12.67	1.50	4.24
MgO	4.40	0.71	1.56	2.06	1.13	2.44	2.08
CaO	0.04	0.10	0.04	0.33	0.26	<0.01	0.18
Na2O	0.23	0.32	1.81	5.76	0.93	0.08	1.81
K2O	2.45	9.78	3.16	5.47	4.04	2.08	5.44
TiO2	0.09	0.11	0.08	0.14	0.12	0.05	0.12
P2O5	<0.01	<0.01	<0.01	<0.01	0.01	<0.01	0.01
MnO	<0.01	0.03	<0.01	0.10	0.05	<0.01	0.06
Cr2O3	<0.002	<0.002	<0.002	<0.002	<0.002	<0.002	Not defined
Ni	<20	<20	<20	<20	<20	<20	Not defined
Sc	4	5	3	7	6	3	5.50
LOI	1.7	0.9	1.3	0.6	1.6	1.5	1.20
Sum	99.76	99.76	99.82	99.80	99.70	99.86	99.76
Ba	188	1027	215	674	1190	77	769.75
Be	1	4	5	7	6	2	4.50
Co	86.4	45.0	45.1	22.5	41.2	55.5	48.78
Cs	2.0	0.8	0.5	2.1	1.0	0.9	1.48
Ga	18.8	21.4	18.9	30.4	18.4	23.4	22.25
Hf	6.0	7.3	5.8	9.6	5.5	3.7	7.10
Nb	15.8	21.3	19.2	26.0	15.8	12.5	19.73
Rb	71.0	226.7	65.1	184.7	102.3	62.8	146.18
Sn	3	4	4	8	5	35	5.00

Sr	8.1	10.9	5.3	8.2	6.8	2.3	8.50
Ta	1.2	1.4	1.5	2.3	1.4	0.9	1.58
Th	12.4	15.9	14.3	31.1	17.5	9.5	19.23
U	3.1	3.7	3.7	7.6	4.4	2.5	4.70
V	<8	<8	<8	<8	12	<8	12.00
W	812.3	397.9	401.2	155.3	322.8	521.2	422.08
Zr	189.4	218.5	157.3	262.6	147.1	103.5	204.40
Y	14.7	54.8	42.7	41.6	118.4	20.6	57.38
La	21.2	48.5	99.9	36.7	75.3	21.5	45.43
Ce	50.2	95.2	213.3	73.9	104.7	50.7	81.00
Pr	6.78	11.84	27.27	10.10	18.81	6.97	11.88
Nd	27.4	46.3	97.8	39.3	70.2	27.5	45.80
Sm	4.81	9.14	16.17	7.86	14.03	5.73	8.96
Eu	0.59	1.28	2.09	0.49	1.35	0.68	0.93
Gd	3.45	9.70	12.36	6.85	16.88	4.77	9.22
Tb	0.51	1.59	1.56	1.19	3.13	0.86	1.61
Dy	2.62	9.01	7.72	7.72	19.14	4.92	9.62
Ho	0.60	2.09	1.53	1.77	4.04	0.96	2.13
Er	1.92	6.01	4.27	5.65	10.72	3.23	6.08
Tm	0.32	0.94	0.70	0.95	1.62	0.52	0.96
Yb	2.52	6.30	4.78	6.98	9.81	3.64	6.40
Lu	0.46	0.96	0.75	1.13	1.41	0.52	0.99
TOT/C	<0.02	<0.02	<0.02	<0.02	<0.02	<0.02	Not defined
TOT/S	<0.02	<0.02	<0.02	<0.02	<0.02	<0.02	Not defined
Mo	0.3	<0.1	0.3	0.4	0.9	<0.1	0.53
Cu	1.1	3.3	0.3	0.5	237.6	2.1	60.63
Pb	2.1	1.9	2.4	4.3	2.2	0.9	2.63
Zn	1	8	4	37	9	4	13.75
Ni	0.2	0.3	0.3	1.4	1.3	0.3	0.80
As	<0.5	<0.5	<0.5	10.0	4.8	<0.5	7.40

Cd	<0.1	<0.1	<0.1	<0.1	<0.1	<0.1	Not defined
Sb	<0.1	0.2	<0.1	0.7	2.8	<0.1	1.23
Bi	<0.1	<0.1	<0.1	<0.1	0.9	<0.1	0.90
Ag	<0.1	<0.1	<0.1	<0.1	<0.1	<0.1	Not defined
Au	1.2	<0.5	<0.5	<0.5	<0.5	<0.5	Not defined
Hg	*	*	*	0.02	*	*	Not defined
Tl	<0.1	0.1	<0.1	0.2	<0.1	<0.1	0.15
Se	<0.5	<0.5	<0.5	<0.5	<0.5	<0.5	Not defined

Panel B

In Panel B the least or unaltered composition is divided by the average altered composition.

Component	Least altered composition = UA (Cio)	Average altered composition (Cia)	Slope to data point (Cia/Cio)
SiO2	66.98	76.07	1.14
Al2O3	16.87	11.01	0.65
Fe2O3	1.52	4.06	2.67
MgO	2.06	2.05	0.99
CaO	0.33	0.11	0.33
Na2O	5.76	0.67	0.12
K2O	5.47	4.30	0.79
TiO2	0.14	0.09	0.64
Sc	7	4.2	0.60
Ba	674	539.4	0.80
Be	7	3.6	0.51
Co	22.5	54.64	2.43
Cs	2.1	1.04	0.50
Ga	30.4	20.18	0.66
Hf	9.6	5.66	0.59
Nb	26	16.92	0.65
Rb	184.7	105.58	0.57

Sn	8	10.2	1.28
Sr	8.2	6.68	0.81
Ta	2.3	1.28	0.56
Th	31.1	13.92	0.45
U	7.6	3.48	0.46
W	155.3	491.08	3.16
Zr	262.6	163.16	0.62
Y	41.6	50.24	1.21
La	36.7	53.28	1.45
Ce	73.9	102.82	1.39
Pr	10.1	14.334	1.42
Nd	39.3	53.84	1.37
Sm	7.86	9.976	1.27
Eu	0.49	1.198	2.44
Gd	6.85	9.432	1.38
Tb	1.19	1.53	1.29
Dy	7.72	8.682	1.12
Ho	1.77	1.844	1.04
Er	5.65	5.23	0.93
Tm	0.95	0.82	0.86
Yb	6.98	5.41	0.78
Lu	1.13	0.82	0.73
Mo	0.4	0.5	1.25
Cu	0.5	48.88	97.76
Pb	4.3	1.9	0.44
Zn	37	5.2	0.14
Ni	1.4	0.48	0.34

Panel C

In Panel C . Cia/Cio values are ordered to facilitate identification of immobile elements.

Component	Slope to data point (Cia/Cio)
Cu	97.76
W	3.16
Fe2O3	2.67
Eu	2.44
Co	2.43
La	1.45
Pr	1.42
Ce	1.39
Gd	1.38
Nd	1.37
Tb	1.29
Sn	1.28
Sm	1.27
Mo	1.25
Y	1.21
SiO2	1.14
Dy	1.12
Ho	1.04
MgO	0.99
Er	0.93
Tm	0.86
Sr	0.81
Ba	0.80
K2O	0.79
Yb	0.78
Lu	0.73

Ga	0.66
Al2O3	0.65
Nb	0.65
TiO2	0.64
Zr	0.62
Sc	0.60
Hf	0.59
Rb	0.57
Ta	0.56
Be	0.51
Cs	0.50
U	0.46
Th	0.45
Pb	0.44
Ni	0.34
CaO	0.33
Zn	0.14
Na2O	0.12

Panel D

In Panel D major elements (>0.1%) and trace elements (<0.1%) are scaled.

Component	Least altered composition = UA (Cio)	Average altered composition (Cia)	KES15001 composition	KES150002 composition	KES150003 composition	KES150005 composition	KES150006 composition	Scale
SiO2	66.98	76.074	78.43	72.53	77.19	67.42	84.8	1.16
Al2O3	16.87	11.008	11.53	13.34	11.29	11.49	7.39	4.51
Fe2O3	1.52	4.062	0.86	1.9	3.38	12.67	1.5	48.68
MgO	2.06	2.048	4.4	0.71	1.56	1.13	2.44	34.95
CaO	0.33	0.11	0.04	0.1	0.04	0.26		212.12
Na2O	5.76	0.674	0.23	0.32	1.81	0.93	0.08	11.81

K2O	5.47	4.302	2.45	9.78	3.16	4.04	2.08	12.07
TiO2	0.14	0.09	0.09	0.11	0.08	0.12	0.05	457.14
Sc	7	4.2	4	5	3	6	3	8.86
Ba	674	539.4	188	1027	215	1190	77	0.09
Be	7	3.6	1	4	5	6	2	8.29
Co	22.5	54.64	86.4	45	45.1	41.2	55.5	2.49
Cs	2.1	1.04	2	0.8	0.5	1	0.9	25.71
Ga	30.4	20.18	18.8	21.4	18.9	18.4	23.4	1.71
Hf	9.6	5.66	6	7.3	5.8	5.5	3.7	5.21
Nb	26	16.92	15.8	21.3	19.2	15.8	12.5	1.85
Rb	184.7	105.58	71	226.7	65.1	102.3	62.8	0.25
Sn	8	10.2	3	4	4	5	35	5.50
Sr	8.2	6.68	8.1	10.9	5.3	6.8	2.3	5.12
Ta	2.3	1.28	1.2	1.4	1.5	1.4	0.9	17.39
Th	31.1	13.92	12.4	15.9	14.3	17.5	9.5	1.22
U	7.6	3.48	3.1	3.7	3.7	4.4	2.5	4.74
W	155.3	491.08	812.3	397.9	401.2	322.8	521.2	0.22
Zr	262.6	163.16	189.4	218.5	157.3	147.1	103.5	0.12
Y	41.6	50.24	14.7	54.8	42.7	118.4	20.6	0.72
La	36.7	53.28	21.2	48.5	99.9	75.3	21.5	0.76
Ce	73.9	102.82	50.2	95.2	213.3	104.7	50.7	0.35
Pr	10.1	14.334	6.78	11.84	27.27	18.81	6.97	2.38
Nd	39.3	53.84	27.4	46.3	97.8	70.2	27.5	0.56
Sm	7.86	9.976	4.81	9.14	16.17	14.03	5.73	2.54
Eu	0.49	1.198	0.59	1.28	2.09	1.35	0.68	36.73
Gd	6.85	9.432	3.45	9.7	12.36	16.88	4.77	2.34
Tb	1.19	1.53	0.51	1.59	1.56	3.13	0.86	11.76
Dy	7.72	8.682	2.62	9.01	7.72	19.14	4.92	1.55
Ho	1.77	1.844	0.6	2.09	1.53	4.04	0.96	5.65
Er	5.65	5.23	1.92	6.01	4.27	10.72	3.23	1.42

Tm	0.95	0.82	0.32	0.94	0.7	1.62	0.52	6.32
Yb	6.98	5.41	2.52	6.3	4.78	9.81	3.64	0.57
Lu	1.13	0.82	0.46	0.96	0.75	1.41	0.52	1.77
Mo	0.4	0.5	0.3		0.3	0.9		220.00
Cu	0.5	48.88	1.1	3.3	0.3	237.6	2.1	172.00
Pb	4.3	1.9	2.1	1.9	2.4	2.2	0.9	19.53
Zn	37	5.2	1	8	4	9	4	2.22
Ni	1.4	0.48	0.2	0.3	0.3	1.3	0.3	57.14

Component	Cio after scaling	Cia after scaling	KES150001 after scaling	KES150002 after scaling	KES150003 after scaling	KES150005 after scaling	KES150006 after scaling
SiO2	78	88.59	91.33	84.46	89.89	78.51	98.75
Al2O3	76	49.59	51.94	60.10	50.86	51.76	33.29
Fe2O3	74	197.76	41.87	92.50	164.55	616.83	73.03
MgO	72	71.58	153.79	24.82	54.52	39.50	85.28
CaO	70	23.33	8.48	21.21	8.48	55.15	
Na2O	68	7.96	2.72	3.78	21.37	10.98	0.94
K2O	66	51.91	29.56	118.00	38.13	48.75	25.10
TiO2	64	41.14	41.14	50.29	36.57	54.86	22.86
Sc	62	37.20	35.43	44.29	26.57	53.14	26.57
Ba	60	48.02	16.74	91.42	19.14	105.93	6.85
Be	58	29.83	8.29	33.14	41.43	49.71	16.57
Co	56	135.99	215.04	112.00	112.25	102.54	138.13
Cs	54	26.74	51.43	20.57	12.86	25.71	23.14
Ga	52	34.52	32.16	36.61	32.33	31.47	40.03
Hf	50	29.48	31.25	38.02	30.21	28.65	19.27
Nb	48	31.24	29.17	39.32	35.45	29.17	23.08
Rb	46	26.29	17.68	56.46	16.21	25.48	15.64
Sn	44	56.10	16.50	22.00	22.00	27.50	192.50
Sr	42	34.21	41.49	55.83	27.15	34.83	11.78

Ta	40	22.26	20.87	24.35	26.09	24.35	15.65
Th	38	17.01	15.15	19.43	17.47	21.38	11.61
U	36	16.48	14.68	17.53	17.53	20.84	11.84
W	34	107.51	177.84	87.11	87.84	70.67	114.11
Zr	32	19.88	23.08	26.63	19.17	17.93	12.61
Y	30	36.23	10.60	39.52	30.79	85.38	14.86
La	28	40.65	16.17	37.00	76.22	57.45	16.40
Ce	26	36.17	17.66	33.49	75.04	36.84	17.84
Pr	24	34.06	16.11	28.13	64.80	44.70	16.56
Nd	22	30.14	15.34	25.92	54.75	39.30	15.39
Sm	20	25.38	12.24	23.26	41.15	35.70	14.58
Eu	18	44.01	21.67	47.02	76.78	49.59	24.98
Gd	16	22.03	8.06	22.66	28.87	39.43	11.14
Tb	14	18.00	6.00	18.71	18.35	36.82	10.12
Dy	12	13.50	4.07	14.01	12.00	29.75	7.65
Ho	10	10.42	3.39	11.81	8.64	22.82	5.42
Er	8	7.41	2.72	8.51	6.05	15.18	4.57
Tm	6	5.18	2.02	5.94	4.42	10.23	3.28
Yb	4	3.10	1.44	3.61	2.74	5.62	2.09
Lu	2	1.45	0.81	1.70	1.33	2.50	0.92
Mo	88	110.00	66.00		66.00	198.00	
Cu	86	8407.36	189.20	567.60	51.60	40867.20	361.20
Pb	84	37.12	41.02	37.12	46.88	42.98	17.58
Zn	82	11.52	2.22	17.73	8.86	19.95	8.86
Ni	80	27.43	11.43	17.14	17.14	74.29	17.14

Components in bold are components from Panel C that were considered to be most immobile. Cu is not included in the isocon diagram because of the extreme internal variation and the subsequent distorting effects on the actual plot. In order to avoid overloading the plot in a single area, arbitrarily scale values were chosen, compare with Grant (2005). The initial total # of values were 39. Scale values were decreased with 2, starting with $2*39=78$. Some native elements were later added and therefore assigned new scale numbers.

Appendix V Geochronology Data

LA-ICP-MS data for analyzed zircons and monazites.

Spot	U (ppm)	Th (ppm)	Th/U	$^{238}\text{U}/^{206}\text{Pb}$	$\pm\sigma$	$^{207}\text{Pb}/^{206}\text{Pb}$	$\pm\sigma$	Conc. %	$^{207}\text{Pb}/^{206}\text{Pb}$ age (Ma)	$\pm\sigma$
<i>Sample KES150001 - Zircon</i>										
S01_01	914	450.6	0.49	3.182	0.027	0.1152	0.0007	94	1881	11
S01_02	786	337.2	0.43	2.999	0.029	0.1165	0.0010	98	1899	15
S01_03	723	290.9	0.40	2.946	0.022	0.1165	0.0008	99	1902	13
S01_04	745	271.4	0.37	2.848	0.021	0.1156	0.0008	103	1886	13
S01_05	592.1	244.8	0.41	3.022	0.024	0.1167	0.0009	97	1903	14
S01_06	1900	142.6	0.07	3.634	0.049	0.1102	0.0009	87	1800	14
S01_07	315.3	162.8	0.52	2.939	0.037	0.1294	0.0016	90	2086	22
S01_08	1287	714	0.56	3.113	0.030	0.1161	0.0006	95	1895.8	9.9
S01_09	867	390	0.45	2.970	0.021	0.1176	0.0008	98	1918	12
S01_10	257.3	210	0.80	3.390	0.054	0.1127	0.0012	90	1840	19
S01_11	388	157	0.41	2.895	0.030	0.1169	0.0010	100	1906	15
S01_12	762	276.6	0.39	2.986	0.025	0.1170	0.0008	97	1909	12
S01_13	577.2	170.5	0.31	3.146	0.036	0.1202	0.0014	91	1954	20
S01_14	329.5	152.7	0.49	2.951	0.024	0.1165	0.0008	99	1900	13
S01_15	601	320	0.55	3.105	0.035	0.1157	0.0010	95	1888	15
S01_16	647.2	230.9	0.37	2.883	0.032	0.1170	0.0009	101	1908	14
S01_17	179.7	70.7	0.42	3.022	0.030	0.1169	0.0012	97	1904	18
S01_18	985	570	0.64	3.036	0.035	0.1171	0.0009	96	1909	14
S01_19	781	312	0.44	2.745	0.026	0.1175	0.0008	104	1916	12
S01_20	668	247	0.40	2.830	0.024	0.1161	0.0009	103	1894	13
S01_21	194.9	83.5	0.46	2.844	0.064	0.1210	0.0021	99	1966	32
S01_22	481.2	234.6	0.51	2.921	0.032	0.1158	0.0009	100	1888	14
S01_23	629.3	248.5	0.41	3.056	0.036	0.1176	0.0009	95	1918	14
S01_24	353	153.3	0.46	2.913	0.028	0.1184	0.0030	99	1920	28
S01_25	513.7	195.9	0.40	2.923	0.026	0.1169	0.0011	100	1904	17
S01_26	310	130.2	0.44	2.933	0.030	0.1158	0.0011	100	1892	18
S01_27	411	189.7	0.48	2.987	0.029	0.1187	0.0016	96	1930	24
S01_28	577.6	239.5	0.42	2.990	0.028	0.1150	0.0008	99	1877	13
S01_29	589	281	0.46	2.924	0.035	0.1162	0.0010	100	1895	15
S01_30	759	338.2	0.43	2.992	0.024	0.1166	0.0008	98	1902	12
S01_31	689	266.9	0.36	2.933	0.022	0.1178	0.0010	99	1919	14
S01_32	743	1150	1.15	3.033	0.035	0.1189	0.0010	95	1937	15
S01_33	645.8	285.9	0.41	2.982	0.028	0.1198	0.0027	97	1930	21
S01_34	834	392	0.40	2.978	0.028	0.1182	0.0009	97	1927	13
S01_35	726	367	0.47	3.050	0.025	0.1178	0.0011	95	1923	15
S01_36	393	193	0.45	2.990	0.023	0.1171	0.0009	97	1912	13
S01_37	675.6	304	0.39	2.994	0.026	0.1181	0.0009	97	1924	14
S01_38	1176	714.3	0.53	2.955	0.024	0.1178	0.0008	98	1920	13
S01_39	418	261.5	0.56	3.023	0.026	0.1179	0.0009	96	1922	14
S01_40	385	221.7	0.52	2.931	0.027	0.1172	0.0009	99	1910	14

S01_41	1423	929	0.59	2.945	0.035	0.1185	0.0010	98	1931	15
S01_42	912	429	0.47	2.892	0.031	0.1178	0.0009	100	1922	13
S01_43	558.1	227.7	0.40	2.940	0.035	0.1185	0.0013	98	1930	20
S01_44	939	273.3	0.29	4.350	0.051	0.1113	0.0009	73	1817	15
S01_45	405	195.7	0.46	3.086	0.031	0.1167	0.0011	95	1906	16
S01_46	2308	1573	0.62	3.117	0.032	0.1167	0.0008	94	1904	13
S01_47	936	520	0.47	3.033	0.031	0.1183	0.0008	95	1929	13
S01_48	377	220.7	0.54	3.019	0.044	0.1181	0.0016	96	1920	25

Sample KES150002 - Zircon

S02_01	429	191	0.43	2.927	0.028	0.1162	0.0010	100	1896	15
S02_02	768.4	344.9	0.45	2.874	0.026	0.1160	0.0010	102	1893	15
S02_03	1143	582	0.50	3.319	0.041	0.1228	0.0014	85	2000	22
S02_04	901	437	0.48	2.998	0.025	0.1163	0.0007	98	1897	11
S02_05	938	435.9	0.46	2.862	0.034	0.1168	0.0010	101	1904	16
S02_06	443	270.7	0.60	2.858	0.033	0.1175	0.0011	101	1914	17
S02_07	912.3	435.7	0.47	3.041	0.025	0.1161	0.0008	97	1897	12
S02_08	825.1	408.5	0.49	2.966	0.029	0.1185	0.0009	97	1931	14
S02_09	647.7	298.6	0.45	3.007	0.024	0.1170	0.0009	97	1908	13
S02_10	1001	554.4	0.53	3.187	0.036	0.1162	0.0010	93	1895	16
S02_11	1013	569	0.54	2.930	0.039	0.1180	0.0014	98	1922	20
S02_12	1223	697	0.53	2.944	0.031	0.1167	0.0009	99	1905	14
S02_13	1709	1330	0.69	3.390	0.070	0.1170	0.0012	87	1907	19
S02_14	413.1	216.7	0.49	2.950	0.028	0.1174	0.0012	98	1913	17
S02_15	670	278.2	0.41	2.940	0.027	0.1165	0.0010	99	1900	15
S02_16	655	266.3	0.40	3.044	0.036	0.1163	0.0009	96	1898	13
S02_17	676.5	301.1	0.44	2.823	0.026	0.1159	0.0010	103	1890	16
S02_18	681.1	308.4	0.45	2.899	0.025	0.1165	0.0008	101	1900	13
S02_19	898	395	0.43	3.118	0.037	0.1166	0.0011	94	1902	16
S02_20	608	274	0.45	3.024	0.029	0.1166	0.0013	97	1901	19
S02_21	732	322	0.45	2.927	0.027	0.1171	0.0009	99	1913	14
S02_22	582.2	277.6	0.48	3.060	0.030	0.1167	0.0009	96	1904	14
S02_23	564.3	223.9	0.40	2.936	0.029	0.1156	0.0008	100	1888	12
S02_24	589.8	230.6	0.40	3.248	0.028	0.1204	0.0010	88	1960	15
S02_25	611	196	0.33	2.872	0.042	0.1172	0.0013	101	1910	20
S02_26	514	185.2	0.37	2.889	0.034	0.1156	0.0011	102	1885	17
S02_27	631	422.1	0.69	2.996	0.027	0.1157	0.0008	98	1888	12
S02_28	462.7	170.2	0.38	3.052	0.056	0.1183	0.0020	95	1924	31
S02_29	1187	819	0.69	3.007	0.039	0.1158	0.0010	98	1891	16
S02_30	798	372.1	0.47	3.034	0.080	0.1199	0.0028	94	1948	42
S02_32	596	220	0.38	2.840	0.029	0.1176	0.0010	101	1917	15
S02_33	613.4	257.7	0.43	2.880	0.027	0.1162	0.0008	101	1896	12
S02_34	682	317	0.48	2.848	0.028	0.1176	0.0014	101	1917	20
S02_35	459.7	220.4	0.49	2.945	0.024	0.1150	0.0009	100	1879	13
S02_36	274.4	116.5	0.44	2.849	0.038	0.1166	0.0011	102	1900	16
S02_37	411.2	216.1	0.52	2.934	0.026	0.1159	0.0009	100	1893	14
S02_38	466	173.5	0.37	2.862	0.028	0.1162	0.0010	102	1895	16

S02_39	454	344	0.75	3.367	0.048	0.1147	0.0011	90	1871	18
S02_40	362.6	129.2	0.37	2.825	0.030	0.1152	0.0011	104	1881	17
S02_41	546	203.1	0.38	2.901	0.029	0.1151	0.0009	102	1879	15
S02_42	479.8	172.4	0.38	2.828	0.026	0.1174	0.0009	102	1914	14
S02_44	503	205.9	0.43	2.798	0.031	0.1167	0.0010	103	1903	15
<i>Sample KES150003 - Zircon</i>										
S03_01	504	209.8	0.42	2.885	0.033	0.1175	0.0016	100	1920	20
S03_03	792.8	372.7	0.47	2.829	0.029	0.1172	0.0010	102	1910	15
S03_04	551	295	0.54	3.111	0.027	0.1190	0.0012	93	1938	18
S03_05	525	294.9	0.56	2.908	0.023	0.1174	0.0009	99	1915	14
S03_07	739	724	0.99	3.650	0.041	0.1210	0.0011	79	1971	16
S03_08	1301	289	0.22	7.675	0.141	0.0985	0.0010	50	1592	19
S03_09	575.4	242.1	0.43	2.806	0.028	0.1190	0.0010	101	1941	15
S03_10	260.8	164.4	0.64	3.070	0.032	0.1183	0.0011	94	1927	16
S03_11	784	349	0.45	3.080	0.051	0.1200	0.0010	93	1952	14
S03_12	558.8	189.2	0.34	2.781	0.029	0.1171	0.0009	104	1910	13
S03_13	617	274.6	0.45	2.763	0.037	0.1176	0.0010	104	1917	16
S03_14	597	253.8	0.43	2.884	0.033	0.1195	0.0013	99	1944	19
S03_15	409.1	397.7	0.98	3.758	0.054	0.1209	0.0014	77	1966	20
S03_16	627	269.1	0.44	2.853	0.047	0.1175	0.0017	101	1910	26
S03_17	744.9	439.1	0.59	2.969	0.038	0.1168	0.0009	98	1905	13
S03_18	739.3	372.1	0.49	3.012	0.038	0.1170	0.0011	97	1906	18
S03_19	700.1	317.2	0.46	2.835	0.036	0.1183	0.0013	101	1925	20
S03_20	688.5	350.6	0.51	3.028	0.030	0.1210	0.0010	93	1969	15
S03_21	990	643	0.57	2.884	0.050	0.1179	0.0011	100	1922	17
S03_22	378.1	184.7	0.48	2.887	0.032	0.1175	0.0010	100	1914	15
S03_23	505.2	233.8	0.46	2.939	0.030	0.1179	0.0009	98	1922	14
S03_24	1003	470	0.46	3.413	0.080	0.1175	0.0018	87	1917	25
S03_25	191.5	61.1	0.30	2.902	0.036	0.1173	0.0013	100	1909	20
S03_26	136.8	52.3	0.38	2.817	0.037	0.1170	0.0015	103	1903	22
S03_27	769	364	0.47	2.809	0.028	0.1175	0.0011	102	1920	14
S03_28	501.2	430.9	0.84	3.097	0.035	0.1209	0.0011	92	1967	16
S03_29	313.6	222.6	0.69	3.890	0.070	0.1189	0.0024	76	1929	29
S03_30	693	369.5	0.53	2.843	0.032	0.1160	0.0008	103	1892	13
S03_31	825	411.9	0.50	2.910	0.039	0.1196	0.0010	98	1946	15
S03_32	1210	853	0.71	3.105	0.036	0.1199	0.0008	92	1952	12
S03_33	174.3	125	0.72	3.007	0.041	0.1186	0.0014	96	1929	21
S03_34	200	78.7	0.39	3.552	0.082	0.1213	0.0026	81	1968	38
S03_35	405	120.5	0.30	5.596	0.110	0.1254	0.0018	52	2032	25
S03_36	733	335	0.46	2.925	0.040	0.1162	0.0009	100	1895	14
S03_37	1417	863	0.61	2.955	0.031	0.1154	0.0009	100	1886	14
S03_38	772.5	402.1	0.52	2.948	0.049	0.1174	0.0011	98	1913	17
S03_39	912	489.8	0.54	2.838	0.034	0.1160	0.0010	103	1893	15
S03_40	811	412.3	0.51	2.964	0.025	0.1172	0.0010	98	1910	14
<i>Sample KES150004 - Zircon</i>										
S04_01	869.3	702.8	0.81	3.123	0.040	0.1198	0.0010	92	1952	15

S04_02	553.1	303.8	0.55	2.931	0.028	0.1173	0.0009	99	1914	13
S04_03	1069.3	1032.8	0.97	2.993	0.026	0.1172	0.0007	97	1912	11
S04_04	1993	1480	0.74	4.367	0.042	0.1166	0.0006	70	1904.1	9.5
S04_05	1275	1091	0.86	2.923	0.023	0.1178	0.0007	99	1921	11
S04_06	774.7	456.4	0.59	2.958	0.034	0.1189	0.0012	97	1937	18
S04_07	859.8	660.7	0.77	3.090	0.027	0.1178	0.0007	94	1921	10
S04_08	965	710	0.74	3.012	0.032	0.1181	0.0009	96	1926	13
S04_09	2214	2536	1.15	5.464	0.116	0.1127	0.0009	59	1842	14
S04_10	709.5	584	0.82	2.938	0.028	0.1182	0.0010	98	1927	14
S04_11	521	298	0.55	2.894	0.038	0.1171	0.0009	100	1910	14
S04_12	795	613.6	0.77	3.608	0.044	0.1221	0.0008	79	1986	12
S04_13	586	326.3	0.56	2.930	0.021	0.1173	0.0007	99	1914	11
S04_14	1720	1729	0.99	5.311	0.054	0.1117	0.0006	61	1825	10
S04_15	467	398	0.83	3.332	0.023	0.1195	0.0006	87	1946.8	9.2
S04_16	1411	1430	1.01	2.892	0.026	0.1173	0.0005	100	1913.3	8.3
S04_18	313.6	138	0.44	2.889	0.024	0.1164	0.0010	101	1898	16
S04_20	848	572	0.67	2.925	0.018	0.1173	0.0005	99	1913.7	8.2
S04_21	697.8	457.8	0.66	2.995	0.027	0.1171	0.0007	97	1910	11
S04_22	601	289.6	0.48	2.923	0.037	0.1181	0.0015	99	1924	22
S04_23	1395	1081	0.75	2.979	0.025	0.1188	0.0006	96	1936.2	9.4
S04_24	690.3	435	0.63	3.206	0.038	0.1203	0.0008	89	1958	12
S04_25	1845	2135	1.16	4.270	0.078	0.1175	0.0010	71	1916	16

Sample KES150005 - Monazite

S05_01	313	5.96E+04	187.62	3.085	0.052	0.1104	0.0024	101	1806	40
S05_02	272.6	2.03E+04	70.87	3.093	0.056	0.1117	0.0025	100	1827	41
S05_03	279.4	41720	148.81	3.089	0.052	0.111	0.0024	100	1816	39
S05_04	241.2	2.91E+04	111.11	3.018	0.057	0.1098	0.0027	104	1796	45
S05_05	339	3.56E+04	102.99	3.151	0.048	0.1138	0.0027	97	1861	43
S05_06	365	53270	143.68	3.081	0.051	0.1108	0.0023	101	1813	38
S05_07	332	5.19E+04	150.38	3.026	0.049	0.1095	0.0023	103	1791	38
S05_08	363	8.72E+04	242.07	3.052	0.041	0.1103	0.0022	102	1804	36
S05_09	401	5.06E+04	124.69	3.040	0.065	0.1085	0.0031	103	1774	52
S05_10	328	6.14E+04	180.18	3.131	0.058	0.1131	0.0027	97	1850	43
S05_11	348	4.25E+04	120.63	3.042	0.050	0.1097	0.0023	103	1794	38
S05_12	230	36230	156.99	3.048	0.051	0.1113	0.0021	101	1821	34
S05_13	368	3.15E+04	84.46	3.106	0.050	0.1124	0.0022	98	1839	35
S05_14	409	25150	61.09	3.126	0.051	0.1139	0.0026	97	1863	41
S05_15	290	4.81E+04	164.42	3.067	0.049	0.1111	0.0025	100	1817	41
S05_16	315	3.67E+04	113.90	3.113	0.044	0.1128	0.0023	98	1845	37
S05_17	317.7	4.05E+04	126.10	3.093	0.054	0.1121	0.0025	99	1834	40
S05_18	338	3.09E+04	89.29	3.042	0.046	0.1099	0.0026	103	1798	43
S05_19	346	42010	120.63	3.055	0.051	0.1122	0.0024	100	1835	39
S05_20	257	5.27E+04	195.31	3.099	0.069	0.1135	0.0037	99	1856	59
S05_21	337	42020	122.85	3.060	0.058	0.1122	0.0026	100	1835	42
S05_22	361	7.83E+04	212.22	3.034	0.043	0.1108	0.0024	102	1813	39
S05_23	306.4	21430	69.83	3.086	0.054	0.1135	0.003	98	1856	48

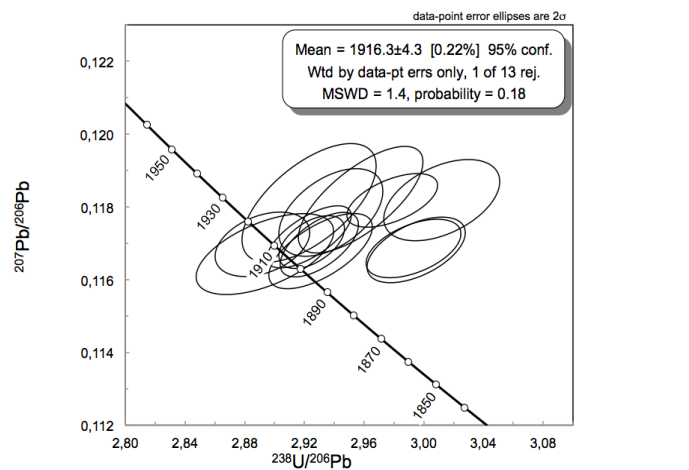
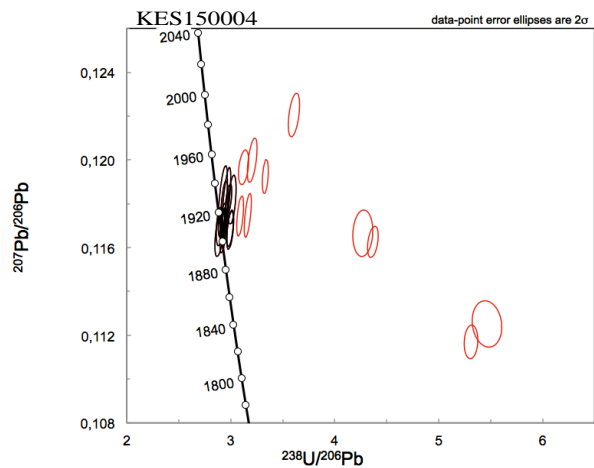
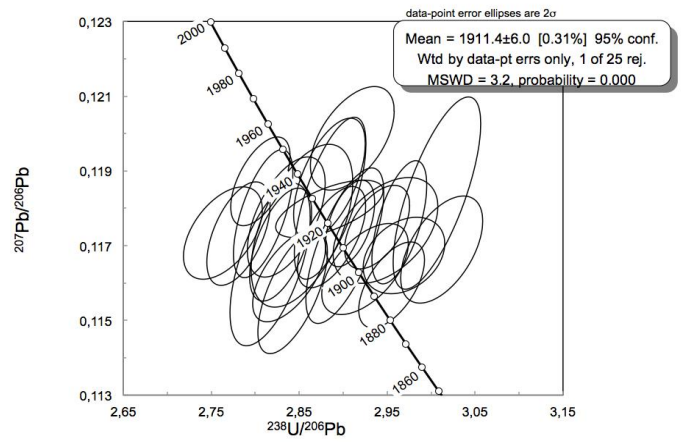
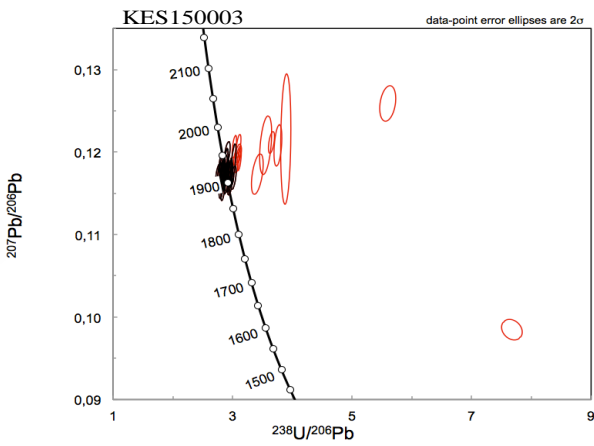
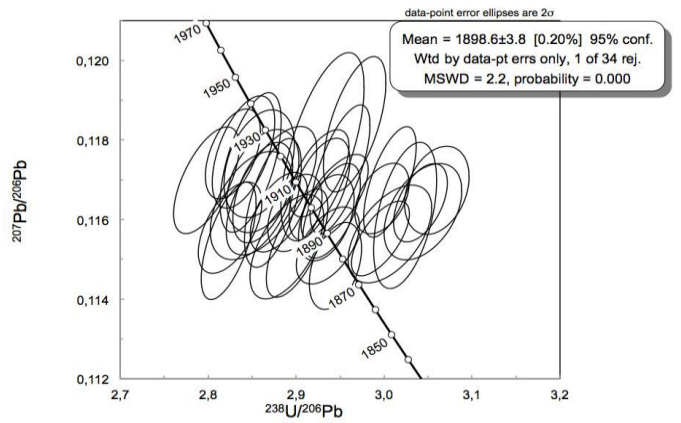
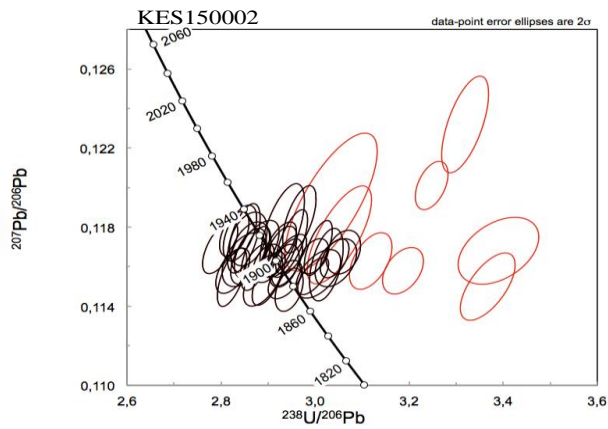
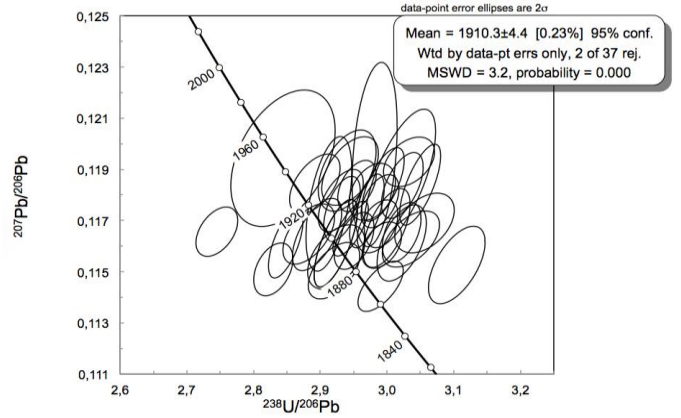
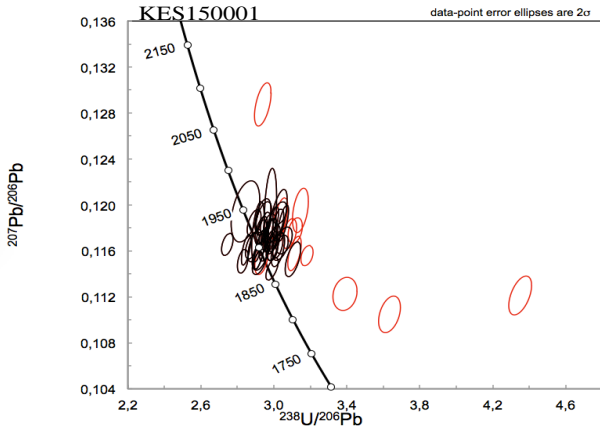
S05_24	289	9.01E+04	309.31	3.086	0.054	0.1132	0.003	99	1851	48
S05_25	297	24680	82.44	3.022	0.050	0.1112	0.0024	102	1819	39
S05_26	337.5	28030	81.10	2.978	0.053	0.1094	0.0024	105	1789	40
S05_27	411	5.25E+04	126.74	3.081	0.064	0.1127	0.0027	99	1843	43
S05_28	300	3.29E+04	108.11	2.947	0.052	0.1095	0.0024	106	1791	40
S05_29	304	5.59E+04	180.51	3.051	0.048	0.1126	0.0023	100	1842	37
S05_30	295	3.05E+04	99.70	2.971	0.052	0.1096	0.0021	105	1793	35
S05_31	323	3.40E+04	103.20	2.945	0.048	0.1096	0.0021	106	1793	35
S05_32	320	4.85E+04	156.25	3.040	0.061	0.1127	0.0034	100	1843	55
S05_33	317.4	22940	72.52	2.997	0.044	0.1099	0.0026	104	1798	43
S05_34	257.9	4.57E+04	174.52	2.997	0.076	0.1113	0.0038	103	1821	62
S05_35	419	6.93E+04	157.98	3.056	0.072	0.1119	0.0032	100	1831	52
S05_36	362	8.02E+04	225.23	2.992	0.047	0.1105	0.0021	104	1808	35
S05_37	276	3.39E+04	119.90	2.957	0.052	0.1105	0.0026	105	1808	43
S05_38	304	25190	82.58	3.013	0.054	0.1123	0.0026	102	1837	42
S05_39	347	8.08E+04	235.24	3.045	0.061	0.1125	0.0027	100	1840	43
S05_40	279.8	28610	102.56	3.044	0.054	0.1135	0.0026	100	1856	41
S05_41	193.8	17250	87.95	2.973	0.056	0.1121	0.0024	103	1834	39
S05_42	340	49710	146.63	2.978	0.051	0.1118	0.002	103	1829	32
S05_43	284.3	5.48E+04	189.04	2.927	0.069	0.1103	0.0035	107	1804	58
S05_44	253	9.58E+04	377.36	2.983	0.067	0.1111	0.0032	103	1817	52
S05_45	352	8.20E+04	232.07	2.998	0.049	0.1115	0.0024	103	1824	39
S05_46	329	50610	153.61	2.952	0.047	0.1103	0.002	104	1804	33
S05_47	358	3.97E+04	108.46	2.933	0.051	0.1105	0.0021	105	1808	35
S05_48	294	23920	82.10	2.915	0.051	0.1104	0.0024	106	1806	40
S05_49	255	71960	280.90	3.003	0.063	0.1137	0.0032	101	1859	51
S05_50	334	49210	145.56	3.048	0.074	0.1148	0.0039	98	1877	61
S05_51	280	8.49E+04	298.51	2.919	0.071	0.11	0.0036	107	1799	60
S05_52	318	22620	69.64	2.930	0.045	0.1119	0.0022	104	1831	36
S05_53	280	17860	61.27	2.883	0.048	0.11	0.0023	107	1799	38
S05_54	367	8.38E+04	228.00	2.970	0.047	0.1142	0.0026	101	1867	41
S05_55	239.3	8.03E+04	332.01	2.843	0.050	0.1128	0.003	107	1845	48
S05_56	298	8.86E+04	295.25	2.756	0.054	0.1172	0.0031	105	1914	47
S05_57	358.3	4.44E+04	115.34	2.946	0.049	0.1287	0.003	91	2080	41
S05_58	423	8.20E+04	193.80	2.761	0.051	0.1217	0.0031	101	1981	45
S05_59	375	5.64E+04	149.48	2.677	0.048	0.1282	0.0029	99	2073	40

Sample KES150008 - Zircon

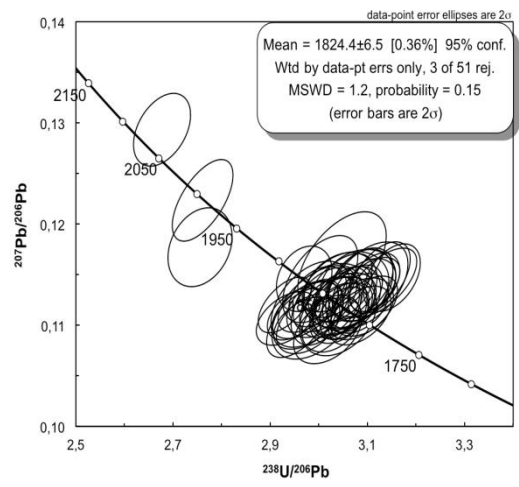
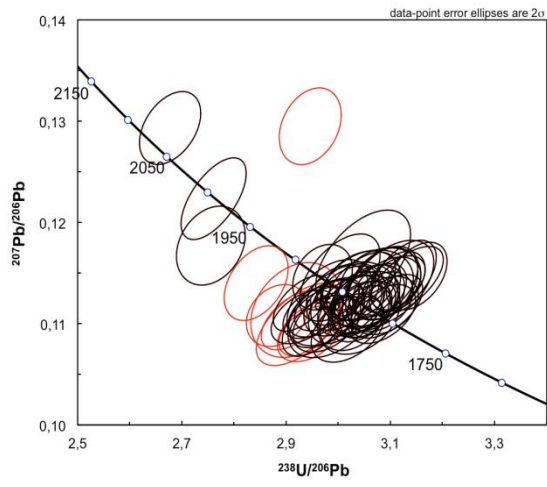
S08_01	1620	1032	0.65	4.075	0.075	0.1088	0.0010	80	1777	17
S08_02	1427	890	0.64	3.554	0.042	0.1106	0.0009	88	1807	15
S08_04	1664	444	0.26	5.708	0.153	0.1081	0.0007	59	1766	12
S08_05	1406	444	0.28	3.810	0.052	0.1091	0.0007	84	1783	12
S08_07	1336	385	0.30	4.174	0.054	0.1088	0.0008	78	1776	13
S08_11	1657	746	0.46	3.404	0.036	0.1107	0.0008	92	1808	13
S08_14	2437	1280	0.54	3.906	0.060	0.1102	0.0006	82	1800.7	9.5
S08_15	2877	1203	0.42	3.762	0.033	0.1129	0.0006	82	1845.6	9.8
S08_16	2937	1414	0.49	3.385	0.030	0.1116	0.0008	91	1823	13

S08_17	2066	1334	0.65	3.626	0.038	0.1104	0.0010	87	1805	16
S08_18	1996	987	0.50	3.171	0.036	0.1121	0.0009	97	1831	14
S08_23	4283	2528	0.55	7.564	0.074	0.0979	0.0007	51	1583	12
S08_24	2515	1892	0.69	4.415	0.070	0.1066	0.0008	76	1740	13
S08_25	2539	2230	0.79	5.549	0.089	0.1034	0.0007	63	1683	12
S08_26	1935	1282	0.62	4.246	0.087	0.1088	0.0006	77	1777	10
S08_29	3225	1833	0.56	3.997	0.048	0.1088	0.0006	81	1777.5	9.3
S08_30	1925	1016	0.52	3.282	0.030	0.1107	0.0008	95	1809	13
S08_31	2002	1222	0.63	3.893	0.052	0.1092	0.0011	83	1782	18
S08_35	1363	609	0.46	4.148	0.052	0.1071	0.0009	80	1748	15
S08_36	1458	388.5	0.27	3.754	0.037	0.1106	0.0008	84	1807	14
S08_38	2129	1637	0.72	7.610	0.064	0.0988	0.0006	50	1600	10
S08_40	1429	139	0.08	3.422	0.033	0.1132	0.0006	89	1849.5	9.1
S08_41	811	636.4	0.77	3.461	0.064	0.1109	0.0008	90	1811	12
S08_42	1321	567	0.42	4.083	0.085	0.1096	0.0005	79	1791.6	8.9
S08_43	2087	69375	33.10	3.416	0.028	0.1111	0.0006	91	1817.6	9.7
S08_44	1304	487	0.38	3.818	0.044	0.1094	0.0007	84	1788	12
S08_45	3902	3797	0.98	6.227	0.081	0.1002	0.0005	59	1625.7	9.3
S08_47	1529	866	0.58	3.164	0.039	0.1106	0.0007	98	1808	11
S08_48	1644	791	0.49	3.837	0.069	0.1089	0.0006	84	1780.4	9.6
S08_49	1886	1292	0.69	4.502	0.067	0.1060	0.0006	75	1730	11
S08_50	2310	798	0.34	4.575	0.092	0.1059	0.0007	74	1728	13
S08_51	2859	1744	0.60	3.965	0.030	0.1094	0.0006	81	1787.5	9.1

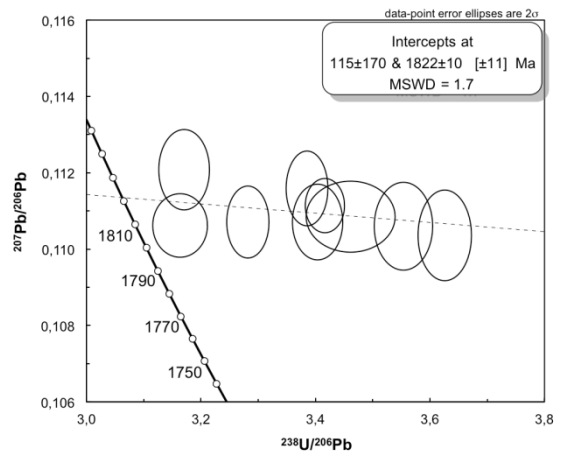
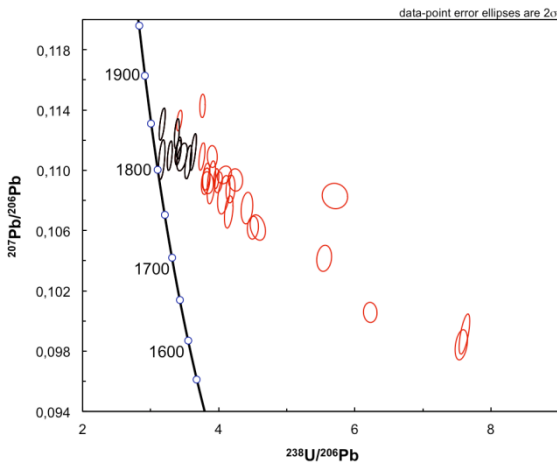
Appendix VI Geochronology Plots



KES150005



KES150008



Tidigare skrifter i serien

”Examensarbeten i Geologi vid Lunds universitet”:

417. Reiche, Sophie, 2014: Ascertaining the lithological boundaries of the Yoldia Sea of the Baltic Sea – a geochemical approach. (45 hp)
418. Mroczek, Robert, 2014: Microscopic shock-metamorphic features in crystalline bedrock: A comparison between shocked and unshocked granite from the Siljan impact structure. (15 hp)
419. Baliya, Fisnik, 2014: Radon ett samhällsproblem - En litteraturstudie om geologiskt sammanhang, hälsoeffekter och möjliga lösningar. (15 hp)
420. Andersson, Sandra, 2014: Undersökning av kalciumkarbonatförekomsten i infiltrationsområdet i Sydsvensk vattenverk, Vombverket. (15 hp)
421. Martin, Ellinor, 2014: Chrome spinel grains from the Komstad Limestone Formation, Killeröd, southern Sweden: A high-resolution study of an increased meteorite flux in the Middle Ordovician. (45 hp)
422. Gabrielsson, Johan, 2014: A study over Mg/Ca in benthic foraminifera sampled across a large salinity gradient. (45 hp)
423. Ingvaldson, Ola, 2015: Ansvarsutredningar av tre potentiellt förorenade fastigheter i Helsingborgs stad. (15 hp)
424. Robygd, Joakim, 2015: Geochemical and palaeomagnetic characteristics of a Swedish Holocene sediment sequence from Lake Storsjön, Jämtland. (45 hp)
425. Larsson, Måns, 2015: Geofysiska undersökningsmetoder för geoenergisystem. (15 hp)
426. Hertzman, Hanna, 2015: Pharmaceuticals in groundwater - a literature review. (15 hp)
427. Thulin Olander, Henric, 2015: A contribution to the knowledge of Fårö's hydrogeology. (45 hp)
428. Peterffy, Olof, 2015: Sedimentology and carbon isotope stratigraphy of Lower–Middle Ordovician successions of Slemestad (Oslo-Asker, Norway) and Brunflo (Jämtland, Sweden). (45 hp)
429. Sjunnesson, Alexandra, 2015: Spårämnesförsök med nitrat för bedömning av spridning och uppehållstid vid återinfiltration av grundvattnen. (15 hp)
430. Henao, Victor, 2015: A palaeoenvironmental study of a peat sequence from Iles Kerguelen (49° S, Indian Ocean) for the Last Deglaciation based on pollen analysis. (45 hp)
431. Landgren, Susanne, 2015: Using calcein-filled osmotic pumps to study the calcification response of benthic foraminifera to induced hypoxia under *in situ* conditions: An experimental approach. (45 hp)
432. von Knorring, Robert, 2015: Undersökning av karstvittring inom Kristianstadsslättens NV randområde och bedömning av dess betydelse för grundvattnets sårbarhet. (30 hp)
433. Rezvani, Azadeh, 2015: Spectral Time Domain Induced Polarization - Factors Affecting Spectral Data Information Content and Applicability to Geological Characterization. (45 hp)
434. Vasilica, Alexander, 2015: Geofysisk karaktärisering av de ordoviciska kalkstensenheter på södra Gotland. (15 hp)
435. Olsson, Sofia, 2015: Naturlig nedbrytning av klorerade lösningsmedel: en modellering i Biochlor baserat på en fallstudie. (15 hp)
436. Huitema, Moa, 2015: Inventering av föroreningar vid en brandövningsplats i Linköpings kommun. (15 hp)
437. Nordlander, Lina, 2015: Borrningsteknikens påverkan vid provtagning inför dimensionering av formationsfilter. (15 hp)
438. Fennvik, Erik, 2015: Resistivitet och IP-mätningar vid Äspö Hard Rock Laboratory. (15 hp)
439. Pettersson, Johan, 2015: Paleoeologisk undersökning av Triberga mosse, sydöstra Öland. (15 hp)
440. Larsson, Alfred, 2015: Mantelpolymer - realitet eller *ad hoc*? (15 hp)
441. Holm, Julia, 2015: Markskador inom skogsbruket - jordartens betydelse (15 hp)
442. Åkesson, Sofia, 2015: The application of resistivity and IP-measurements as investigation tools at contaminated sites - A case study from Kv Renen 13, Varberg, SW Sweden. (45 hp)
443. Lönsjö, Emma, 2015: Utbredningen av PFOS i Sverige och världen med fokus på grundvattnet – en litteraturstudie. (15 hp)
444. Asani, Besnik, 2015: A geophysical study of a drumlin in the Åsnen area, Småland, south Sweden. (15 hp)
445. Ohlin, Jeanette, 2015: Riskanalys över pesticidförekomst i enskilda brunnar i

- Sjöbo kommun. (15 hp)
446. Stevic, Marijana, 2015: Identification and environmental interpretation of microtextures on quartz grains from aeolian sediments - Brattförsheden and Vittskövle, Sweden. (15 hp)
447. Johansson, Ida, 2015: Is there an influence of solar activity on the North Atlantic Oscillation? A literature study of the forcing factors behind the North Atlantic Oscillation. (15 hp)
448. Halling, Jenny, 2015: Inventering av sprickmineraliseringar i en del av Sorgenfrei-Tornquistzonen, Dalby stenbrott, Skåne. (15 hp)
449. Nordas, Johan, 2015: A palynological study across the Ordovician Kinnekulle. (15 hp)
450. Åhlén, Alexandra, 2015: Carbonatites at the Alnö complex, Sweden and along the East African Rift: a literature review. (15 hp)
451. Andersson, Klara, 2015: Undersökning av slugtestsmetodik. (15 hp)
452. Ivarsson, Filip, 2015: Hur bildades Bushveldkomplexet? (15 hp)
453. Glommé, Alexandra, 2015: $^{87}\text{Sr}/^{86}\text{Sr}$ in plagioclase, evidence for a crustal origin of the Hakefjorden Complex, SW Sweden. (45 hp)
454. Kullberg, Sara, 2015: Using Fe-Ti oxides and trace element analysis to determine crystallization sequence of an anorthositenorite intrusion, Älgön SW Sweden. (45 hp)
455. Gustafsson, Jon, 2015: När började platttektoniken? Bevis för platttektoniska processer i geologisk tid. (15 hp)
456. Bergqvist, Martina, 2015: Kan Ölands grundvatten öka vid en uppdämning av de utgrävda dikena genom strandvallarna på Ölands östkust? (15 hp)
457. Larsson, Emilie, 2015: U-Pb baddeleyite dating of intrusions in the south-easternmost Kaapvaal Craton (South Africa): revealing multiple events of dyke emplacement. (45 hp)
458. Zaman, Patrik, 2015: LiDAR mapping of presumed rock-cored drumlins in the Lake Åsnen area, Småland, South Sweden. (15 hp)
459. Aguilera Pradenas, Ariam, 2015: The formation mechanisms of Polycrystalline diamonds: diamondites and carbonados. (15 hp)
460. Viehweger, Bernhard, 2015: Sources and effects of short-term environmental changes in Gullmar Fjord, Sweden, inferred from the composition of sedimentary organic matter. (45 hp)
461. Bokhari Friberg, Yasmin, 2015: The paleoceanography of Kattegat during the last deglaciation from benthic foraminiferal stable isotopes. (45 hp)
462. Lundberg, Frans, 2016: Cambrian stratigraphy and depositional dynamics based on the Tomten-1 drill core, Falbygden, Västergötland, Sweden. (45 hp)
463. Flindt, Anne-Cécile, 2016: A pre-LGM sandur deposit at Fiskarheden, NW Dalarna - sedimentology and glaciotectonic deformation. (45 hp)
464. Karlatou-Charalampopoulou, Artemis, 2016: Vegetation responses to Late Glacial climate shifts as reflected in a high resolution pollen record from Blekinge, south-eastern Sweden, compared with responses of other climate proxies. (45 hp)
465. Hajny, Casandra, 2016: Sedimentological study of the Jurassic and Cretaceous sequence in the Revinge-1 core, Scania. (45 hp)
466. Linders, Wictor, 2016: U-Pb geochronology and geochemistry of host rocks to the Bastnäs-type REE mineralization in the Riddarhyttan area, west central Bergslagen, Sweden. (45 hp)



LUNDS UNIVERSITET

Geologiska institutionen
Lunds universitet
Sölvegatan 12, 223 62 Lund